FINITE ELEMENT ANALYSIS OF DEGRADATION, GROWTH FACTOR RELEASE AND SIGNALING PATHWAY INTERACTIONS IN A 3D SCAFFOLD

by
Sezen ÖZTÜRK

Submitted to the Graduate School of Engineering and Natural Sciences
in partial fulfillment of
the requirements for the degree of Master of Science

Sabancı University
August 2024

FINITE ELEMENT ANALYSIS OF DEGRADATION, GROWTH FACTOR RELEASE AND SIGNALING PATHWAY INTERACTIONS IN A 3D SCAFFOLD

APPROVED BY:

Assoc. Prof. Güllü Kızıltaş Şendur ____________________________
(Thesis Supervisor)

Assoc. Prof. Ahmet Fatih Tabak ____________________________

Asst. Prof. Sibel Çetinel ____________________________

DATE OF APPROVAL: 24.07.2024

ABSTRACT

FINITE ELEMENT ANALYSIS OF DEGRADATION, GROWTH FACTOR RELEASE AND SIGNALING PATHWAY INTERACTIONS IN A 3D SCAFFOLD

SEZEN ÖZTÜRK

Materials Science and Nano Engineering MSc. Thesis, August 2024

Thesis Supervisor: Assoc. Prof. Güllü Kızıltaş Şendur

Keywords: Scaffold degradation, signaling pathway, growth factor release, bone healing, FEM, optimization

Bone scaffolds promise a great potential to gain new treatment strategies to control bone healing and regeneration processes due to their tunable nature. Bone tissue engineering (BTE) gains enduring attention of researchers from various disciplines since it is a multidisciplinary field. This thesis provides a comprehensive examination modeling degradation of a 3D porous polymeric bone scaffold aiming to enhance bone healing with growth factor release and the effect of signaling pathway interactions. A set of reaction-diffusion equations were solved using COMSOL Multiphysics software which employs finite element method (FEM). In the first part, we performed a parametric study with the developed FEM model focusing on scaffold degradation, BMP-2 growth factor release and degradation rates. To validate our 3D model, a previous validation case was performed on a simpler geometry. Next, a signaling pathway evolving due to the released BMP-2 was also modeled deriving Ordinary Differential Equations (ODEs) based on mass action law. The ODE system was subject to Michaelis Menten approach, and a detailed mathematical derivation is presented. In the third part, two optimization algorithms were developed to find optimum values for some selected set of the previously examined parameters effecting the scaffold degradation and growth factor release kinetics. This thesis forms the groundwork for an initial FEM model to be used in analyzing 3D bone scaffolds for degradation and release kinetics in association with signaling pathway interactions. This model should be very useful for various bone scaffold design studies with integration of existing key mechanisms such as angiogenesis into the presented model.

ÖZET

3B KEMİK İSKELESİNDE DEGRADASYON, BÜYÜME FAKTÖRÜ SALINIMI VE SİNYAL YOLU ETKİLEŞİMLERİNİN SONLU ELEMANLAR YÖNTEMİ (FEM) İLE MODELLENMESİ

SEZEN ÖZTÜRK

Malzeme Bilimi ve Nano Mühendislik Yüksek Lisans Tezi, Ağustos 2024

Supervisor: Assoc. Prof. Güllü Kiziltas Sendur

Keywords: Kemik iskelesi degradasyonu, sinyal yolu, büyüme faktörü salımı, kemik iyileşmesi, FEM, optimizasyon

Kemik iskeleleri, ayarlanabilir doğası sayesinde kemik iyileşmesi ve rejenerasyonunu kontrol etmek için yeni tedavi stratejileri konusunda büyük potansiyel vaat etmektedir. Kemik doku mühendisliği (BTE) çok disiplinli bir alan olduğundan çeşitli disiplinlerden araştırmacıların dikkatini çekmektedir. Bu tez çalışması, büyüme faktörü salınımı ve sinyal yolu etkileşiminin etkisini artırarak kemik iyileşmesini amaçlayan 3D gözenekli polimerik kemik doku iskeletinin bozulmasını modellemeyi kapsamlı bir şekilde incelemektedir. Bir dizi reaksiyon-difüzyon denklemi, sonlu elemanlar metotu (FEM) kullanan COMSOL Multiphysics yazılımıyla çözülmüştür. Tezin ilk bölümünde, geliştirilen FEM modeli kullanılarak iskele bozulması, BMP-2 büyüme faktörü salımı ve bunun bozulmasının hızlarına odaklanılarak bir parameter çalışması yapılmıştır. Bu modelin doğrulaması için, daha basit bir geometri üzerinde bir doğrulama çalışması gerçekleştirilmiştir. Ardından, salınan BMP-2'nin neden olduğu bir sinyal yolu da kütle korunumu/hareketi yasasına dayalı bir dizi adi diferansiyel denklem (ODE) türetilerek modellenmiştir. ODE sistemi, Michaelis-Menten yaklaşımına tabi tutulmuş ve detaylı matematiksel türetim sunulmuştur. Tezin üçüncü bölümünde, iskelet bozulması ve büyüme faktörü salınım kinetiğini etkileyen daha önce incelenen bazı parametrelerin optimum değerlerini bulmak için iki optimizasyon algoritması geliştirilmiştir. Bu çalışma, sonlu elemenlar yöntemine dayalı 3 boyutlu kemik iskelelerinin degradasyon ve büyüme

faktörü salınımı kinetiklerinin hücre içi sinyal yollarıyla etkileşimini analiz etmek için bir temel oluşturmaktadır. Dolayısıyla, bu tez çeşitli kemik iskelesi tasarım çalışmalarının halihazırda varolan damarlanma ve kemik yenilenmesi çalışmalarına entegrasyonu için oldukça yararlı bir çalışmadır.

ACKNOWLEDGEMENTS

I would like to express my sense of gratitude to my thesis supervisor Assoc. Prof Dr. Güllü Kızıltaş Şendur for her guidance during my M.Sc. thesis. I would also like to thank the members of Kızıltaş Group, especially Mervenaz Şahin, Özlem Araç and Ata Alipour Ghassabi, who always helped and supported me throughout this thesis study.

I am also thankful to my jury members Asst. Prof Dr. Sibel Çetinel and Assoc. Prof. Dr. Ahmet Fatih Tabak for their interest and feedback about my thesis.

I would like to extend my heartfelt thanks to all my friends who have supported me throughout this journey. I am grateful to Yağız Dereboy, who was always there throughout the course of my thesis, especially in moments when I doubted myself. Their encouragement and advice were invaluable.

Lastly, I would also like to thank my parents for their endless love and support. Your constant belief in me has been the foundation of my perseverance. I would like to give special thanks to my brother for always being my closest friend, especially during the hardest times of this study.

This study was funded by the Scientific and Technological Research Council of Turkey (TÜBİTAK) 1001 research project support program (Project #:119M470).

TABLE OF CONTENTS

LIST OF FIGURES

LIST OF TABLES

LIST OF ABBREVIATIONS

ALP	Alkaline Phosphatase
BMP	Bone Morphogenetic Protein
BSP	Bone Sialoprotein
BTE	Bone Tissue Engineering
DDS	Drug Delivery System
ECM	Extracellular Matrix
FEM	Finite Element Method
GF	Growth Factor
MAPK	Mitogen-activated protein kinases
MM	Michaelis Menten
MSC	Mesenchymal Stem Cell
OCN	Osteocalcin
OPN	Osteopontin
Osx	Osterix
PCL	Polycaprolactone
PLA	Polylactic Acid
PLGA	Poly(Lactic-Co-Glycolic) Acid
Runx2	Runt related transcription factor 2
SAPK	Stress-activated protein kinases
TGF-β	Transforming Growth Factor-B
VEGF	Vascular Endothelial Growth Factor

CHAPTER 1

1. INTRODUCTION

1.1.Motivation

Musculoskeletal fractures affect thousands of people permanently, causing tissue loss and anomalies in daily life. Skeletal autografts and allografts remain the gold standard for treating large bone defects, with over 500,000 procedures performed annually in the US, representing nearly 20% of all bone treatments (Hettiaratchi & Coulter, 2016). In the United States and Europe alone, half a million patients require bone substitutes each year, with global bone fracture costs estimated at US$5.5 billion annually and bone repair at US$17 billion (Tajvar et al., 2023). Despite medical advances, bone grafting techniques face limitations such as low tissue availability, host immune rejection, and infections that may require additional surgeries. Bone tissue engineering (BTE) has emerged as a promising alternative, leveraging scaffolds, growth factors, and stem cells to enhance bone healing and regeneration. This thesis focuses on modeling a 3D porous bone scaffold with particular emphasis on specific mechanisms such as degradation, growth factor release and signaling pathway interaction.

Integrating drug delivery systems (DDS) within scaffolds offers significant advantages for BTE, enabling controlled release of growth factors essential for promoting osteogenesis and enhancing bone healing. Bone tissue scaffolds hold great promise due to their customizable nature, allowing fine-tuning of properties to support specific functions. Advances in production techniques and computational modeling in BTE are enabling the design of scaffolds that meet precise biological and mechanical needs, providing a cost-effective alternative to traditional bone transplants. In this thesis we develop a model taking into account the BMP-2 release from degrading polymer scaffold.

The effect of released BMP-2 on transcription factors which are regulated by BMP-2 are numerically investigated. The selected signaling pathway involves Smad1/5, Runx2 and Osx.

Computational modeling utilizes advanced resources to explore the complex mechanisms of physical systems through mathematical models. This method involves adjusting inputs and boundary conditions in simulations to evaluate diverse scenarios and outcomes. The ability to assess scaffold designs before fabrication, ex vivo testing, and in vivo implantation saves time and money while providing critical design insights. By virtually modifying shape and material properties, various scaffold designs can be evaluated without the need for actual manufacturing. Computational outputs are typically validated by comparing them with experimental findings. Especially, computational studies allow researchers to predict cellular responses to different stimuli, identify potential regulatory nodes, and understand the impact of molecular interactions on overall cell behavior which if performed experimentally requires lots of time and is extremely hard to achieve. This capability is particularly important for elucidating the mechanisms underlying diseases, discovering new drug targets, and designing effective therapeutic interventions. Finite Element Method (FEM) is a powerful computational technique frequently employed in BTE to analyze and predict the behavior of biological structures under different conditions. FEM involves discretizing a complex structure into smaller elements and simulating their responses to various forces and conditions. This allows researchers to develop scaffolds with properties that mimic the mechanical behavior of natural bone, improving BTE outcomes. In this thesis we rely on FEM to develop our GF release integrated scaffold degradation model in COMSOL Multiphysics software and carry out an extensive parametric study to investigate the interplay between the degradation and release parameters and the resulting time dependent concentration profiles.

Optimization algorithms are crucial for advancing scaffold design and functionality since they take advantage of mathematical techniques to find the best design that satisfies multiple conflicting criteria such as in the case of bone scaffold design considering biodegradability. Optimization allows systematic exploration of design parameters and configurations, identifying optimal combinations that maximize performance and efficiency. These algorithms can also incorporate multiple objectives, balancing factors such as drug release and degradation behavior to meet the complex requirements of bone tissue regeneration. Optimization algorithms significantly reduce the time and resources needed for scaffold development, accelerating the process and enhancing the effectiveness of BTE solutions. Therefore, in the second part of the thesis we integrate the developed FEM based integrated release-degradation-signaling pathway model in the first part to an optimization framework in MATLAB with a subset of selected design variables.

1.2.Objective of the Study

The main objective of this study is to develop a Finite Element Analysis (FEA) based analysis framework of a 3D scaffold considering different mechanisms known to affect bone regeneration. This study considers scaffold degradation and growth factor release coupled with the activated signaling pathway by the released growth factor. In the first part of the thesis, we evaluate in depth the affecting parameters of this system modeled in the form of a combination of Partial Differential Equations and Algebraic Equations. Also, another aim of the thesis is to form an initial design optimization toolset for the design of affecting parameters utilizing the developed FEA analysis model. A reaction-diffusion system of equations is used to model a 3D porous bone tissue scaffold from which the initially loaded growth factor is released. This equation system is solved using a FEM-based numerical solver software in COMSOL. Tailoring the degradation rate, degradation mode of the scaffold is crucial before performing in vivo assessments. This thesis offers a validated FEM model with a parametric analysis including a vast number of simulations to show the tunability and the effect of the degradation and release parameters on the resulting concentration solutions of the coupled system. To be more specific, we have selected five parameters, hydrolysis reaction rate of the scaffold, diffusivity of water, degradation rate, release constant, degradation constant of growth factor for the release dynamics. Observations were performed in terms of determining the most effective ones on the system, the interplay between these five parameters and their tunable ranges for the designed system. Other than FEM, an ODE based signaling cascade was modeled to analyze down-regulatory events of BMP-2 since its downregulated signaling pathway is crucial for bone regeneration. The temporal changes in Smad1/5, Runx2 and Osx which are the well-known transcription factors were studied by considering the output of the FEM model. Michaelis-Menten based on Hill function was employed for the signaling events, including their detailed derivations for the pathway. Furthermore, two optimization models were simulated to validate the selected parameters of the integrated FEM model and provide an initial design framework to be used in future studies. The objective functions aim to minimize the deviations of concentration changes in scaffold and growth factor obtained from FEM solution incorporating the simulation and the optimization tools. In future, this validated design framework can be used with other design requirements and constraints addressing various scaffold design problems.

1.3.Literature Review

The field of bone tissue engineering (BTE) has become increasingly important in tackling the difficulties associated with the repair of bone defects. It improves bone healing and regeneration by utilizing scaffolds, growth factors (GFs), and stem cells in concert. Tissue scaffolds are highly customizable for a wide range of applications, which makes them highly promising for directing and assisting the regeneration process. To construct optimal scaffolds that match the multi-scale porous structure required for bone tissue scaffolds (BTS), researchers have delved into multiple approaches for scaffold design that emerged in parallel to recent developments in computer modeling and simulation. This part aims to give a brief summary on previous computational studies focusing on drug release, degradation, intracellular signaling pathways, and existing optimization algorithms highlighting the gaps to be filled with respect to these studies in this thesis.

Numerous studies examining constitutive computational models with the intention of capturing as many aspects as possible of engineered bone scaffolds are abundant in the literature. The literature has been carefully examined and outlined by some researchers (Fletcher & Osborne, 2022; Khotib et al., 2021; N. Musthafa et al., 2024). The degradation of polymeric materials has been numerically analyzed more than a decade, for example in the early work of Gopferich et al. followed and extended by other authors in tissue engineering studies (Adachi et al., 2006; Göpferich, 1996; Sanz-Herrera et al., 2009). The study by Adachi and his coworkers provides a framework for the best possible design of the porous scaffold microstructure using a 3D simulation of bone regeneration, which entails the formation of new bone and scaffold degradation but ignoring drug release effect in their overall design. It was simply assumed that the rate at which the hydrolysis of scaffolds causes a decrease in their mechanical properties was related to the amount of water that diffuses from the surface into the bulk material. To account for the formation of new bone on both scaffold and bone surfaces, the rate equation of mechanically stimulated trabecular surface remodeling was utilized. They performed their simulation using a voxel finite element to mesh their lattice-based scaffold (Adachi et al., 2006). Later, a multiscale mathematical model was proposed by Sanz-Herrera et al. that integrates two different scales: the microscopic level, which represents the pore level of the scaffold, and the macroscopic level, which represents the entire bone organ and scaffold region where the new bone formation was assessed (Sanz-Herrera et al., 2009). They employed a homogenization theory to connect the two distinct levels. The microscopic level was focused on the scaffold's pore structure, taking into account cell migration, proliferation, differentiation based on Fickian diffusion for vascularization, and the production of bone matrix, while the macroscopic level took into account factors like mechanical loads and diffusion processes. There was no growth factor release and signaling pathways in cellular activities accounted for, so the only parameters in their cellular analysis were mechanical load and diffusion. They have used ABAQUS software with a voxel mesh based on FEM which they have adapted from Adachi et al. 's work (Sanz-Herrera et al., 2009). Another study was performed by Rothstein et al. presenting a unified mathematical model to predict controlled release from surface and bulk eroding polymer matrices (Rothstein et al., 2009). This model incorporates degradation kinetics and drug diffusion mechanisms, providing a comprehensive understanding of release dynamics. They have assumed uniform drug loading to their non-porous 2D axisymmetric spherical scaffolds since the loading efficiency is a parameter for release dynamics. Moreover, pursuing surface or bulk degradation scaffolds offers different release kinetics. In their study, the effect of scaffold size and diffusivity of water was analyzed on cumulative protein release. They have created their model in MATLAB (MathWorks, r2007a), then solved it in a FEM-based simulation software, COMSOL Multiphysics (v3.1) (Rothstein et al., 2009).

An agent-based model for studying neovascularization in porous scaffolds was created by Artel et al. (Artel et al., 2011). The process of sprouting angiogenesis, in which new blood vessels form from already existing ones, is simulated by the model. They have made use of the Recursive Porous Agent Simulation Toolkit (Repast) in JAVA to involve both event-driven and time-driven behaviors of the capillary segments. Their scaffold was assumed to be non-degradable, and no VEGF load was performed initially. However, they have solved a simple equation for VEGF concentration profile which calculates the concentration profile in only one direction which provides a constant protein profile throughout the simulation and reflects a steady-state diffusion situation (Artel et al., 2011).

Later, Huang et al. developed a model focused on the dual delivery of growth factors to create temporally stable concentration profiles (G. X. Huang et al., 2015). The partial differential equations controlling the diffusion and release kinetics of the growth factors inside the scaffold were solved with FEM using COMSOL Multiphysics. However, their PDEs accounted for only variables such as growth factors, their antibodies, which were also loaded to scaffolds, and GF-antibody complexes. Their focus has been on the biological responses that follow the controlled release of growth factors from non-degrading scaffolds that are designed layer by layer. Although one of main focuses was the biological assessment driven by TGF-β and/or BMP-4, no computational work was performed in that aspect. They manufactured their scaffolds in accordance with the best designs and analyzed mesenchymal stem cells (MSCs) differentiation into chondrogenic and osteogenic lineages by transcription factor expression such as Runx2 and osteopontin (OPN) with Western blotting (G. X. Huang et al., 2015).

Even though the mentioned studies have utilized a great base for the importance of the computational tools in BTE, their aspect on overall bone regeneration process was very limited. A more comprehensive study was performed by Sun et al., designing a 3D multi-scale model to simulate multiple biological processes, including CaP scaffold degradation, exogenous growth factor release, osteogenic differentiation and proliferation, angiogenesis, and nutrient transport with an integrated approach (X. Sun et al., 2013).The mathematical approach involves a system of nonlinear partial differential equations (PDEs) for scaffold scale analysis and nutrient transport, a set of ordinary differential equations to simulate the intracellular signaling pathways, and nonlinear probability functions to represent angiogenesis and cellular dynamics. Moreover, integrating their previous work in Sun et al., they accounted for cellular population dynamics based on stochastic differential equations (SDEs) (X. Sun et al., 2012). The numerical methods employed in their study include the implicit Euler method for solving the nonlinear ODEs and the Euler-Maruyama method for the SDEs. The model simulations were implemented using MATLAB (MathWorks, R2007b). Their model relied on an intracellular signaling pathway driven by three important growth factors, BMP-2, TGF- β and Wnt. In their signaling cascade, BMP-2 and TGF- β activate a Smad-Runx2 pathway while Wnt is the up-regulator of β-Catenin. Their dynamic concentrations were then differentiation and proliferation of mesenchymal stem cells (MSCs) into osteoblasts and osteoclasts. They also performed a pore size analysis for cumulative release of BMP-2, number of endothelial cells and active osteoblasts, and bone mass (X. Sun et al., 2012, 2013). Wang et al. (2020) developed a 3D computational model similar to Sun et al.'s study eliminating multiple growth factor release effects, intracellular pathway dynamics and cellular phenotype switches, but keeping VEGF release, nutrient transport and the angiogenesis mechanism (L. Wang et al., 2020). They integrated their model with mechanical stimulation on both scaffold and interstitial fluid (filling the porous domain of scaffolds) domains by evaluating strain energy density and scaffold degradation based on a mechanically loaded scaffold scenario. Their new approach was to consider change in diffusion coefficients of transportation elements such as VEGF and oxygen, based on porosity creation time due to scaffold degradation. The numerical implementation of the model employed the finite element method (FEM) on ABAQUS software using Euler finite difference approximation (L. Wang et al., 2020). The main differences between our study and Wang et al. 's are the subset of mechanisms such as degradation, GF release. They modeled the degradation of scaffold using an exponential function representing initial porosity effect and resulting time delay starting from zero porosity of bulk scaffold. We did not consider change in porosity; however, we employed a second order reaction rate expression representing the irreversible hydrolysis of polymer. Also, they used a power function to relate initially loaded growth factor amount to released GF amount. Moreover, they did not involve consequent signaling pathway effect on bone regeneration which is crucial. Based on Sun et al. 's work, we implemented the signaling pathway interactions affected by the released GF amount while the time dependent released GF amount modeled with Michaelis Menten approach (X. Sun et al., 2013). The signaling pathway interactions were constructed considering regulatory systems of BMP-2 under quasi static assumptions, and Smad1/5, Runx2 and Osx were the part of this pathway. Furthermore, we conduct a parametric analysis for the parameters which are crucial in this degradation-GF release system performed based on FEM. To the best of our knowledge, an in-depth analysis of a degradation-GF release model in FEM does not exist. It is noted that the 3D model geometry and parametric data is initially based on the paper information and correspondence with authors. Next, we developed an initial optimization framework on the validated integrated FEM model. As a result of a literature review for parameter optimization for 3D scaffold degradation and GF release, there are no previous studies found.

1.4.Contributions

The tuning ability of patient and fracture specific growth factor release have been a well sought topic in bone tissue engineering. The high cost and time-consuming nature of experimental studies slows down and makes it difficult to present through research on BTE applications. Computational methods offer a valuable research area to fasten in vitro, and in vivo analysis required for bone healing strategies. Moreover, they have the ability to generate bone scaffolds with precise qualities, providing a strong support for the implementation of tissue engineering in the future, particularly in clinical applications. Although the literature is rich in modeling different mechanisms related to the mechanical, biological and chemical features of the bone regeneration process, computational studies focusing on the integration of multiple mechanisms for 3D scaffolds is still rare. To the best of our knowledge, an in-depth parametric study of a coupled degradation- GF release model for 3D scaffolds incorporating signaling pathway interaction mechanism does not exist. Similarly, design optimization studies based on the three-way integrated scaffold model are yet to be conducted. Within this thesis we aimed to develop a computational bone scaffold analysis model based on an existing model in literature performed by Sun et al. and used it for conducting an extensive parametric analysis of 3D scaffold behavior, in particular resulting polymer and BMP-2 concentration profiles using FEA in COMSOL Multiphysics (X. Sun et al., 2013). A secondary objective was to present an initial design optimization framework focusing on the developed and validated model. Since coupling intracellular signaling pathway dynamics and its regulatory effect on gene transcription, which is a requirement for cellular activities, is inadequately studied with computer-aided bone scaffolding, this thesis tried to shed light on this missing feature.

In summary, one of the unique focuses of this thesis was to provide an in-depth parametric analysis for a 3D biodegradable scaffold which exogenously releases a growth factor, namely BMP-2 and degrades over time, solved numerically employing FEM. The validation of the developed model was provided by an in-depth parametric analysis to observe degradation modes of the designed bone scaffold and its release dynamics in comparison to the study by Sun et al. (X. Sun et al., 2013). Thereafter, the dynamics of signaling cascade based on phosphorylation and dephosphorylation events of transcription factors activated by the released growth factor was analyzed. Completing the parametric analysis that included vast number of simulations runs, the second contribution was to develop an optimization framework that was used to perform the self-validation of the selected parameters (the parameter selection was made based on both literature and parametric analysis results) used in the integrated FEM model. Two sequential optimization studies using a gradient based optimization algorithm in MATLAB were presented targeting polymer and GF concentrations at certain timeframes based on the degradation-release integrated FEM model developed in the first part of the thesis.

1.5.Organization of the Thesis

Chapter 1 introduces bone regeneration mechanisms considering previous studies in literature. This chapter delves into the motivations and objectives of this study. A comprehensive literature review specifically overviewing similar previous work which primarily aimed to construct multi-level computational simulation models considering different aspects involved in bone regeneration is provided. It introduces the main goals and maps the gaps that are aimed to be filled with this thesis.

Chapter 2 gives the necessary background information to understand the complex nature of the bone organ and related mechanisms. This chapter summarizes the use of biodegradable bone scaffolds and drug delivery strategies adapted to bone tissue engineering for bone healing and regeneration. Additionally, it provides an overview of numerical methods, especially the finite element method, and summarizes the importance of computational tools in this research field.

Chapter 3 introduces the basic requirements of a bone scaffold while focusing on the mathematical approaches for biodegradable scaffold design and drug release kinetics. Also, the biological connection between a biological signaling pathway driven by the growth factors, BMP-2, which are essential for enhanced bone healing strategies is presented. For the modeling part, it summarizes the initial validation study in a 2D geometry and then details the 3D porous scaffold model. After, it unveils the details of mathematical derivations of Michaelis Menten law and Hill function for enzyme-substrate kinetics to be applied on interactions between growth factors and transcription factors based on mass action law. Then, the optimization algorithms targeting to find optimal values of the important parameters decided based on the 3D model and its parametric analysis were provided.

Chapter 4 provides the tabular and graphical results of the FEM model, signaling interactions and optimization algorithms. First, the results of the background validation study are presented. Then, polymer and growth factor concentrations obtained from the 3D model are presented. The analysis of the concentration profiles of degrading polymer, released growth factor is explained based on the parametric study performed using finite element simulations. Afterwards, the signaling pathway components' dynamics are unveiled. Later, the optimization algorithm and its results are explained.

Chapter 5 summarizes the key conclusions and implications of the study. This chapter aims to bring together all the provided information and reveal the contributions of this work while explaining the possibilities of future research studies.

CHAPTER 2

2. BACKGROUND AND LITERATURE REVIEW

2.1.Formation and Regeneration of Bone

The skeletal system is a body system composed of bone and cartilage tissues. Bone is a connective tissue that has multiple functions in the body, including protecting soft inner organs, storing minerals and mesenchymal stem cells inside the bone marrow, functioning as a reservoir of growth factor and cytokines, and giving its shape to the body with its load bearing capacity. There are 213 bones in the body which can be categorized into four groups, namely long bones, short bones, flat bones and irregular bones (B. Clarke, 2008). Bones include two sections inside them, which are called cancellous and cortical bone as shown in Figure 1. The cancellous bone or trabecular bone has a spongy lattice structure. The cortical bone or compact bone is dense and forms the outer shell that surrounds the marrow space (Hettiaratchi & Coulter, 2016). Although cancellous bone has a larger surface area than cortical bone, 80% of total bone mass belongs to cortical bone due to its denser structure. Both sections consist of osteons. Cortical osteons are composed of Haversian canals (Haversian system) which are longitudinal central canals. They are surrounded by equally sized concentric lamellar host osteocytes. Haversian canals vascularize bone through blood vessels that penetrate cortical bone from the periosteum (Kim et al., 2015). The periosteum is a connective tissue that packs enclosed in the cortical bone. Bone is made up of both organic (70-90%) and inorganic (10-30%) elements (Ansari, 2019). Inorganic elements are largely minerals including calcium phosphate and calcium carbonate. These minerals crystallized to form hexagonal hydroxyapatite ($Ca_{10}(PO_4)_6(OH)_2$). The Organic part is formed of almost 90% fibrous proteins and with the remainder being non-collagenous proteins, lipids, and other bone matrix proteins such as osteopontin (OPN) (Ansari, 2019; B. Clarke, 2008; Hettiaratchi & Coulter, 2016). Cartilage is a collagen-based connective tissue that covers movable parts of bone. Articular cartilage is a gel-like tissue that is made up of large protein-polysaccharide molecules providing a smooth and lubricated surface for joints and lowering the friction coefficient at load bearing surfaces (Lanza, 2014).

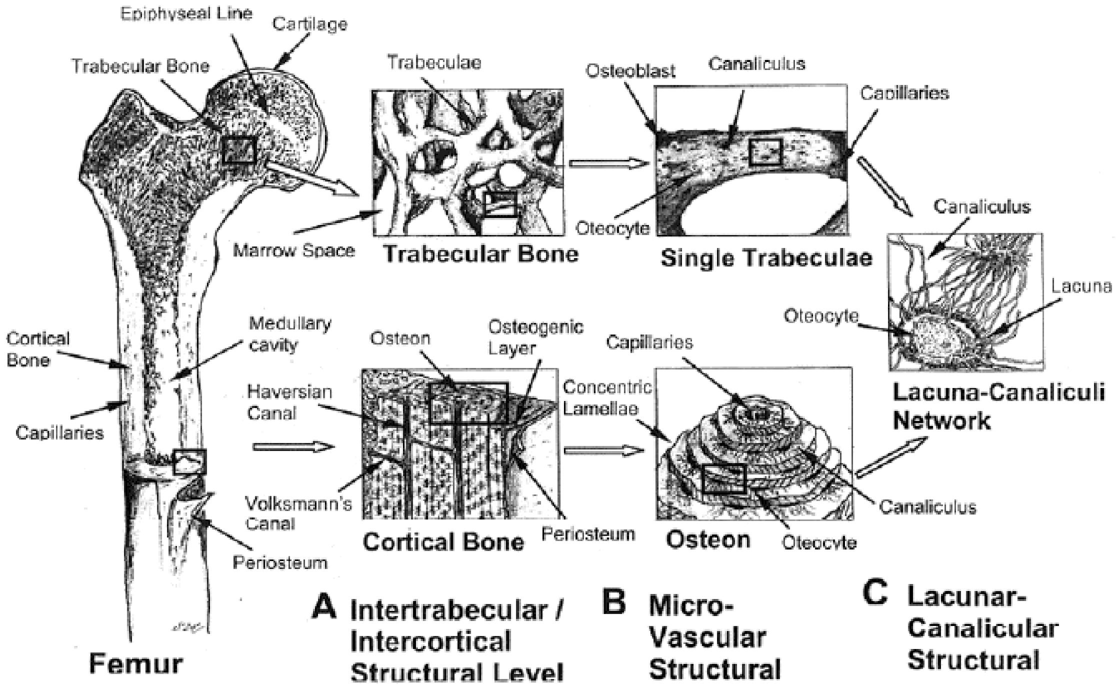

Figure 1: Hierarchical structure of a long bone from osteons through cancellous and cortical bone *(Liebschner & Wettergreen, 2003)*.

Bone cells play essential roles in the maintenance, growth, and repair of bone tissue. They can be categorized into four main types: osteoprogenitor cells, osteoblasts, osteocytes, and osteoclasts. They are very distinct in their duties however their roles are highly interconnected. Osteoprogenitor cells are precursor cells that are derived from stem cells and have the ability to form osteoblasts. They are found in both the periosteum (the outer layer of bone) and the inner part of bone (Caplan, 2001). Osteoblasts are responsible for bone production and are found near the surface of bones. They secrete collagen, alkaline phosphatase and other extracellular matrix (ECM) components. They also create space for calcium and phosphate enabling them to deposit these minerals(Lanza, 2014). In this way, osteoblasts can start bone formation via mineralization. Upon completion of mineralization, they either become surrounded by ECM and differentiate into osteocytes or approximately 50-70% of them undergo apoptosis (B. Clarke, 2008). Osteocytes are found in osteons and are responsible for homeostasis. They regulate oxygen and mineral levels as well as orchestrating bone remodeling via signaling with both osteoblasts and osteoclasts. They are able to detect mechanical loads and use this information to regulate bone metabolism and remodeling (Tu et al., 2015). Osteoclasts are large and multinucleated cells, and their duty is bone resorption. Osteoclasts are derived from mononuclear precursor cells of the monocyte-macrophage lineage (B. Clarke, 2008). They can travel to the specific defective sites on the bone surface. They secrete acid phosphatase and enzymes to dissolve inorganic compounds of bone. Thus, they eliminate defective sites in bone. Breaking down defective sites allows bone remodeling and conserves mechanical strength of bone (Lanza, 2014).

2.1.1. Formation of Bone

Bone formation (ossification) occurs through two mechanisms during fetal development: intramembranous ossification and endochondral ossification. Intramembranous ossification is mainly responsible for the formation of flat bones like skull bones. Mesenchymal stem cells (MSCs) residing in the embryonic connective tissue differentiate into osteoprogenitor cells. They further differentiate to form osteoblasts. Osteoblasts clusters and secrete collagen and organic components creating a calcification center and osteoids (Caplan, 2001; Lanza, 2014). Osteoids mineralize with the presence of calcium phosphate and form a bone matrix. Eventually, osteoblasts derived from squamous MSCs create trabeculae. The calcification center becomes an ossification center and osteoblasts become buried in the newly formed matrix, later differentiating into osteocytes. Developing bone becomes a network of trabeculae and forms spongy bone. Also, MSCs at the surface of developing bone condense and creates a dense outer layer which is called periosteum (Fratzl & Weinkamer, 2007). Contrary to intramembranous ossification, endochondral ossification starts with a hyaline cartilage model, which is the first of five steps as shown in Figure 2. In the first step, mesenchymal stem cells differentiate into chondrocytes which anticipates the hyaline cartilage model. The cartilage model has a rough shape of the future bone and consists of the primary ossification center in the middle. Chondrocytes secrete extracellular matrix rich in collagens while the bone draft enlarges (hypertrophy) through proliferation and matrix production. They also synthesize alkaline phosphate for mineralization of the matrix. Meantime, due to the bone collar, there is no nutrition diffusion to the inside of the bone, thus blood vessels are formed around the bone in the fourth step (Lanza, 2014). Then hypertrophic chondrocytes are invaded by specialized osteoclasts (chondroclasts) and undergo apoptosis. In the second step, osteoblasts differentiate into osteoclasts in the periosteum, which is the dense outer layer. As the chondrocytes die and osteoclasts degenerate the calcified regions in the fourth step, they create spare regions for blood vessels to grow into the matrix. Osteoclasts also break down spongy bone and form the medullary cavity which then contains bone marrow (Lanza, 2014; Maes & Kronenberg, 2011).

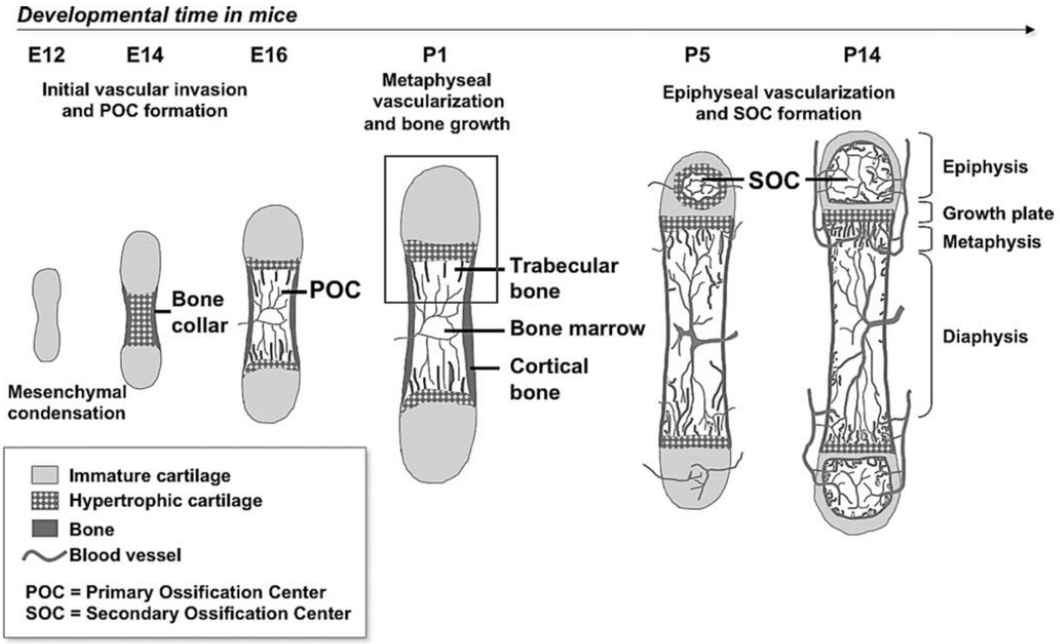

Figure 2: Schematic of endochondral ossification for long bone formation and development *(Maes & Kronenberg, 2011)*.

2.1.2. Bone Healing Cascade

Bone fracture healing is a complex process that involves various proteins and components. Interestingly, during the bone fracture healing of an adult, the morphogenetic signaling pathway activations are the same as the ones during embryonic skeletal development (Einhorn & Gerstenfeld, 2015). Bone fracture healing mechanisms can be divided into two mechanisms: primary and secondary healing (M. Wang et al., 2024). The primary mechanism occurs when the healing process does not require formation of a hematoma. It is possible when the fracture ends are almost aligned and there is no critical-sized defect or gap. Osteoclasts and osteoblasts cooperate in the primary healing, osteoclasts create an empty cross line at fracture site by resorption and then osteoblasts start a remodeling process to fill the empty site with woven bone (Einhorn & Gerstenfeld, 2015).

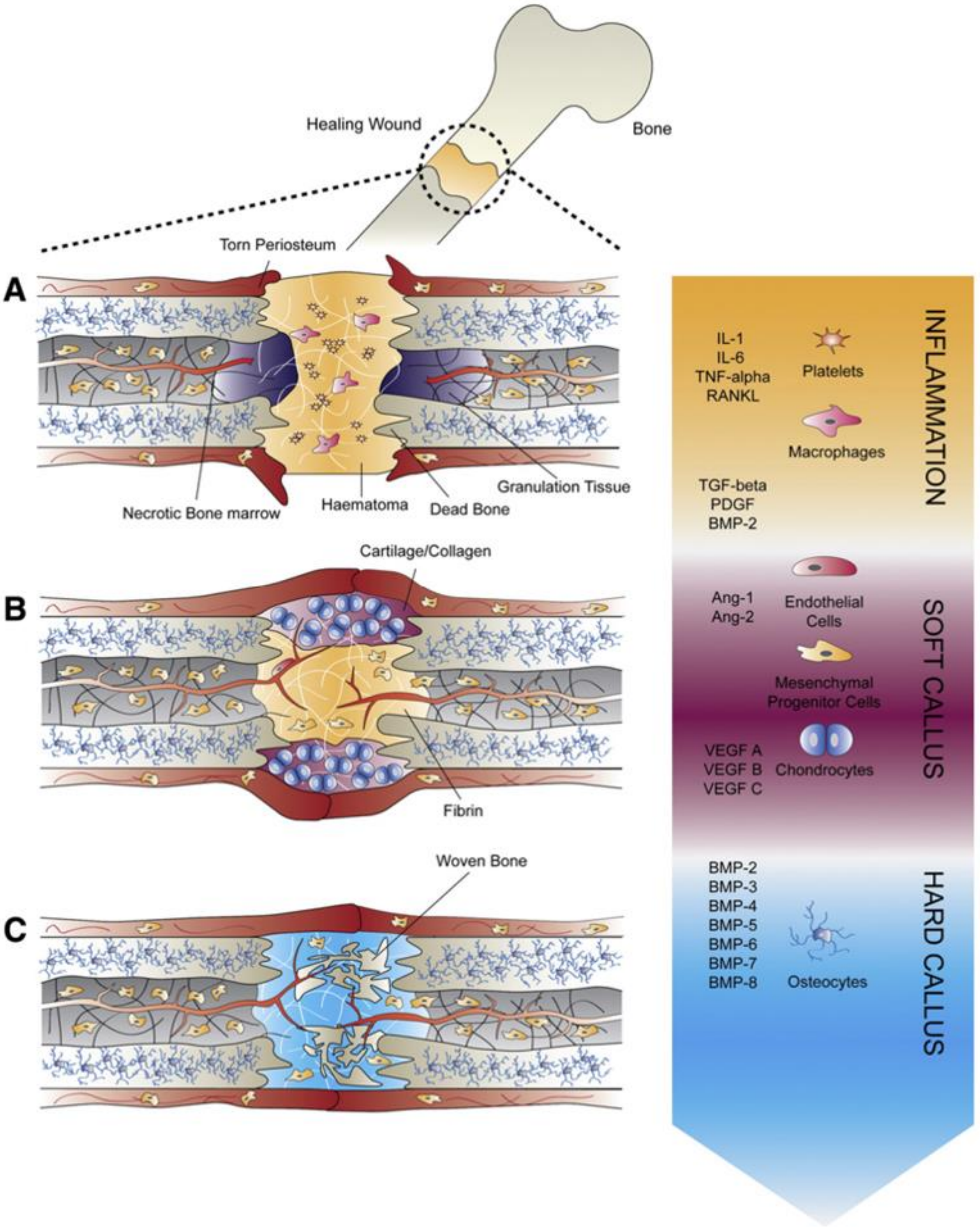

Figure 3: The initial healing can by histological appearance be divided in A) inflammatory, B) soft callus, and C) hard callus phase (Lienemann et al., 2012).

The secondary mechanism occurs if the fracture has a complex shape and its ends are not closely aligned (M. Wang et al., 2024). It is the most common healing mechanism and consists of both endochondral and intramembranous bone formation (Marsell & Einhorn, 2011). It involves some overlapping steps which are hematoma formation, inflammation, revascularization, cartilage formation and mineralization (soft callus), woven bone formation (hard callus), and remodeling as shown in Figure 3 (Hettiaratchi & Coulter, 2016). As soon as the fracture occurs, the injured blood vessels cause the formation of a hematoma (blood clot) around the fracture site. After that, inflammatory cells secrete interleukins, and various cytokines start an acute inflammatory phase. An increasing concentration of these proteins calls mesenchymal stem cells to initiate the soft callus formation which is followed up by hard callus formation and remodeling (Hettiaratchi & Coulter, 2016; Marsell & Einhorn, 2011). Among growth factors that play an essential role in secondary fracture healing, there are transforming growth factor-beta (TGFβ), bone morphogenetic proteins (BMPs), vascular endothelial growth factor (VEGF). Their release and diffusive motion around the fracture site are critical to the healing process (M. Wang & Yang, 2017).

2.2.Polymer Degradation and Drug Release Dynamics

2.2.1. Polymer Degradation

In bone healing studies, biodegradable polymers are frequently preferred together with ceramics or composites. Biodegradability is advantageous for bone healing because it allows complete disappearance of implanted material, eliminating the secondary surgery necessities. Many in vitro and in vivo studies are present in the literature for various biodegradable polymers to investigate their degradation mechanisms (Y. Wang et al., 2008). Understanding the degradation dynamics of biodegradable polymers is one of the crucial concerns of these studies to design a polymeric scaffold that has optimal behavior in vivo. The scaffolds must continue their functions during healing, as an interplay with newly formed bone tissue. This is because the newly formed tissue will take over these functions from the implanted scaffold as it degrades (H. S. Kang, 2010). In the literature, the degradation term is distinguished from erosion considering their phenomenological differences. Polymer degradation is defined as a chain scission process; chemical events that affect polymer backbone such as a decrease in molecular weight of the polymer. On the other hand, polymer erosion stands for the depletion of material, a physical phenomenon namely dissolution and diffusion. Erosion does not affect the polymer at molecular scale; instead, it changes the physical structure of the material (Y. Chen et al., 2011; Siepmann & Gopferich, 2001; Tzafriri, 2000). The literature is richer in studies on polymer degradation dynamics than polymer erosion mode which is a more complex event as it depends on many other processes besides degradation, such as morphological changes and characteristics of the minor products formed (Davison et al., 2014; Von Burkersroda et al., 2002).

Polymer degradation may be induced by oxidation, thermal activation, chemical or mechanical degradation. For biomaterials, chemical degradation plays a greater role depending on their intended purpose. They degraded via three fundamental modes of degradation: hydrolytic degradation, enzymatic degradation and stimuli-associated degradation (D. Yang et al., 2019). Because all polymers have hydrolysable chemical bonds, in a very humid environment like the human body, hydrolysis becomes the most important degradation reaction for biomaterials (Göpferich, 1996; Tajvar et al., 2023). The two primary degradation mechanisms are bulk degradation and surface degradation (Gopferich & Langer, 1993; Von Burkersroda et al., 2002). When the polymer scission takes place at the surface of the material, it affects the outermost layer of the material and does not change the whole geometry during the reaction. As the device ages, its size and weight gradually decrease through the inside. However, its molecular weight and mechanical properties remain constant over time. If hydrolysis occurs randomly and uniformly throughout the bulk material, it is called bulk degradation (Göpferich, 1996; Tzafriri, 2000). In Figure 4, it is shown on the left that bulk degradation causes a uniform change in the material. The degradation fate of the material depends on the interplay between water diffusivity and the hydrolysis reaction rate. The higher the diffusivity of water, the faster it reaches the bulk of the material and its chemical bonds and initiates hydrolysis reaction. If water penetration is slower than the degradation reaction, then it would be limited on the surface of the material. Based on that, materials whose water diffusion rate is higher than the hydrolysis reaction rate, then the material undergoes bulk degradation. Conversely, if degradation rate is higher than diffusion rate, then surface degradation is favored (Davison et al., 2014; Von Burkersroda et al., 2002).

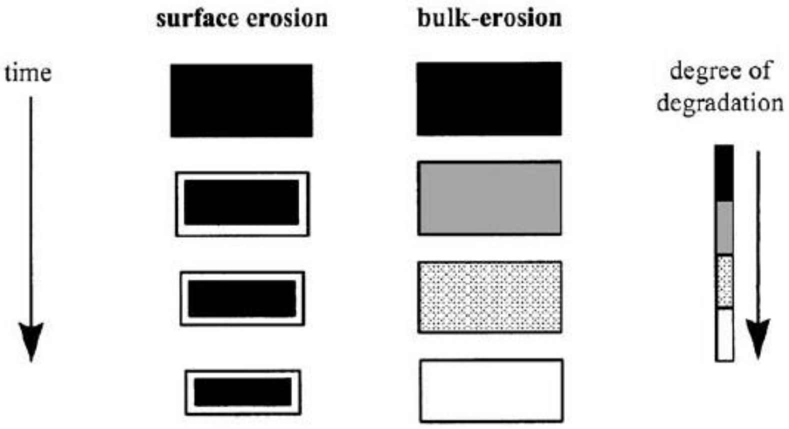

Figure 4: Schematics of change in a polymer matrix during surface and bulk erosion (Von Burkersroda et al., 2002).

As the water penetrates the polymer, the water molecules attack the polymer chemical bonds in the amorphous regions. Water molecules preferably attack ester bonds because anhydrates and ester bonds are the most reactive ones. Destruction of chemical bonds yields short alcohol chains and acids (Siepmann et al., 2005). Although the molecular weight of the polymer and its mechanical properties change throughout the bulk degradation process, they can be conserved by crystal domain chemical bonds until some point (Davison et al., 2014). When the concentration of acidic byproducts (e.g., carboxylic acids) increases due to the cleavage of ester bonds, the low pH environment further catalyzes hydrolysis reaction and thus fastens the overall degradation of polymer. This self-accelerating mechanism is called autocatalysis (Siepmann et al., 2005). Aliphatic polyesters like polyglycolic acid (PGA), polylactic acid (PLA), and poly(ε-caprolactone) (PCL) are the most often utilized biodegradable polymers in medical applications such as drug delivery systems and are known to follow bulk degradation kinetics in the literature (H. S. Kang, 2010). Their polymer backbone has carboxylic acid end groups on one end and hydroxyl end groups on the other so that their hydrolysis process is an auto catalyzed degradation (Davison et al., 2014; Siepmann et al., 2005).

Enzymes also play a significant role in the degradation of biodegradable materials through a process known as enzymolysis. Enzymolysis involves enzymes catalyzing the scission of polymer chains, critically impacting the degradation rate of polymers in physiological environments (H. Zhang et al., 2014). Enzymes can degrade polymers through hydrolytic or oxidative reactions. Hydrolytic enzymes such as phosphatases, esterases, and proteases, which are abundant in the body, accelerate the breakdown of scaffolds by catalyzing hydrolysis reactions. Enzymatic degradation is mostly limited to surface erosion due to the larger size of enzymes that prevents their penetration into the scaffold. Hence, enzyme availability is restricted to the exterior. Containing paths, cavities, and pore sizes inside the material ease enzyme movement throughout the material. Enzymes' ability to form a complex with their substrate increases as the degradation proceeds because of the formation of micro and macropores (Tajvar et al., 2023; D. Yang et al., 2019; H. Zhang et al., 2014).

The degradation behavior of polymers depends on various factors including material structure, its chemical composition, molecular weight, crystallinity, hydrophobicity, mechanical stress, water diffusivity and environmental factors such as pH and temperature(Gopferich & Langer, 1993). There may be a significant feedback impact of some of these parameters on the degradation velocity. Molecular weight is the most crucial quantity for tracking degradation. In addition to molecular weight loss, other measures such as mechanical strength loss, total breakdown into monomers, or monomer release have been suggested as indicators of degradation. Although they are all connected, they do not all have to follow the same dynamics. Since they have more bonds to break, higher molecular weight polymers usually degrade more slowly(Göpferich, 1996). Hydrophobic polymers such as PCL and PLA degrade more slowly due to lower water uptake(Meyer et al., 2009). The rate of degradation can be altered by the copolymer make up; for example, hydrophobic polymers' degradation velocity can be sped up the rate of hydrolysis upon the addition of hydrophilic substitutes. Hydrolysis may also be catalyzed or retarded by environmental conditions, including pH levels; degradation is usually faster in acidic or basic medium than under neutral conditions. Therefore, the diffusion of the shorter chains out of the polymer plays a key role in controlling the overall degradation rate. As a result of this interplay between diffusion and hydrolysis reaction is that a thicker plate degrades faster than a thinner one, as the short chains with acid end groups cannot diffuse out quickly enough, leading to an acidic environment build-up inside the thicker plate and autocatalysis (Göpferich, 1996; H. S. Kang, 2010; Y. Wang et al., 2008).

Material structure and geometry also affect degradation behavior of the materials. The pore size and porosity are effective parameters for degradation behavior of scaffolds since an increasing porosity creates a larger surface area and increases the interconnectivity of pores. The higher surface area allows more contact domains for water molecules with the material resulting in higher degradation rate and dominant surface degradation mode. Moreover, when the water contact area is larger, the formation of acidic byproducts, which cause an autocatalytic effect, fastens the degradation. On the other hand, the higher pore interconnectivity enables higher water permeability. If fluids' diffusivity is easier, the accumulation of the byproducts is reduced which decreases the effect of autocatalysis. Thus, the porosity of scaffolds has a great importance on degradation mode by tailoring the water permeability and hydrolysis effect (Raja et al., 2022; Q. Zhang et al., 2013).

2.2.2. Growth Factor Release

Bone is a highly regenerative organ which follows a certain healing process after injury, which necessitates external treatments such as grafts for effective healing in large or non-union defects. Bone scaffolds serve as supportive materials for these types of fractures by both mimicking extracellular matrix and providing mechanical strength. They should be biocompatible and biodegradable, also have an appropriate material characteristic to enhance osteoinductive cells' attachment and proliferation on their surface; having a porous structure to provide cavity for vascularization and new tissue growth and an ability to load and deliver bioactive molecules or drugs (De Witte et al., 2018; É. R. Oliveira et al., 2021).

Drug delivery systems for bone tissue engineering, not necessarily a 3D scaffold, aim to provide the loaded molecules effectively to enhance signaling pathways initiated by their release from native extracellular matrix. They are designed to control spatial and temporal release dynamics (É. R. Oliveira et al., 2021). Traditional ways of systematic drug administration to the body are not an effective solution for bone healing, since drugs are absorbed and distributed to the body by the vascular system and finally removed. Consequently, bone, which is not a highly vascularized organ, cannot benefit from the given dosage while unrelated organs are exposed to the drug (Ghosh et al., 2018). Drug delivery systems can be engineered to achieve controlled release through mechanisms such as diffusion, dissolution, swelling, matrix erosion, and osmosis. Polymer-based scaffolds have been found to be very appropriate as carriers due to their tailorable material properties to manipulate various parameters related to release mechanisms (S. R. P. Oliveira et al., 2024). Moreover, bioactivity potential of both natural and synthetic polymers can boost osteoinductivity with deposition of growth factors, transcription factors, genes or mesenchymal stem cells (Rama & Vijayalakshmi, 2023; Sharma et al., 2021). Furthermore, delivering multiple drugs having different physiochemical properties is possible without varying their therapeutic efficiency via polymeric scaffolds (S. R. P. Oliveira et al., 2024)Synthetic polymers such as PLGA, PLA and PCL are the most widely examined ones in drug delivery applications. Among them, PLGA is a copolymer which is formed of PLA and PGA exhibiting an excellent example of tailoring polymer properties for specific purposes. Consisting of different ratios of PGA and PLA helps alter properties of PLGA such as molecular weight, degradation rate which affects release profile of the loaded drugs (S. R. P. Oliveira et al., 2024; Sharma et al., 2021).

Drug release mechanism from polymer matrices depends on the physical and chemical characteristics of the polymer and can be classified into three systems. Although the concentration gradient is always a driving force in all, the degradation fate of the polymer distinguishes these three systems. In the first, only diffusion is involved in non-biodegradable polymers. If the polymer undergoes a swelling process, it enhances the diffusion dynamics and can be treated as a second release system. For biodegradable polymers, release dynamics depend on the interplay between polymer cleavage and diffusion (Arifin et al., 2006; Leong & Langer, 1987). The release of drug occurs only from the surface of non-biodegradable polymer matrices which limits its tuning abilities to mainly pore size (Calori et al., 2020). In contrast, in the cases of employing degrading polymer as a delivery system, the release mechanism is in accordance with multiple processes affecting polymer degradation in addition to interactions between drug and polymer such as diffusivity of drug through the polymer (Tzafriri, 2000). Physical and chemical interactions between drug and polymer molecules, such as van der Waals forces, hydrogen bonds, and electrostatic interactions have a great impact on release rates. Strong physical interactions result in slow drug release rates. By contrast, weaker physical interactions yield a faster release of the drug before the release rate reaches a steady profile at the implantation. It is called burst release which is mostly undesired but frequently occurring (X. Huang & Brazel, 2001; Sharma et al., 2021). Dissolution of drug in the polymer and unfavorably fast polymer degradation would also yield burst release. Drug release studies often mention burst release cases and researchers seek ways to avoid the burst due to toxic effects of high concentration of drugs at the implantation site, high cost of production of biological molecules in vitro, bioactivity loss of proteins after release due to their short half-lives, and the need for additional dosing in the late stages of treatment (X. Huang & Brazel, 2001; É. R. Oliveira et al., 2021; Schrade et al., 2022).

For example, Yin et al. showed that blood vessels formed under high doses of VEGF can exhibit morphological abnormalities and leakage. Additionally, angiogenesis can contribute to pathological changes, including tumor formation, arteriosclerosis, and retinal proliferative diseases(Yin et al., 2019). Nevertheless, burst release might be an optimal delivery mechanism in some cases where high release rates are pursued (X. Huang & Brazel, 2001).

Bioactive signaling molecules play vital roles in bone regeneration. Growth factors such as bone morphogenic proteins (BMPs), transcriptional growth factor beta (TGF-β), vascular endothelial growth factor (VEGF), fibroblast growth factors (FGFs) and insulin-like growth factors (IGFs) are essential for stimulating specific signaling pathways for bone formation, cell differentiation or angiogenesis. They are involved in different phases of the bone regeneration process. BMP-2 is the growth factor most frequently used to stimulate bone formation in humans and studied for drug release for bone regeneration. Recombinant human BMP-2 is not only a US Food and Drug Administration (FDA) approved growth factor, but also a collagen implant for its delivery together with other growth factors is the first FDA approved implant (Calori et al., 2020; Takayama et al., 2023). Growth factors can be attached to scaffolds through physical or chemical methods, including adsorption and chemical cross-linking. They can be physically entrapped within the scaffold during production. Other than physical entrapment, GFs can be caged in the scaffold via formation of ionic complexes. The chemical binding methods include covalent or noncovalent binding of GF to the scaffold. Both covalent and ionic attachments require modifications in functional groups on the scaffold surface. Due to the stronger interactions in covalent binding, it can prevent burst release and prolong the release duration (De Witte et al., 2018). Fibrin-based matrices are frequently utilized due to their ability to bind growth factors, such as basic fibroblast growth factor (b-FGF) and BMP-2, through heparin-binding sequences. Schrade et al. investigated the release from gelatin nanoparticles which shows an incorporation with heparin binding sites. They proved that this interaction significantly prolonged the release, reducing the initial burst and providing a more sustained release profile (Schrade et al., 2022). Additionally, it has been shown that BMP-2 loaded heparin-functionalized nanoparticles are shown to drastically improve bone regeneration compared to control groups which consist of only fibrin gel and not heparin binding sites (Chung et al., 2007). These GFs are covalently cross-linked to fibrin during enzymatic coagulation, a process enhanced by adding heparin or hyaluronic acid to the fibrinogen mix. The release of GFs from these matrices occurs passively as the fibrin and heparin degrade simultaneously, resulting in a relatively rapid release rate. To achieve a slower and more controlled release of GFs, various encapsulation methods have been developed. Encapsulation creates a physical barrier that prevents the diffusion of GFs until the encapsulating material degrades sufficiently. By adjusting the composition of the capsule, the degradation rate and subsequent release of the entrapped GF can be managed. Bioresorbable polymers, particularly aliphatic polyesters, are commonly employed for this purpose. These polymers initially undergo random hydrolytic breakdown of their amorphous regions, followed by surface erosion, which then exposes and releases the GFs in a controlled manner (Hettiaratchi & Coulter, 2016).

Dual delivery systems that combine multiple growth factors or drugs can enhance osteogenesis and angiogenesis, improving bone healing outcomes (Blackwood et al., 2012). Patel et al. investigated the effects of dual delivery of VEGF and BMP-2 on bone regeneration in a rat cranial critical size defect model (Patel et al., 2008). Their findings indicate a synergistic effect of the dual delivery of VEGF and BMP-2 on early bone regeneration. The addition of VEGF enhanced early-stage bone formation but did not significantly impact the total amount of bone formed (Patel et al., 2008). Another study employed BMP-2 and IGF-1 with a nanocomposite scaffold and investigated their dual release kinetics and effect on osteogenesis. They obtained a controlled and sustained release of both growth factors resulting in enhanced osteogenic differentiation and mineralization compared to single growth factor release (Kuttappan et al., 2018).

In this thesis, the release of BMP-2 is considered from a degrading CaP scaffold. The release system is both driven by the degradation of the scaffold and diffusion of BMP-2 from the eroding surface through the water and scaffold domains.

2.3.Background for Biological Signal Transduction Events

Developing cures for health problems requires a deep understanding of how a living body operates, which is incredibly complex. Traditional biology approaches were mainly limited to individual parts of this highly hierarchical system which prevented understanding complex interactions. The exponential evolution of research tools and computational technologies eliminates the limitations of figuring out the interactions between biological components and providing on-target solutions (Bing, 2005).

However, the biological entities and their properties include various time and length scales such as from seconds to years or nanometers to meters. Furthermore, the hierarchical structure of biological components encompasses different organization levels lying down between tissues, organs to cells, molecules and even to atomic interactions. Systems biology is an interdisciplinary field including computational sciences, genomics, measurement techniques and aims to achieve an in-depth understanding of biological system behavior (Klipp et al., 2016). Studying biochemical pathways and gene regulatory systems are the major challenges because conventional methods require large experimental designs for these interactions. Also, they are essential for cellular behaviors and gene regulation predictions. Biochemical dynamics modeling needs a broad biological background as well as a mathematical base because they are mostly established on basic physical laws such as mass conservation law and thermodynamics which requires solving system of equations for multivariable models. Since experimental studies are mostly inadequate in generalizing and validating widespread hypotheses due to the complexity of the networks, the emerging field of computational sciences allows model approaches for these complex regulatory networks and eases the analysis of spatio-temporal dynamics (Kitano, 2002). Moreover, necessitating less experimental work reduces high costs and laboring of experimental studies while helping to eliminate ethical issues and harming animals. Another advantage of using computational tools, the mathematical terms are tunable for different signaling networks and understanding the parameter dominance with single perturbations due to its repeatability. Nevertheless, the essential goal of a model or a simulation is to approach reality and experimental results (Klipp et al., 2016).

2.3.1. Signal Transduction Events in Bone Regeneration and Repair

Bone regeneration consists of a series of well-constructed induction and conduction following the above summarized biological events. Current approaches to BTE gain significant attention to design effective bone scaffolds that are able to provide an appropriate environment for bone repair. Satisfying the requirements of a well-designed bone scaffold necessitates understanding the mesenchymal stem cells’ differentiation ability, the importance of growth factors and transcription factors that have essential roles in endochondral ossification (Majidinia et al., 2018).

ECM molecules and cells can communicate with a wide range of receptors to carry out controlled reactions to changes in their environment via complex signal transduction pathways. Signaling ligands interact with receptors within or on the surface of target cells to facilitate communication between cells. These interactions cause the cell's signaling pathways to become active, which in turn modifies the levels of gene expression and protein activation. These modifications have an inevitable effect on the cellular processes of adhesion, migration, proliferation, differentiation, and death (Klipp et al., 2016). All cellular communication follows a cascade-like process, despite possible differences in the signal transduction routes and responses: When a ligand attaches directly to its receptor, the signal is transduced and augmented inside the cell by enzymes and second messengers, and the cell reacts accordingly. Signal transduction pathways, also known as cellular responses, can have a variety of effects, such as triggering the transcription of target genes or opening or closing an ion channel (Lanza, 2014; Mark Saltzman, 2009). Adhesion receptors can function as transmembrane signaling molecules, mediating signals initiated by growth factors or substances that regulate gene expression, phenotypic modulation, cell replication, differentiation, and apoptosis. These signals can travel all the way inside cells, sometimes even to the nucleus. Secreted factors modulate cell-cell communication in the normal and pathologic regulation of tissue growth and maturation, despite the fact that some ligands with which cells interact are immobilized and not in solution, such as the integrins which are the principal adhesion receptors mediating cell-ECM attachment (Lanza, 2014). The complex connections that regulate tissue development, homeostasis, and regeneration are actually brought about by the variety of particular bindings of specialized stimuli with cell-surface receptors (Figure 5) (Ratner et al., 2013).

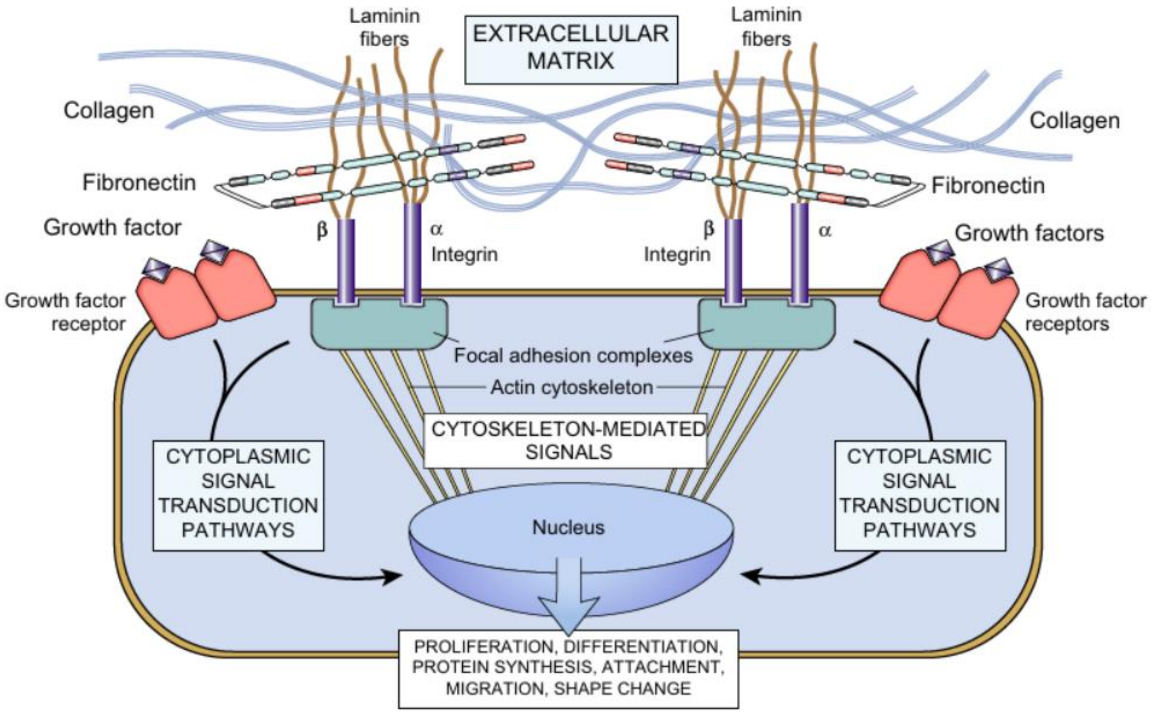

Figure 5: Schematic representing integrin-ECM molecules interactions. Growth factors stimulate receptors to activate signaling pathways (Ratner et al., 2013).

Signaling pathways commonly use phosphorylation and dephosphorylation events which add and remove phosphate groups, respectively, to turn on and off enzymes. Phosphorylation of proteins is a significant modification that the cell uses to aid in the signal's passage from the receptor to the final effector enzyme. The addition of phosphate groups to certain protein amino acid residues is catalyzed by kinases. Kinase cascades or a sequence of kinase events are used in many signal transduction pathways. A sequence of phosphorylation processes known as a "kinase cascade" occurs when one protein phosphorylates another, which phosphorylates still another (for example, kinase A phosphorylates kinase B, activating it to phosphorylate kinase C). Phosphorylation frequently results in the activation of a transcription factor and thereby the expression of specific target genes (Ratner et al., 2013).

2.3.2. Common Signaling Pathways for Bone Regeneration

A large variety of molecular signaling pathways are involved in bone repair and regeneration. Proteins are not responsible for a single duty in these processes and have complex regulatory connections between them including crosstalk events. Growth factors are cell-secreted proteins which serve as signaling molecules for cell-cell interactions by binding of target cells' surface receptors (Figure 5). The binding of growth factors to receptors activates a series of signal transduction events starting from the cell surface and laying down to the nucleus until the expression of target genes inside the nucleus (Hayrapetyan et al., 2015). Numerous studies have shown that many growth factors have crucial roles in in osteoblast activity and local bone formation such as bone morphogenetic proteins (BMPs), transforming growth factor-betas (TGF-βs), Wnts, fibroblast growth factors (FGFs), platelet-derived growth factors (PDGF), and insulin-like growth factors (IGFs) (Majidinia et al., 2018).

BMPs are growth factors belonging to the TGF-β superfamily. The process of fracture healing, adult skeletal maintenance, and endochondral ossification all are affected by BMP signaling (Majidinia et al., 2018). Besides the common feature of BMP-2, BMP-4, BMP-6 and BMP-9 is being an osteogenic regulation factor and BMP-7 is an osteoblast differentiation factor, each has distinct roles via different down regulatory molecules in endochondral ossification (Nasir et al., 2023). BMP-2 is the most researched, including many clinical applications, and commercialized one among BMP proteins (Majidinia et al., 2018). BMP-2 preserves bone homeostasis and its strength by tightly regulating numerous osteoblast and osteoclast balance. BMP-2 expression is elevated following bone damage, which facilitates MSC recruitment and osteoblast development at the fracture site. Research has demonstrated that a lack of BMP2 hinders the healing of fractures, emphasizing the crucial role that BMP-2 plays in bone regeneration (Celil et al., 2005; Rosen, 2009). According to the studies, lack of BMP-2 secretion from skeletal cells causes a considerable delay in the formation of secondary ossification centers in limb's endochondral bones. Also, microfractures were observed even two weeks after its birth that these findings were associated with circumstances of highly loading and compressions would result similarly in adult bone in the lack of BMP-2 (Rosen, 2009).

BMP and TGF-β signaling cascades send signals to cytoplasm via both canonical (Smad-dependent) and non-canonical (Smad-independent) pathways. Even though transcription factors in their downstream are different, they are both activated via BMP receptors type

I (BMPR-I) and type II (BMPR-II) (serine/threonine kinases) (Khotib et al., 2021). In the canonical pathway, the receptor kinase phosphorylates Smad proteins in response to ligand activation, and these proteins subsequently translocate to the nucleus to initiate the transcription of particular target genes. On the other hand, the non-canonical pathway induces osteoblast differentiation through mitogen-activated protein kinases (MAPK) and then p38 transcription factor activation which is a member of the stress-activated protein kinases (SAPKs). Both TGF-β and BMP have been shown to activate this pathway (Lee et al., 2002). Mitogen-activated protein kinase (MAPK) cascade is widely studied in the literature, and it regulates a variety of physiological processes, including osteogenesis, cell movement and death. MAPKs activate other kinases, such as ERK and c-Jun N-terminal kinase (JNK), which subsequently activate key transcription factors like Runx2 and Sp7/Osterix (Osx) via Sp1, promoting the expression of genes involved in osteogenesis (Camal Ruggieri & Feldman, 2020; Hayrapetyan et al., 2015). Thus, the crosstalk between BMP and TGF-β is essential for the regulation of osteoblast differentiation and the transcriptional activity of Runx2 through non-canonical BMP signaling (Lee et al., 2002).

In the canonical BMP signaling pathway, Smad1, Smad5, and Smad8 are phosphorylated by BMP receptors and transmit its signals, Smad2 and Smad3 are phosphorylated by TGF-β receptors and promote TGF-β signaling (Lee et al., 2002). There are 8 different Smad proteins in mammals. Based on their functioning, they are divided into three classes. The first one is receptor-regulated Smads (RSmads) which includes Smad1, 2, 3, 5, 8. They are activated after binding of BMP-2 and -4 to the type I and II receptors for gene regulation. The second group is called co-mediating Smad and only Smad4 belongs to this group. It has a crucial role in canonical BMP signaling since it binds to phosphorylated RSmads and helps translocate them through cytoplasm to the nucleus for transcription. The last category of Smads is I-Smads that include 6 and 7. They negatively contribute to BMP signaling due to their inhibitory effect (Song et al., 2009; Zou et al., 2021). Both in the absence and in the presence of TGFs, Smads continually enter and depart the nucleus. Stable nuclear Smad accumulation during active signaling is actually dynamically maintained by ongoing cytoplasmic RSmad phosphorylation and nucleus R-Smad dephosphorylation (Schmierer et al., 2008). After being exposed to TGF-β for about 20 minutes, cells reach a stable level of Smad2 and 3 phosphorylation that can last for many hours. When TGF-β concentration decreases in the extracellular space, Smad phosphorylation eventually fades away. This is due to the receptor deactivation through internalization and degradation, or the operation of negative feedback mechanisms (Kopf et al., 2012). The under-phosphorylated condition of Smad2 protein exported from the nuclei suggests that RSmad dephosphorylation takes place in the nucleus. Dissociation of the RSmad–Smad4 complex and export of its constituent parts to the cytoplasm occur concurrently with dephosphorylation. As long as TGF-β receptors are present, RSmads will repeatedly cycle through receptor-mediated phosphorylation and re-entry into the nucleus maintaining their total presence in the cellular space in the meantime (Massagué et al., 2005; Song et al., 2009). Wang et al. emphasized that Smad proteins constantly shuttle between the nucleus and the cytoplasm in order to sustain active signaling. It was highlighted that Smad1/5/8 by BMP receptors and Smad2/3 by TGF-β receptors are phosphorylated, which is essential for target gene transcription and signal propagation (Q. Wang et al., 2023). In a very similar manner, Lang et al. reported that osteoprogenitor recruitment and maintenance were compromised by Smad1/5 suppression, which decreased the amount of Osx osteoprogenitor cells, primarily in the metaphysis. Additionally, after Smad1/5 depletion, there is a notable decrease in bone volume fraction (BV/TV) and Osx in mRNA expression in the metaphysis (Lang et al., 2024). Huang et al., have shown that the phosphorylation of Smad1 stimulates osteogenic marker genes Runx2, ALP, bone sialoprotein (BSP), osteopontin (OPN), and osteocalcin (OCN) to promote bone formation under BMP-2 treatment (D. Huang et al., 2020). BMP-2 could trigger mesenchymal cells to differentiate into osteoblast lineage by activating Smad1/5/8. Shortly, for the importance of Smad4 together with other, reduced bone mineral density, volume, velocity of bone formation, and osteoblast count are all consequences of conditional deletion of Smad4 in osteoblasts due to the need to transport phosphorylated Smads. Zhang et al. implied that an efficient way of regulating bone formation is to control Smad4 (Figure 6) (G. Zhang et al., 2020). These findings demonstrated that Smad1/5/8 are intracellular signaling proteins that transduce signals elicited by members of BMP signaling in osteoblasts (G. Chen et al., 2012; D. Huang et al., 2020).

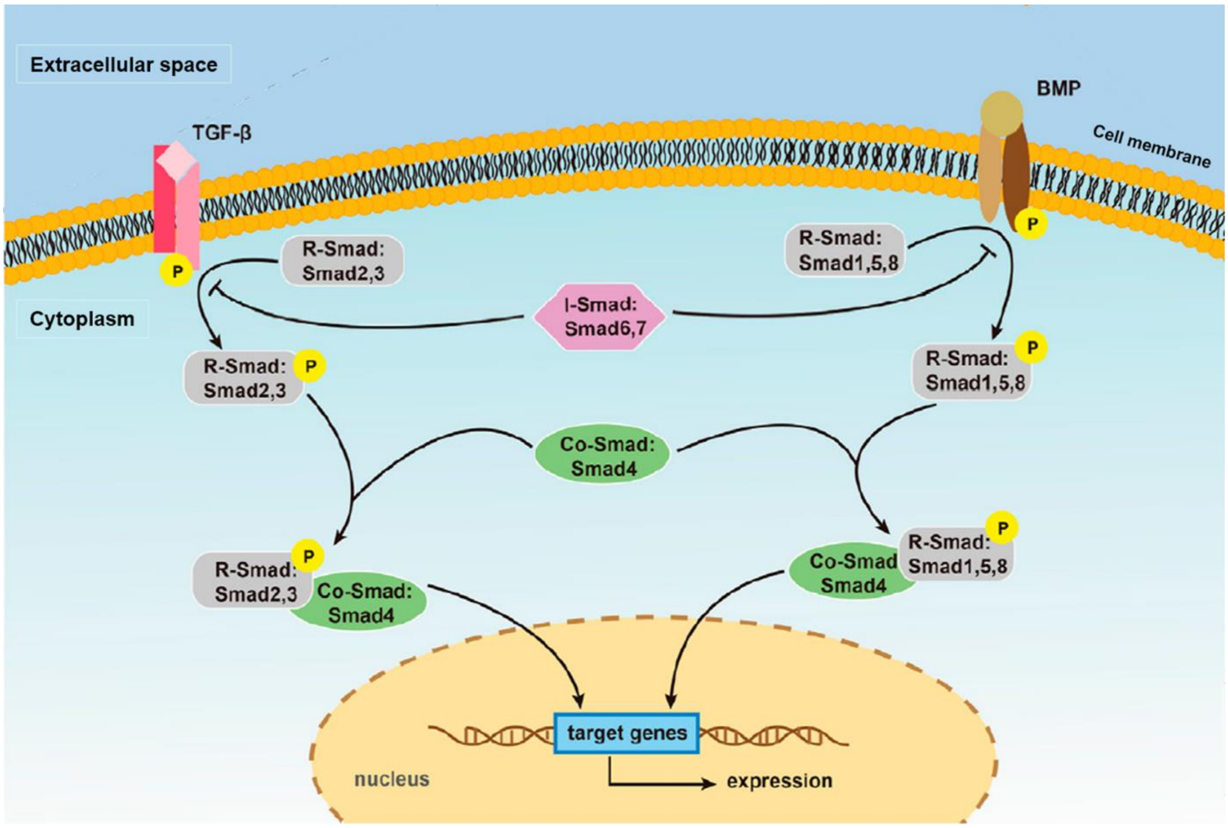

Figure 6: Activation of canonical TGF-β/Smad and BMP/Smad pathways leading to gene expression (Zou et al., 2021).

Runx2 is a master-regulatory transcription factor for bone formation since it strictly controls osteoblast and chondrocyte differentiation through various signaling pathways. Furthermore, Runx2 is crucial for the proliferation of chondrocytes and osteoblast progenitors, and matrix protein gene expression in both chondrocytes and osteoblasts (Komori, 2005; Lee et al., 2000). It is an early osteogenic marker which can directly bind to osteoblast-specific elements to downregulate several genes such as OPN and OCN (Thaweesapphithak et al., 2023). Consequently, Osx prompts pre-osteoblasts to differentiate into osteoblasts by activating terminal osteogenic marker genes, including BSP, OPN, and OCN since Runx2 is a direct regulator for Osx (D. Huang et al., 2020; Komori, 2022). Typically, one of the first markers to be produced when mesenchymal stem cells (MSCs) differentiate into osteoblasts is COL1A1. It has a role in the extracellular matrix's early development (Komori, 2022). OPN is involved in cell adhesion, motility, and signaling and is expressed early in osteogenic differentiation. By activating terminal osteogenic marker genes, Osx, a downstream target of Runx2, further initiates the differentiation of preosteoblasts into mature osteoblasts, serving as a marker for subsequent stages of osteogenic differentiation (Z. Huang et al., 2007). Because of chondrocyte maturation and cartilage matrix breakdown brought on by Runx2 overexpression in the articular cartilage, osteoarthritis will result. is thought to serve as a marker for osteogenic differentiation's later phases. OCN is a non-collagenous protein that osteoblasts release and is present in dentin and bone. It is connected to the mineralization stage of bone development and is thought to be a late indication of osteogenic differentiation (Tohmonda et al., 2011).

In this thesis, we selected a compact version of the canonical pathway of BMP-2. As described earlier, the canonical pathway is the Smad dependent pathway activated by BMP-2. Runx2 is important for signaling pathways consisting of Smad proteins, and it strictly regulates Osx. Thus, selected Smads, Smad1/5, Runx2 and Osx forms the signaling pathway considered in the present work.

2.4.Numerical Methods in BTE

In bone scaffold modeling, computational methods are employed to simulate and optimize the design, function, mechanical properties and biological interactions of scaffolds at various levels, from tissue to cellular. Computational methods have greatly aided the field's advancement by providing insightful and predictive capabilities, thus minimizing the need for lengthy experimental trials. The production of better-performing and reliable scaffolds can be improved by using these computational methods, which enable accurate prediction of scaffold performance under physiological environments, mechanical property optimization, and simulation of cellular interactions. However, experimental methods are closer to reality and their results attained from are more likely to be applied in clinical studies (N. Musthafa et al., 2024). This part aims to give insights on previous studies about the drug release, degradation, intracellular signaling pathways, and optimization algorithms used in BTE computations.

Traditionally, scaffolds are created and modified based on the outcomes of in vitro and in vivo experiments. This iterative approach is very costly, time-consuming, and occasionally lacks precise control over the scaffold's properties. Considering the aim of bone tissue scaffolds, the scaffold design part must be supported with biological experiments which are additional iterative steps for a comprehensive study. Many studies are present in the literature aiming to find optimal mechanical properties for various designs of bone tissue scaffolds. Because computational methods such as computer-aided design (CAD), FEA, and computational fluid dynamics (CFD) are great tools to reduce the iterative steps of experimental studies, they have been employed to obtain findings that are hard to get experimentally such as stress-strain curves or compression analyzes of scaffolds (S. Zhang et al., 2019a).

Computational methods are useful regardless of which scale is considered in bone regeneration such as scaffolding, cellular activities or intracellular pathways. In tissue level, FEM, CFD and reaction-diffusion type partial differential equations (PDEs) are mostly used. CFD simulations are important in this field since the body consists of various types of blood vessels which provides room for continuous blood flow and nutrient/oxygen transport. It is known that cellular activities require continuous access of blood via vessels. Another aspect of its importance is that the scaffold’s pore size and interconnectivity affect the movement of interstitial fluid and CFD studies are useful for optimizing the flow dynamics. Ordinary differential equations and PDEs are keystones to model and solve real life engineering problems (N. Musthafa et al., 2024). Thus, reaction-diffusion PDEs are used in all levels of bone healing, including growth factor release, scaffold degradation, receptor-ligand interactions for signaling pathway activation, transcription factor dynamics through gene transcription in the context of this study. While PDEs provide a spatio-temporal evolutions of considered variables, concentrations of species such as GFs and TFs, ODEs are generally used to evaluate time dependent kinetics of signaling cascades.

Three methods have primarily been used to model the scaffold degradation behavior: phenomenological (using the diffusion, reaction, and dissolution governing equations), probabilistic (using the Monte Carlo technique to apply the probability distributions of the kinematics of molecules), and empirical (based on test data via regression tactics) (S. Zhang et al., 2019a). The aforementioned techniques can be used to forecast the temporal and geographical changes in scaffold properties together with the growth factor release dynamics, allowing for the regulation of scaffold degradation and drug delivery to correspond with the pace of tissue regeneration.

The system-level mechanisms of biological processes can be better understood by utilizing experimental data from small-scale investigations and high-throughput technology. Quantitative models, particularly those applying systems theory to chemical kinetics, have been used to describe metabolic networks, signaling pathways, and gene regulation (Piñero et al., 2018). Whereas the computational methods are divided into two generalized sections which are top-down and bottom-up (knowledge-based), some other studies classified them as logical, continuous and single molecule levels (Karlebach & Shamir, 2008; Le Novere, 2015; R. S. Wang et al., 2012). The top-down methods include statistical analysis and static network models and are used on high-throughput omics data to extract information unique to a biological process and interpret the structure of underlying systems. Conversely, the bottom-up techniques simulate the ways in which metabolites, proteins, and genes interact to produce the dynamic behaviors of biological systems. Usually, they are built-up on theories derived from small-scale research and use continuous dynamic modeling approaches for the dynamical behaviors (R. S. Wang et al., 2012). The bottom-up techniques include discrete and continuous dynamic modeling. Discrete models, which are increasingly being used to model biological networks, are suitable for systems with hundreds of components and do not require kinetic parameters. Examples of this type of modeling are Boolean network models, multi-valued logical models, and Petri nets (Figure 7) (Le Novere, 2015).

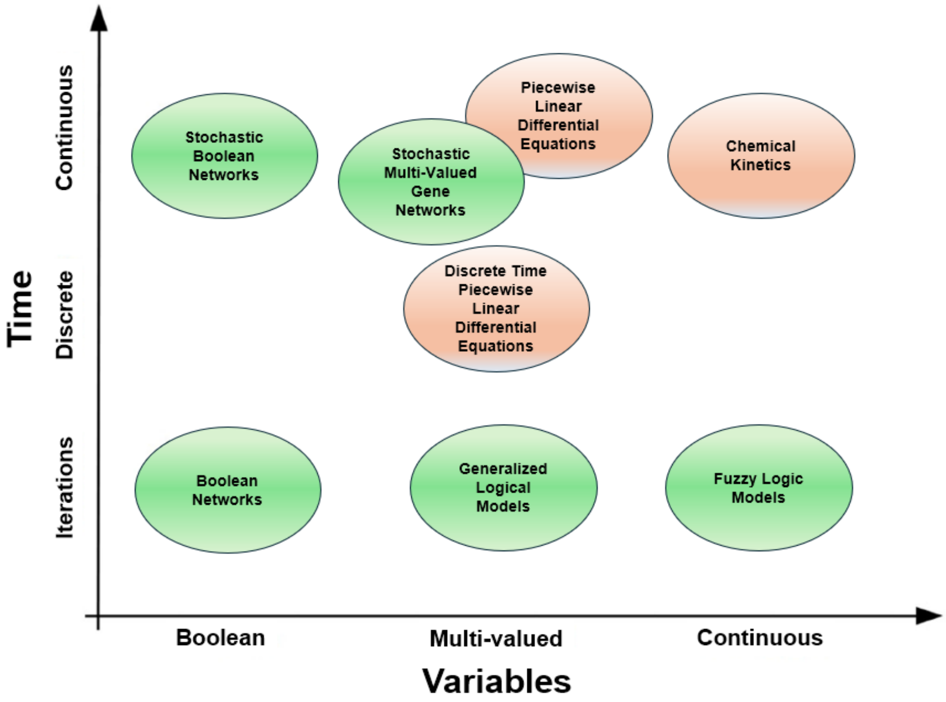

Figure 7: A representative schematic for different modeling approaches based on their time and variable consideration. The green ones use logic-based methods while the orange ones evaluate changes in variables with quantitative mathematical methods. The figure is adapted from (Le Novere, 2015).

FEM is a mathematical model that allows for a more straightforward analysis by discretizing a continuous medium into multiple smaller elements while maintaining the original geometry features. It is used to solve partial differential equations (PDEs) in real-time engineering issues. This ability is useful for modifying the morphological properties of scaffolds in order to optimize them (Liu et al., 2021). In FEM, the meshing process divides the scaffold geometry into a finite number of elements. In general, the accuracy and precision of simulation results are improved by increasing the number of finite elements, but this also increases computation time. FE meshes and material characteristics are combined in a FE model (Sorgente et al., 2023). FEM can be used to forecast how the scaffold will behave when it's in use. Because it is a methodical approach, its solution may be applied computationally, increasing the ability to handle equations and resolve challenging issues. As a result, FEM has been expanding into other fields, including medicine and the treatment of bone fractures. Comparing FEM to in vitro and in vivo experiments which are used to investigate the recovery process of certain tissues allows for a non-invasive investigation. These are costly, time-consuming experiments that address moral dilemmas. Very recently, Zamani et al. employed FEM to model the mechanical environment factors like stress, strain, and fluid flow in the fracture site using a 2D geometry (Zamani & Mohammadi, 2024). It also facilitated the modeling of mechanobiological processes such as the migration and differentiation of mesenchymal stem cells (MSCs) and angiogenesis. They introduced weak forms of reaction-diffusion equations and applied FEM to discretize their governing equations for calculating affecting parameters, which influence cellular activities and tissue metabolism during fracture healing. Similarly, Yang et al. developed a FEM framework for bone fracture healing to modify element properties according to mechanical and cellular events and angiogenesis (Y. Yang et al., 2024). For complex domains and initial/boundary conditions, such as the curved shape of bones, FEM offered a strong framework (Zamani & Mohammadi, 2024). It is essential for understanding the synchronization of cellular dynamics during fracture healing and for making precise predictions about tissue differentiation. Boccaccio et al. used FEM to evaluate mechanical performance under different boundary conditions (compression, shear, lateral pressure) to determine the best scaffold architecture (Rodríguez-Montaño et al., 2019). By simulating different load conditions and scaffold designs for randomly oriented scaffolds, the study optimized the diameter of scaffold beams to achieve the most favorable mechanical environment for bone growth (Rodríguez-Montaño et al., 2019). Additionally, FEM was more stable and efficient in terms of more realistic representations than conventional finite difference techniques, which made it a useful tool for biomechanical study (Zamani & Mohammadi, 2024).

Finite element analysis-based optimization approaches have been utilized to model the mechanical interaction between implants and bones outside of the human body. Nevertheless, there is a lack of data in literature for totally implementing FEM outputs to in vivo research. Therefore, to make the optimization method more therapeutically applicable in the future, biomechanical study in the human body will be required (Wu et al., 2023).

In this thesis, we have employed a FEM based solver COMSOL Multiphysics version 5.4 for initial validation study explained in Chapter 3 and 6.1 to numerically solve the governing PDEs of 3D scaffold degradation and growth factor release. We have used the Chemistry interface to define chemical reactions representing scaffold and BMP-2 degradations and release of BMP-2, and transport of diluted species (TDS) module for solving diffusion dynamics for all species; scaffold, water and growth factor. We also create both 2D and 3D geometries used in the models in COMSOL software.

CHAPTER 3

3. MATERIALS AND METHODS

As a branch of tissue engineering, bone tissue engineering seeks ways to enhance the regeneration of bone mass lost due to physiological disorders like tumors, osteoporosis which frequently prevails among elderly women or particularly in larger bone defects like externally caused bone fractures (Sanz-Herrera et al., 2009). Bone has an inherent capacity to regenerate and heal small wounds and cracks. Nevertheless, for fractures exceeding a threshold (typically > 2cm) usually require external treatment depending on the anatomical location (Meyer et al., 2009; Tajvar et al., 2023). Synthetic scaffolds are valuable alternatives as a treatment alternative for critical bone defects, with numerous preclinical studies demonstrating successful outcomes (Bazyar & Sheidaee, 2024; De Witte et al., 2018).

3.1.Properties and Requirements of Bone Scaffolds

A bone scaffold should replace the injured bone site for the healing process promoting bone growth and disappear completely at the end of the healing (Liebschner & Wettergreen, 2003). Bone scaffolds should satisfy desired physical and chemical properties in both macro and micro scales and be able to mimic extracellular matrix (ECM), in terms of both mechanically and biologically during the healing process (Tajvar et al., 2023). The mechanical strength of the scaffold should match the actual bone in the defect site; however, they should have adequate interconnected voids inside for new tissue formation and vascularization. Bone scaffolds ought to be porous structures to meet the mass transport, cell nutrition, cell migration and cell attachment requirements (Hollister, 2005).

Biocompatibility of the scaffold material is a crucial point. Biocompatibility is the capacity to support tissue regeneration without causing any toxic effects on the body and inflammatory response (Hussein et al., 2016; D. Yang et al., 2019). Thus, biocompatibility is an essential requirement for scaffold materials. On the other hand, bioactivity is the ability of a material to react with host tissue in a manner that their reaction increases biological activity, such as cellular regulatory events (dos Santos et al., 2017). Bioactive materials are available to form chemical bonds with the tissue and ease the interstitial integration of them, which eventually boosts the healing process at the defect site (Oyane et al., 2003). Unlike biocompatibility, bioactivity is not a necessity for bone tissue implants. Although numerous synthetic polymers are currently used as bone scaffolds because of their mechanical properties and degradation dynamics, they often need surface modification for biological activity which makes the topic an active research area (Bakhshayesh et al., 2018). For example, even though PLA and PCL are highly preferred biodegradable and biocompatible synthetic polymers in bone scaffolds, their hydrophobic nature does not allow using their pure forms, because they lack in bioactive sites for the cell adhesion (Li et al., 2019). To enhance cellular attachment onto scaffold, its surface can be chemically modified by adding cell adhesion molecules. Surface modifications also increase the biocompatibility of the material (Meyer et al., 2009). Optimal surface modifications can enhance osseointegration even in inferior quality implant insertion circumstances which frequently results in lack of primary stability of the scaffold (Verardi et al., 2018). As a surface property, hydrophilicity and hydrophobicity have a role in cell attachment to scaffold. Studies show that cell capability to attach the scaffold is higher in hydrophilic surfaces and hydrophilicity is an effective parameter on cellular activities (Suamte et al., 2023).

Scaffolds need to possess adequate mechanical properties, such as tensile strength, elastic modulus, and stiffness (Table 1). These properties ensure that scaffolds have sufficient strength and stiffness for surgical handling and can maintain functionality from implantation until complete degradation. Once transplanted into an animal or human body, scaffolds are subjected to various loads, including compression, tension, shear, torsion, bending, and biomechanical/physiological forces. Compression is the most common load experienced in vivo. If scaffolds lack adequate stiffness to withstand these loads, they may quickly lose their integrity and functionality. Additionally, the healing rate of bone tissue varies with age, which is a crucial factor to consider when developing scaffolds for orthopedic applications. Therefore, considering the mechanical properties and behavior of scaffolds is essential in scaffold design (Suamte et al., 2023; S. Zhang et al., 2019a). The degradation rate of the scaffold and its diffusivity are crucial parameters for sustaining necessary mechanical strength over the course of time. The degradation rate should match the rate of tissue regeneration in that aspect. In a case where the degradation of scaffold is too slow compared to bone formation rate, scaffold cannot provide the space needed to form new tissue. This leads to problems in scaffold proper integration to defect site and transferring function from scaffold to tissue (Hollister, 2005; Tajvar et al., 2023).

Table 1: Appropriate scaffold pore size, porosity, and elastic modulus for bone tissue applications (S. Zhang et al., 2019b)

Tissue type	**Pore size (µm)**	**Porosity (%)**	**Elastic modulus**
Cancellous bone	500–1000	50–90	0.01–0.5 GPa
Cortical bone	<500	3–12	3–30 GPa
Cartilage	400	80	0.7–15.3 MPa

Porosity and pore size are two critical parameters for polymer scaffolds. Studies show that 100–500 µm pore sizes provide sufficient room for bone cells to live, move, and multiply in three dimensions (Garzón-Alvarado et al., 2012). Furthermore, it has been demonstrated that dual-pore scaffolds, which have both micro and macro pores, improve the potential for bone tissue regeneration (Abbasi et al., 2020). Because the structure of scaffolds affects the surface-to-volume ratio, it has a significant impact on how quickly they degrade. According to Zhang et al. recent research has demonstrated the important influence of the surface-to-volume ratio on scaffold degradation, with larger ratios resulting in a faster breakdown (H. Zhang et al., 2014). Connected pores allow biological fluids to seep into the scaffold, encouraging the body's resorption and replacement. Additionally, they offer a sizable surface area for interactions with the surroundings (Tajvar et al., 2023; von Doernberg et al., 2006). The porous structure of scaffolds lowers the mechanical strength but provides interconnectivity for biological processes (Ferraz, 2024). Pores also serve as cavities for cell attachment and movement (Hollister et al., 2002; Suamte et al., 2023). Adachi et al., have reported that the new bone formation occurred earlier in spherical pore structure rather than the lattice like structure even though the final bone alignment to the loading direction was similar. They have explained that the faster bone formation is due to the initial concave scaffold surface (Adachi et al., 2006).

In this thesis, we chose to work on a 3D scaffold made of CaP, the main geometry and parameters were based on Sun et al.'s work (X. Sun et al., 2013). Since the bone scaffold was modeled as surrounded by an extracellular matrix represented by water, hydrolysis is the main degradation mechanism for the polymer scaffold as well as the most considered one in literature. For example, from earlier works considered in the literature, Adachi et al. and Sanz Herrera et al. considered polymer scaffold degradation to occur via hydrolysis, modeling its rate using a linear relationship with local water content around the scaffold (Adachi et al., 2006; Sanz-Herrera et al., 2009). Similarly, Wang et al. modeled the degradation of polymer scaffold based on a nonlinear relationship between its rate and number of fluid elements around a scaffold element, among other parameters (L. Wang et al., 2020). We considered a second order chemical reaction rate expression to represent the hydrolysis reaction depending on both water and polymer presence at the same time.

3.2.Drug Release from Porous Scaffolds

Drug release studies aim to deliver minimum or optimal dosage of drug by tailoring its release kinetics. To study release kinetics, mathematical modeling is found to be a suitable approach (Arifin et al., 2006; Siepmann & Gopferich, 2001; L. Wang et al., 2020). The goal of mathematical drug release modeling is to forecast the mechanisms behind the drug diffusion, and kinetics affecting the release from delivery systems. By comparing experimental data with mathematical methodologies, these mathematical models can be used to improve release kinetics, identify the physical principles underlying drug transport, and determine the kinetics of release systems. Various mechanistic models, semi-empirical and empirical equations have been established for this purpose. Since the adaptability of mechanistic models to changing release systems, mechanistic models generally provide a better understanding of drug delivery. These models take biophysicochemical aspects into account which is critical for release modeling due to its complexity and sensitive nature to geometry, size, porosity of the delivery vehicles and drug properties themselves (Askarizadeh et al., 2023).

Empirical and semi-empirical models have been developed for estimation of drug release kinetics by many researchers due to their simplicity. They are developed by fitting a linear or nonlinear equation to an experimentally obtained drug release data. To do that, the percentage of released drug to the initially loaded total amount of drug is considered as a function of time (Mohseni-Motlagh et al., 2023). These types of release models include zero-order, first-order, and Higuchi model, Ritger-Peppas model (Rama & Vijayalakshmi, 2023). Zero-order release kinetics provides a linear relationship between initially loaded amount of drug and its time dependent changes depending on the zeroth order release constant such that $C(t)=C_0+k_0*t$. However, it is only applicable if the drug loaded area remains constant during the process. Due to its easy tunability, it has a potential to deal with the burst release problems which are mentioned earlier in the literature (Askarizadeh et al., 2023; X. Huang & Brazel, 2001). Assuming steady-state conditions, Fick's first law establishes a relationship between diffusive flux and concentration, with flux moving from high- to low- concentration locations in a manner proportional to the concentration gradient. The first-order release kinetics proposes a linear relationship with its release constant based on the first derivative of time dependent drug concentration. By contrast to zero-order kinetics, it can be applied to porous delivery vehicles or water-soluble matrices. Also, in cases where a drug is encapsulated into nano or microparticles to control and sustain their release for a specific time, the first-order kinetics are applicable. For example, Wang et al. have implemented a first-order release approach to their reaction-diffusion system where VEGF is released from a porous degradable bone scaffold (L. Wang et al., 2020).

Mechanistic drug release models have been attributed to solving diffusion event driven equations. Although empirical approaches do not consider the drug carrier’s geometry and material characteristics in the model, mechanistic models are discussed based on the carrier geometry (Mohseni-Motlagh et al., 2023). Drug release from non-degrading porous vehicles is controlled by pure diffusion mechanisms. Such release systems can be classified as monolithic (Figure 8a) and reservoir systems. Reservoir systems have a reservoir loaded with drugs which is surrounded by a barrier to control the release rate whereas monolithic systems do not consist of this barrier around the carrier device. By this definition, porous scaffolds as drug release agents can be expected to obey monolithic release system dynamics. The release from non-degrading scaffolds follows first order

Fickian diffusion in which the concentration is at its steady state (Farzan et al., 2023). When it comes to biodegradable delivery vehicles, the release mechanism is highly affected by the polymer fate which can undergo a swelling or an erosion depending on many factors (Figure 8b). Thus, the diffusion mechanism follows the second order Fickian diffusion which involves spatial changes in the species concentration. Also, desorption of the drug is effective while degradation mode and rate affects diffusion of drug which results in a very complex process. Siepmann and Gopferich stated that the most crucial phenomena to consider for biodegradable drug delivery systems are chemical reactions responsible for polymer erosion and diffusional mass transport (Siepmann & Gopferich, 2001). Theories considering both mass transport and chemical interactions offer greater details on the mechanisms governing drug release than the empirical models. These models obey Fick's laws and take the concept of diffusivity into account. The effects of diffusion on changing concentrations over time are predicted by Fick's second law (Askarizadeh et al., 2023).

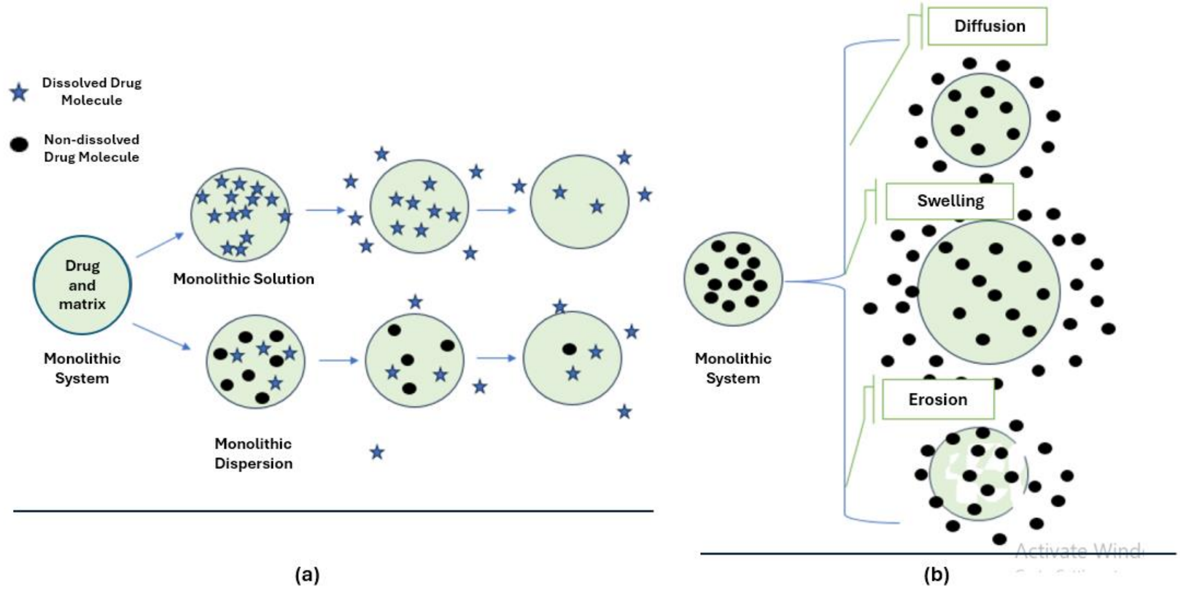

Figure 8: Controlled drug release mechanism for a monolithic system, (a) considering dispersion effect. (b) The release mechanism is determined according to polymer degradation fate, only diffusion is valid for drug transport in non-degrading polymer. In swelling or erosion of polymer, drug transport is affected by these mechanisms. Adapted from (Askarizadeh et al., 2023).

In this thesis, we chose to incorporate BMP-2 growth factor release from porous polymer scaffold adapted from Sun et al.'s work (X. Sun et al., 2013). Since our scaffold has a complex shape in 3D and the scaffold is eroding at the same time, a mechanistic model approach was necessary for the current model. In their work, they assumed an exogenous release from scaffold which indicates BMP-2 is assumed to be loaded externally to the scaffold. We also loaded BMP-2 to the interface of pores and scaffold. The time dependent dynamics of BMP-2 is modeled using a reaction-diffusion equation including its degradation, release and diffusion spatially and temporarily. Sun et al. took into account three growth factors including BMP-2, Wnt, and TGF-B to study the effect of different cytokine therapies on bone mass and endothelial cell number (X. Sun et al., 2013). However, we aimed to investigate the effect of polymer degradation and parameter dominance in the given geometry. The release term is in the form of Michaelis Menten (MM) approach, depending on the water concentration, initially loaded BMP-2 amount and Michaelis Menten constant. The concentration of water appears in both polymer degradation equation (Equation 3.4) and release equation (Equation 3.5) since it has a role in both occurrences. MM kinetics were employed for release by treating BMP-2 as a substrate and water as an enzyme; in a form of enzyme concentration is the dominant for the release. Similarly, Vmax in general MM approach is represented as the remaining concentration of BMP-2 in the scaffold by taking the difference between initial loading amount and BMP-2 concentration variable. Main assumptions were the neglect of affinity between BMP-2 and polymer scaffold during loading and release dynamics.

3.3.Construction of FEM Model

3.3.1. Background Validation of 2D Axisymmetric Geometry

Before the construction of a 3D porous geometry model presenting complexities both in terms of geometry, Boundary Conditions and the coupling of degradation and GF release mechanism, a validation study was performed using COMSOL Multiphysics (version 5.5) on a simple geometry for the degradation mechanism only. The validation study was adapted from Rothstein et al. which models spherical scaffolds in different sizes. The scaffolds were initially loaded with finite amount of drugs into the granules formed in the production of the scaffold. The granules were assumed to be distributed randomly throughout the matrix which provides a uniform distribution of drugs (Rothstein et al., 2009). As described in the literature, the hydrolysis reaction of the scaffold due to the diffusion of water-like extracellular fluids into the scaffold was assumed to result in the breaking of chemical bonds and dissolution (Von Burkersroda et al., 2002). The model equations for time-dependent water concentration within a hydrolysable polymer matrix of initial molecular weight were calculated from competing diffusion-reaction equations. As water diffuses into the matrix, a process described by Fick's second law, the scaffold degrades mainly via hydrolysis of the polymer matrix (Equations 3.1 and 3.2).

$$\frac{\partial C_W}{\partial t} = \nabla(D_W \nabla C_W) - kC_W M_W \tag{3.1}$$

$$\frac{\partial M_W}{\partial t} = -kC_W M_W \tag{3.2}$$

Here, C_W and M_W represent the concentration of water and the molecular weight of the polymer, respectively, D_W is the diffusivity of water within the polymer scaffold, and k is the polymer degradation rate constant. The literature states that the value of D_W is in the order of 10^{-12} m^2/s for various systems (Von Burkersroda et al., 2002).Wherever the gradient of the polymer molecular weight (dM_W/dr vs. r) is at its smallest in the polymer matrix, it may be said to represent a "degradation front". When the core of the polymer matrix is at its initial molecular weight, this minimum is defined as the inflection point of the continuous function, Mw(r), so that the initial average molecular weight at this front is ½ M_{wo} (Rothstein et al., 2009).

Various values collected from literature independent of geometry are also presented in Table 2 in more detail. The equation given in the third row of Table 2 is the standard Stokes Einstein equation which is used to estimate diffusion coefficients of spherical particles diffusing through a fluid. The general assumption is that the fluid particles are small enough for fluid to behave as a continuous phase. In the equation, k_B is the Boltzmann constant, T is the temperature, μ is dynamic viscosity and r is the radius of the considered particle. Manhas et al. used the equation to estimate diffusivity of $CaCl_2$ in water (Manhas et al., 2017). The equation in the last row is the Young-Carroad-Bell method employed by Huang et al. to estimate diffusion coefficients of BMP-4 and TGF-β (G. X. Huang et al., 2015). In the equation, T is the temperature, η is the dynamic viscosity of the fluid and M_i is the molecular weight of the protein.

Table 2: Examples for diffusivity of water and growth factor, degradation rate of polymer scaffold from literature

Parameter	**Value**	**Reference**
D_W	$4.6x10^{-15}$ m^2/s	(Adachi et al., 2006)
	$10x10^{-12}$ m^2/s	(Rothstein et al., 2009)
	$D=kBT6\pi\mu r=2.83x10^{-9}$ m^2/s	(Manhas et al., 2017))
k	$4.2x10^{-7}$ 1/s	(Adachi et al., 2006)
	$2.5x10^{-10}$ to $6.9x10^{8}$ 1/s	(Göpferich, 1996)
D_G	$2.9x10^{-10}$ m^2/s (in water, BMP-2)	(Davis & Leach, 2011)
	$5.2x10^{-11}$ m^2/s (in water, VEGF)	
	$4.6x10^{-14}$ m^2/s in PLGA	(Siepmann et al., 2005)
	$2x10^{-10}$ m^2/s (in water, VEGF)	(Mac Gabhann et al., 2005)
	$2.3x10^{-12}$ m^2/s BMP in hydrogel	(Ribeiro et al., 2015)
	$2.9x10^{-11}$ m^2/s (VEGF)	(L. Wang et al., 2020)
	$D=(8.3x10-8)*T/(\eta M_i^{1/3})$	(G. X. Huang et al., 2015)

The radius of the spherical scaffold in the model was set to 2 and 20 mm for two cases. The water pool surrounding the polymer matrix was modeled with varying thicknesses relative to the matrix radius. Geometry was created as a 2D axisymmetric quarter-sphere, using axisymmetric and symmetry boundary conditions (Figure 9).

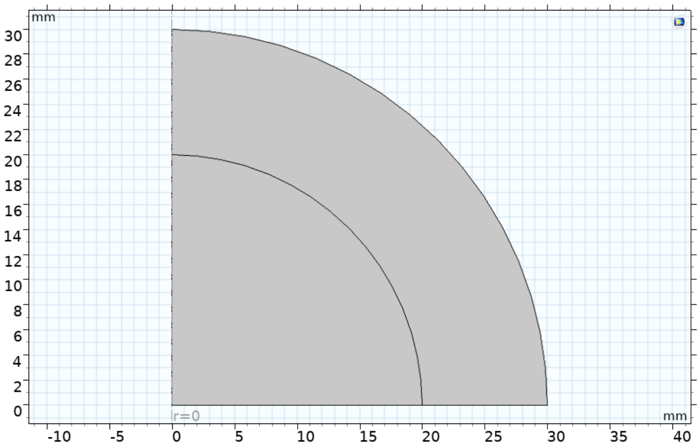

Figure 9: 2D axi-symmetrical geometry of drug loaded degradable matrix

The Chemistry interface under Chemical Species Transport in COMSOL Multiphysics was used for analyzing the chemical reaction and chemical components. In this module, the reaction kinetics and rate expressions were defined. The reaction was defined as a unidirectional reaction. The reaction rate constants, varying based on the amorphous and crystalline structure ratios of the polymer, were taken from the literature ranging from $8.75x10^{-9}$ 1/s to $2.7x10^{-7}$ 1/s (Gopferich & Langer, 1993). To separate the regions where the reaction occurs in the created geometry and model the diffusion of species after the reaction, the Transport of Diluted Species (TDS) module was added. Two separate TDS modules were used for the two distinct regions in the geometry: the matrix and the surrounding environment of water to mimic ECM. The TDS module was prepared for both regions using parameters given in the literature ranging DW from $1x10^{-13}$ to $1x10^{-11}$. In the model, the biodegradation reaction occurs only within the matrix, and the diffusion constants of the species within their respective regions were defined accordingly. Since exact values for the diffusion constants of water and species within the polymer matrix were not specified in the literature, different values ranging from 10^{-12} m^2/s to multiples of 10^{-14} m^2/s were used to run the model. The symmetrical conditions for the quarter-sphere geometry and the concentration boundary values at the intersections and endpoints of the regions were defined to create the spherical matrix. The concentration of water on the polymer matrix surface was calculated by dividing the initial water density by the molecular weight, as the hydrolysis reaction cannot start within the matrix when the water concentration is 0 as hydrolysis reaction is driven by water presence. Initially, the water concentration in the polymer matrix was set to 0 mol/m^3, and 1 mol/m^3 in the surrounding environment. The initial molecular weight of the polymer matrix was given as 10 kDa in the scaffold region, as specified in the literature (Rothstein et al., 2009). The simulation was solved for a time span of 12 months and for four different reaction rate constants, assuming a polymer matrix radius of 2 and 20 mm. The COMSOL model details and relevant settings are given in Appendix A.

3.3.2. Model Construction for Polymer Degradation and Growth Factor Release

The degradation of a 3D spherical porous bone scaffold due to hydrolysis and growth factor release from the degrading scaffold is modeled. The non-dimensional molecular weight of the polymer and water concentration is modeled using the partial differential equations given in Equations 3.3-3.5, that were solved simultaneously. These represent a diffusion-reaction system based on second order Fickian diffusion of extracellular liquid such as water and the standard second order reaction rate term for hydrolysis of polymer scaffold (Equations 3.3 and 3.4, respectively). Water was taken into account to represent the extracellular liquid surrounding the implanted bone scaffold.

$$\frac{\partial C}{\partial t} = \nabla(D_W \nabla C) - k_C C M \qquad (3.3)$$

$$\frac{\partial M}{\partial t} = -k_M C M \qquad (3.4)$$

where C is the water concentration and M is the polymer molecular weight, D_W is water diffusivity through the matrix, and k_C and k_M are degradation reaction rate constants for scaffold in water and matrix, respectively. At time zero, the water begins to penetrate the matrix, starting the hydrolysis reaction. Meanwhile, exogenous growth factor release starts from the degrading scaffold, and they continuously diffuse the extracellular liquid filling the pores. The presence of growth factor is modeled with another reaction-diffusion equation (Equation 3.5).

$$\frac{\partial G}{\partial t} = \nabla(D_G \nabla G) - \chi_{scaffold} r_{Gi} (G_{max} - G) \frac{C}{C + K_M} - d_G G \qquad (3.5)$$

where G is the concentration of growth factor, D_G is the growth factor diffusivity, which varies in scaffold and pore domains, r_G is the release constant, G_{max} is the initially loaded amount of growth factors to scaffold, K_M is the Michaelis constant, d_G is the degradation constant of growth factors. scaffold is a characteristic function which is equal to 1 in the scaffold domain and is equal to 0 otherwise. GF release from the scaffold to pores is employed by Sun et al. and modeled with Hill function according to the Michaelis-Menten kinetics. The remaining amount of growth factors in the scaffold are related to the water concentration such that it is stimulated by presence of water similar to a substrate behavior in the second term (X. Sun et al., 2013). Here we exclude porosity creation in the polymer matrix due to bulk erosion. The nondimensional molecular weight of the polymer decreases through time, but we assume that the bulk degradation will not increase porosity inside the scaffold, and not create a specified space for GF to diffuse. The diffusion coefficient of water within the scaffold was assumed to be less than one order of magnitude of that in pores. Similarly, growth factor diffusivity through the scaffold was three orders of magnitude less than that in pores.

Instead of solving the dynamical changes of concentration of 3 species using PDEs modules in COMSOL, the chemistry and transport of diluted species interfaces were coupled to model the three equations. The Chemistry interface involves two irreversible reactions that correspond to the hydrolysis reaction of the polymer matrix which depends on water concentration and the growth factor degradation reaction (Equations 3.6 and 3.7, respectively). Although the degradation of polymer occurs via hydrolysis, growth factors are not through hydrolysis; however, we assumed a first order degradation reaction for growth factor decay (X. Sun et al., 2013; L. Wang et al., 2020). Thus, the effect of water presence on growth factor concentration is only on its release kinetics indirectly by polymer degradation. The reaction rates of both equations employed the mass action kinetics (which described in Chapter 3.2 in detail). A quadratic discretization method was used in the Chemistry interface while a linear discretization is applied to the module in all domains.

$$M + W \rightarrow MW \tag{3.6}$$

$$G \rightarrow GW \tag{3.7}$$

The release term of GF is implemented as an additional term for species G in the COMSOL software, while transport of diluted species (TDS) interface was coupled with chemistry interface to solve diffusion of all three species. Therefore, Equation 3.4 and the last terms of the remaining equations are solved by the chemistry interface. The TDS module employs a second order Fickian diffusion by default which allows direct implementation of the first terms of Equations 3.3 and 3.5. Since degradation of scaffold occurs only in the scaffold domain, its reaction rate was not employed in the pore domain.

Moreover, the degradation rate constant of the growth factor is indicated in the Chemistry interface as the rate of Equation 3.7 similar to the rate constant, k, of Equation 3.6.

The characteristic function used in Equation 3.5 (scaffold) was applied to the model using an interpolation function. Since the remaining growth factor term should stand only for the scaffold domain, the solution was arranged to consider this term only in the scaffold domain. However, the chemistry interface does not allow defining domain-based reactions. To solve this issue, the coordinate data of each node belonging to scaffold and pore domains were obtained after an initial run. Then, an external interpolation file was prepared and coordinates corresponding to scaffold nodes assigned as 1 while pore coordinates were assigned as 0. The same approach was applied for the initial growth factor loading part. Since the GFs initially loaded only to the pore-matrix interface, the coordinate data for each node on the boundaries of the geometry was exported and externally manipulated to assign as 0.8 (the initial loading amount) nodes corresponding to pore-matrix interface while the remaining were assigned to be zero (Appendix B).

COMSOL Multiphysics® software (version 6.1) was used to develop the mathematical model describing polymer scaffold degradation and growth factor release from degrading scaffold as shown in Figure 10. A three-dimensional porous scaffold geometry was constructed using COMSOL geometry interface. It was designed as a cubic matrix with a size of 1.5mm x 1.5mm x 1.5mm and pore radius of 0.3 mm. The lateral pores are tangent to the surfaces of the scaffold on the y- and x-planes. The spherical pores are designed to have an intersection whose length corresponds to 10% of the diameter of the pores.

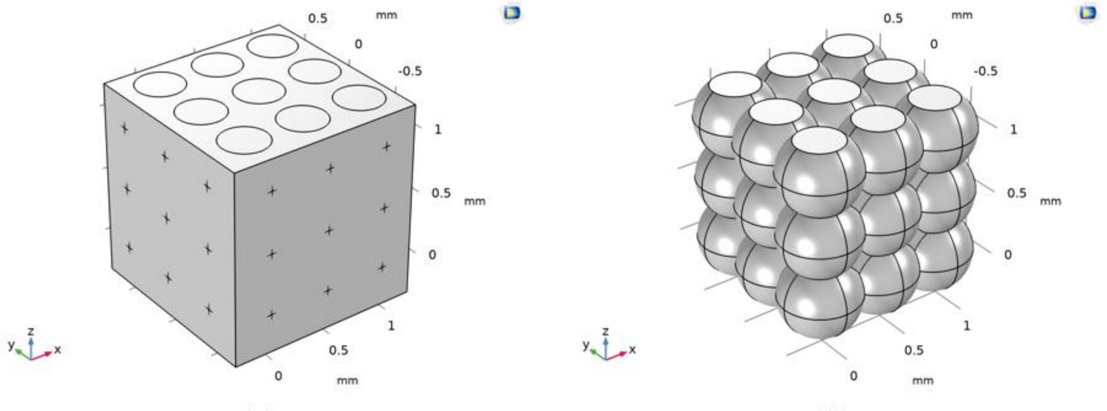

(a) (b)

Figure 10: a) 3D geometry of the cubic structure of the scaffold, and b) the spherical pores inside the cubic matrix.

The initial concentration of water is given as 1 in pores and 0 in matrix while the initial concentration of matrix is set as 0 in pores and 1 in matrix domain. The homogeneous Neumann boundary conditions are applied for all three equations, zero flux is applied along the outer boundaries of the geometry as shown in Figure 11. Growth factors were initially loaded to the interface of scaffold and pore domains to model the exogenous release. In vivo secretion of GF was ignored because its release from the scaffold is comparably higher than GF secretion of a cell (X. Sun et al., 2013; L. Wang et al., 2020).

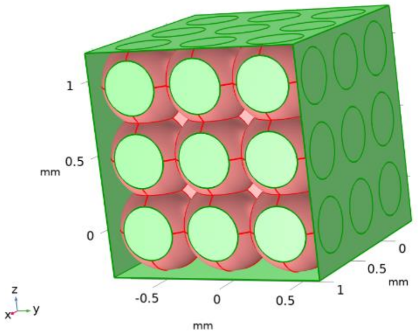

Figure 11: Scaffold surfaces with zero flux condition (green).

Since the three equations (Equations 3.3, 3.4, 3.5) are coupled in Chemistry and TDS interfaces, obtaining their solutions requires communication between these interfaces. This integration is essentially provided in two different ways. In the first, tds module asks the source of diffusions of each species and it was specified as ‘chemistry’ to link the diffusivities to the Chemistry interface (Appendix B). Because there are two transport properties that were set for scaffold and pore domains separately to distinguish the diffusion coefficients of species in different materials, the same is applied to the second transport properties section. The second relation between two interfaces was enabled by defining two separate reaction conditions in the TDS module for Equations 3.6 and 3.7. The rates of both reactions are called from the chemistry interface. While the first reaction was assigned for matrix domain only to solve for each species reaction, the latter was assigned for pore domain and reaction rate of Equation 3.6 was manually assigned as 0 since there is no polymer degradation event occurring in pores. All COMSOL model settings and details for the 3D model are provided in Appendix B.

The parameters necessary to solve these equations are given in Table 3. The parameters are based on the in-depth parametric study performed in this thesis to match to the extent possible the GF and polymer concentration profiles of the chosen reference study (X. Sun et al., 2013). The initial parameters chosen for the parametric study were selected based on literature and tuned with an insight gained in the course of the model study part. The fitted values are determined to be close to the literature values with some of them presented. The values provided can be compared to the ones Table 2 provided above. In the parameter fitting process, we initially focused on k and D_W in Equations 3.3 and 3.4, and our fine tuning was based on the resulting polymer concentration profile and distribution. Later, we concentrated on D_G, d_G, r_G in Equation 3.5 with a target of matching the GF concentration profiles.

Table 3: Important model parameters and their values used in the simulation studies of the thesis.

Parameter	**Value**	**Description**	**Reference**
k_M	4.00×10^{-7} 1/s	degradation rate of polymer	Fitted
k_C	4.00×10^{-7} 1/s	degradation rate of water	Fitted
D_W	4.6×10^{-8} mm²/s	diffusivity of water in matrix	Fitted
D_G	2.9×10^{-9} mm²/s	diffusivity of BMP2 in matrix	Fitted
r_G	2.0×10^{-5} 1/s	release constant for BMP2	Fitted
K_M	0.5	Michaelis Menten constant	(Sun et al., 2013) / Fitted
d_G	1.0×10^{-8} 1/s	degradation rate of BMP2	Fitted
M_G	26 kDa	molar mass of BMP2	(Sundermann et al., 2020)

The whole process is simulated for the real time length of 1 day and total period of 28 days with weekly time steps. A physics-controlled mesh was used with finer element size having 0.0825 mm maximum element size. Time-dependent direct solver was used with a fully coupled approach to solve for all unknowns simultaneously and to include the couplings between them at once. All direct solvers that COMSOL offers (MUMPS, PARDISO and SPOOLES) use LU decomposition, however PARDISO tends to be the fastest one (COMSOL, 2022). Thus, PARDISO was selected as the solution to avoid out-of-core memory error of MUMPS due to its need for more memory. The linear direct solver used the constant Newton method with a damping factor of 0.9 with maximum 8 number of iterations. An implicit BDF scheme was employed for time-stepping with initialization using backward Euler scheme.

3.4.Modeling of Biological Systems

The intricate nature of biological interactions in the growing field of systems biology demands the use of sophisticated computational models to supplement conventional experimental methods. Genes, proteins, and metabolites form complex networks within cells and tissues that dynamically interact to form biological systems (Kitano, 2002; Sobie, 2011). Although crucial for obtaining empirical data, experimental approaches frequently lack the capacity to fully capture the range of these interactions because of obstacles such as scale and one-by-one variable manipulation. This gap is filled by computational modeling, which makes it possible to combine different datasets, simulate biological processes, and forecast how a system will behave in different scenarios. These models have the capacity to capture the fundamental ideas of biological networks, offering insights that are frequently unattainable through experimentation alone. Moreover, computational methods make it easier to generate and evaluate hypotheses, enabling researchers to investigate possible outcomes and pinpoint important regulatory systems (Ideker et al., 2001; Kahlem & Birney, 2006). The information gathered from in silico simulations guides the design of experiments and facilitates an integrated strategy that hastens the identification of new therapeutic targets and the further development of precision medicine techniques (D. C. Clarke, 2000).

As a subgroup of network-based models, systems of ordinary and partial differential equation systems (ODEs and PDEs) are mostly employed to simulate the cellular components as dynamically changing variables. Despite using discrete pairing values 1 and 0 representing presence and absence of transcription factors, ODE systems evaluate concentrations of TFs as a continuous variable in time. ODE systems allow treating the independent variable of continuous time and the dependent variables of concentration of species as discrete steps according to model behavior (Klipp et al., 2016). These equation systems can be deterministic and stochastic. While stochastic modeling enables studying a system arising from fluctuations or noisy data, deterministic modeling ignores the stochastic effects and assumes that these signaling components are homogeneously distributed within the cell (Aldridge et al., 2006; Zi, 2012). Selecting the most appropriate method for a model depends on the properties of the system and main expectations from the model. ODE-based methods can be extended to study interaction reaction kinetics in three common ways: law of mass action, Michaelis-Menten kinetics and Hill function. Similarly, they can be simplified by applying well-studied laws such as quasi-steady state assumptions (Thakur et al., 2023; Zi, 2012).

The primary processes responsible for signal transmission in biological systems are protein-protein interactions, enzymatic reactions, including cycles of protein phosphorylation and dephosphorylation, protein degradation, and intracellular messenger proteins. These interactions are communication tools of cells or other components of the biological system. Because all these interactions can be represented as chemical reactions, the kinetic study is a viable method for dynamical analysis of both small- and large-scale signaling pathways. Establishing a connection diagram including the chemical reactions and giving the various interactions the right kinetic characteristics or rate laws is essential for kinetic studies (Anbumathi, 2014; Crampin et al., 2004). Determining the type of reaction intermediates, their interactions (how they react with or change into each other), and the rates of these transformations are the main objectives of a mechanistic analysis of a biological system.

The law of mass action, which was introduced in the nineteenth century, states that the probability of the collusion of reactants in a reaction is proportional to the rate of the reactions' rate. This probability is also proportional to the concentrations of each reactants' power of molecularity which indicates how many of them undergo the reaction (Klipp et al., 2016). A reaction involves two reactants, and one product is represented as

$$A + B \leftrightarrow P \tag{3.8}$$

The reaction rate for Equation 6 is written based on the law of mass action as

$$v_{net} = v_{forward} - v_{backward} = k_{forward} \cdot [A] \cdot [B] - k_{backward} \cdot [P] \tag{3.9}$$

where the v_{net} is the net reaction rate, $k_{forward}$ and $k_{backward}$ are the reaction rate constants for the forward and backward reactions, respectively, and bracket parentheses are used to represent the concentration of the species. Then, the generalized reaction rate equation can be written as

$$v_{net} = v_{forward} - v_{backward} \tag{3.10}$$

$$v_{net} = k_{forward} \sum_{i=1}^{mi} reactant_i - k_{backward} \sum_{j=1}^{mj} product_j \tag{3.11}$$

where m_i and m_j are the reactants and products of the reaction. To derive the ODEs evaluating the dynamics of the reaction can be then written based on the net rate as

$$\frac{-dA}{dt} = \frac{-dB}{dt} = \frac{dP}{dt} = v_{net} \tag{3.12}$$

The reason for equal coefficients between differential terms is due to the equal stoichiometry in the reactants and product in Equation 6, and the minus coefficient in the reactants is due to the consumption of them.

In a similar manner, a chemical conversion of a substrate S into a product P can occur spontaneously

$$S \overset{k}{\rightarrow} P \tag{3.13}$$

where k is the reaction rate constant that regulates the speed of the reaction. Enzymes are biological catalysts that are naturally found in the body. Enzyme involved reactions have a formation of an enzyme-substrate complex as an intermediate step. An enzymatic reaction is represented as

$$S + E \overset{k1,k-1}{\longleftrightarrow} C \overset{k}{\rightarrow} E + P \tag{3.14}$$

where C is the enzyme-substrate complex. Enzymes convert a simple one step elementary reaction to two elementary reactions dividing the reaction steps. The first step is a reversible interaction between enzyme and its substrate forming a complex, and the second step is the formation of product by irreversible dissociation of complex with a chemical alter only in substrate. Enzymes accelerate a chemical reaction by working similar to a catalyst by lowering the free energy barrier such that the production of P is generally faster in the second reaction than the first (Eilertsen et al., 2021). To apply mass action law to Equation 3.14 results with the following system of ODEs:

$$\frac{dS}{dt} = -k_1 \cdot E \cdot S + k_{-1} \cdot ES \tag{3.15a}$$

$$\frac{dES}{dt} = k_1 \cdot E \cdot S - (k_{-1} + k_2) \cdot ES \tag{3.15b}$$

$$\frac{dE}{dt} = -k_1 \cdot E \cdot S - (k_{-1} + k_2) \cdot ES \tag{3.15c}$$

$$\frac{dP}{dt} = k_2 \cdot ES \tag{3.15d}$$

This system of ODEs cannot be solved analytically (Klipp et al., 2016). This requires an application of numerical solution, or a simplification for the system of equations. Michaelis and Menten introduced a mathematical model based on a quasi-steady-state assumption (QSSA) for the complex. They claimed that ‘if the rate of production formation (k_1) is approximately constant over the time interval concerned', then the complex concentration would be approximately constant $\left(\frac{dC}{dt}=0\right)$ (Segel & Slemrod, 1989). However, this assumption is valid only if the enzyme concentration is small compared to that of the substrate. The validity of QSSA is limited to $E_0 \ll S_0$, but then it is more generalized to $E_0 \ll S_0 + K_M$ where $K_M = \frac{k_{-1}+k_2}{k_1}$ is the Michaelis Menten constant (H.-W. Kang et al., 2017).

The derivation of QSSA applied expression is applied to the current problem of the thesis in Chapter 3.2.1, so it is not introduced here. Shortly, the general Michaelis Menten kinetics is obtained as

$$v = \frac{V_{max} \cdot S}{K_M + S}, V_{max} = k_2 + E_{total} \tag{3.16}$$

where V_{max} is the maximum reaction velocity and E_{total} is the initial enzyme concentration (unbound). It is necessary to clearly distinguish the timescales of the fast and slow species—that is, the substrate and the enzyme–substrate complex in order to use the quasi-steady-state approximation in an efficient manner. Reducing the complexity of the system by using different timescales to simplify reaction kinetics is an important and often used method. Determining the proper time intervals and circumstances for this simplification to be true, especially for a process involving just one enzyme and substrate, has been a subject of discussion (Crampin et al., 2004).

Many reactions empirically show sigmoidal kinetics with respect to substrate concentration. The Hill equation is a mathematical equation that describes this sigmoidal behavior between the substrate concentration and the enzyme that is occupied by the substrate. By doing so, it quantifies responses that are either ultrasensitive or sub-sensitive to changes in allosteric proteins. In order to mathematically characterize this binding for enzyme-substrate processes, the empirical equation derived as

$$v = \frac{V_{max} \cdot S^n}{K_M + S^n} \tag{3.17}$$

where n is the Hill coefficient (Anbumathi, 2014; Crampin et al., 2004). The general form of the Hill equation is given as by Klipp et al. by assuming the complete cooperativity in binding of protein-ligand (Klipp et al., 2016).

$$v = \frac{V_{max} \cdot K_B \cdot S^n}{1 + K_B \cdot S^n} \tag{3.18}$$

where K_B is the binding coefficient of protein-ligand. N indicates the degree of cooperativity, for n being 1 means the binding of a ligand does not affect the binding of others. For n values larger than 1, there is a positive cooperativity meaning that binding of a ligand increases the affinity for others.

After that, these complexes are either absorbed or take part in phosphorylation processes. Through a sequence of events involving ATP and other active components, signaling components are phosphorylated. Anyone signaling component has the ability to activate several other signaling components; this kind of multi-functionality, such as crosstalk, is frequently observed in biological systems. Finally, the downstream effector molecules that arise from the signaling pathways are active transcription factors, which are indicative of phosphorylated proteins (Min Lee et al., 2008).

Many of the individual key reactions within this complex signaling network are not amenable to experimental investigation, making it impossible to ascertain experimentally whether such a hypothesis is consistent with the observed kinetics of nuclear accumulation of activated Smad complexes and their behavior after receptor inactivation. Furthermore, identifying the reactions that are rate-limiting and, therefore, possible targets for therapeutic intervention, is challenging (Schmierer et al., 2008).

In this thesis we analyze the dynamical changes in transcription factors affected by BMP-2 concentration by representing their signaling pathway as a chemical reaction system. Mass action law is applied to obtain a system of ODEs similar to given in Equation 3.15. Also, Michaelis Menten approach is applied under steady state approximation for enzyme-substrate complex and Hill function is employed to make the transcription factor behavior more sensitive to BMP-2 concentration similar to Equation 3.17.

3.4.1. Application of Michaelis Menten and Hill Function to The Current Problem

The signaling pathway system is limited to 4 major components, BMP-2, Smad1/5, Runx2 and Osx (Figure 12). Osx is downstream of both Smad1/5 and Runx2, so their effect on Osx phosphorylation is considered separately. The mathematical model consisting of their dynamical changes is a system of 4 nonlinear ODEs with 12 kinetic parameters arising from chemical reactions by mass action kinetics. Equation 16 is the chemical reaction set representing the cellular signaling events taking place.

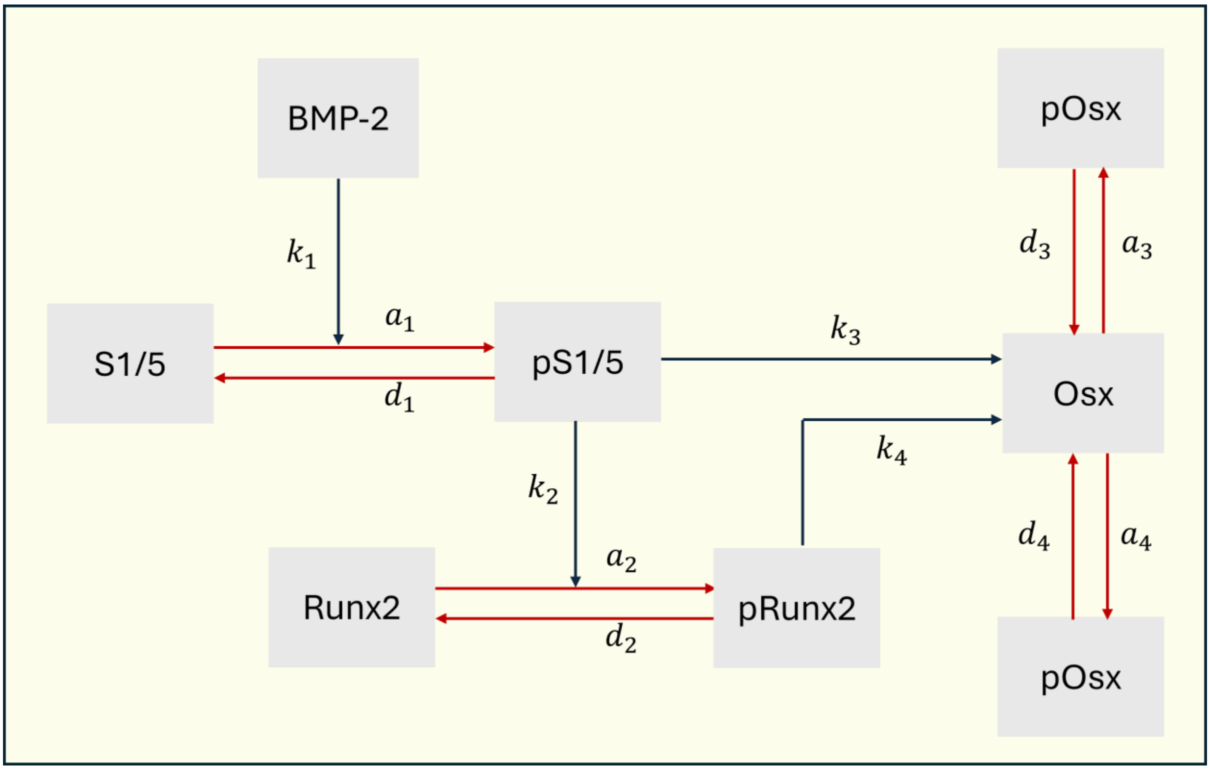

Figure 12: BMP-2-Smad signaling pathway considered in the model. The red lines indicate activation and deactivation of TFs and blue lines are the product formation from intermediate complex.

$$S1 + BMP2 \overset{a1,d1}{\longleftrightarrow} S1: BMP2 \overset{k1}{\rightarrow} pS1 + BMP2 \tag{3.19a}$$

$$pS1 + Runx2 \overset{a2,d2}{\longleftrightarrow} pS1: Runx2 \overset{k2}{\rightarrow} pS1 + pRunx2 \tag{3.19b}$$

$$pRunx2 + Osx \overset{a3,d3}{\longleftrightarrow} pRunx2: Osx \overset{k3}{\rightarrow} pRunx2 + pOsx \tag{3.19c}$$

$$pS1 + Osx \overset{a4,d4}{\longleftrightarrow} pS1: pOsc \overset{k4}{\rightarrow} pS1 + pOsx \tag{3.19d}$$

where a_i, d_i, are the reaction rate constants for the reversible enzyme-substrate binding (association and dissociation rate constants) and k_i is the rate of product formation reaction. According to Eilertsen et al.'s studies, the enzymatic reactions near the thermodynamic limit are modeled by nonlinear ordinary action (Eilertsen et al., 2021). Moreover, if the concentrations of the species in the reaction system is not too low, the system again can be represented by nonlinear ODEs based on mass action law, under the assumption of well-mixed conditions (Eilertsen & Schnell, 2020). Dynamical changes in each species of a chemical reaction system can be expressed by rate equations for each species. The rate equations obey the law of mass action and form a system of nonlinear ODEs. At this point, considering enzyme-substrate kinetics, it is assumed that there are no chemical structure changes during the reactions. Furthermore, the association, dissociation and product formation rate constants are assumed to be independent of time and concentration. The bracket notation [] refers to concentrations of each species. Rename concentrations of each species for the sake of simplicity as following:

$$[S1] = x_1, [BMP2] = x_2, [pS1] = x_3, [S1{:}BMP2] = y_1, [Runx2] = x_4, [pRunx2] = x_5, [pS1{:}Runx2] = y_2, [Osx] = x_6, [pOsx] = x_7, [pRunx2{:}Osx] = y_3, [pS1{:}Osx] = y_4$$

Then, the nonlinear ODE system representing the time dependent changes of variables (concentrations of phosphorylated transcription factors) in Equation 3.19 are given in Equation 3.20.

$$\frac{dx_1}{dt} = -a_1x_1x_2 + d_1y_1 \tag{3.20a}$$

$$\frac{dx_2}{dt} = -a_1x_1x_2 + d_1y_1 + k_1y_1 \tag{3.20b}$$

$$\frac{dy_1}{dt} = a_1x_1x_2 - d_1y_1 - k_1y_1 \tag{3.20c}$$

$$\frac{dx_3}{dt} = -a_2x_3x_4 + d_2y_2 + k_1y_1 - a_4x_3x_6 + d_4y_4 + k_2y_2 + k_4y_4 \tag{3.20d}$$

$$\frac{dx_4}{dt} = -a_2x_3x_4 + d_2y_2 \tag{3.20e}$$

$$\frac{dy_2}{dt} = a_2x_3x_4 - d_2y_2 - k_2y_2 \tag{3.20f}$$

$$\frac{dx_5}{dt} = -a_3x_5x_6 + d_3y_3 + k_2y_2 + k_3y_3 \tag{3.20g}$$

$$\frac{dx_6}{dt} = -a_3x_5x_6 + d_3y_3 - a_4x_3x_6 + d_4y_4 \tag{3.20h}$$

$$\frac{dy_3}{dt} = a_3x_5x_6 - d_3y_3 - k_3y_3 \tag{3.20i}$$

$$\frac{dx_7}{dt} = k_3y_3 + k_4y_4 \tag{3.20j}$$

$$\frac{dy_4}{dt} = a_4x_3x_6 - k_4y_4 - d_4y_4 \tag{3.20k}$$

For a closed system, the conservation of mass law can be applied for enzymes to reduce the complexity of the equations since they come out of the reaction with no change in mass and composition. In the beginning, any phosphorylated component or complex is not formed yet, so we can write following initial conditions:

$$x_3(t = 0) = 0, \qquad x_1(t = 0) = [TotalS1] \tag{3.21a}$$

$$x_5(t = 0) = 0, \quad x_4(t = 0) = [TotalRunx2] \tag{3.21b}$$

$$x_7(t = 0) = 0, \quad x_6(t = 0) = [TotalOsx] \tag{3.21c}$$

$$y_1 = y_2 = y_3 = y_4 = 0 \; at \; t = 0 \tag{3.21d}$$

For the first reaction (Eqn. 3.19a), BMP-2 forms a complex with Smad1/5 reversibly, the concentration of total BMP-2 is the sum of concentrations of the intermediate complex and its concentration at any time for enzyme conservation (Equation 3.22).

$$x_{2,T} = x_2(t) + y_1 \tag{3.22}$$

The same implication that eliminates Equation 3.20b can be mathematically shown by adding up Equations 3.20b and 3.20c and using the initial condition $y_1 = 0$;

$$\frac{dx_2}{dt} + \frac{dy_1}{dt} = 0 \tag{3.23}$$

Based on the conservation of mass, we know that the sum of phosphorylated and unphosphorylated concentrations of transcription factors are equal to their initial concentrations at any time so we can write Equation 3.24. Time dependency of concentration changes is dropped for the sake of simplicity:

$$x_{1,T} = x_1 + x_3 \tag{3.24a}$$

$$x_{4,T} = x_4 + x_5 \tag{3.24b}$$

$$x_{6,T} = x_6 + x_7 \tag{3.24c}$$

Equations 3.22 and 3.23 eliminate Equation 3.20b from the initial ODE system. Furthermore, we can substitute Equation 3.22 to all equations consisting of variable y_1. After that, Equation 24 eliminates three more equations from the initial system: Equations 3.20a, 3.20e and 3.20h since the total concentrations of transcription factors are constant. Then, the ODE system becomes Equation 3.25 as follows

$$\frac{dy_1}{dt} = a_1 x_1 (x_{2,T} - y_1) - d_1 y_1 - k_1 y_1 \tag{3.25a}$$

$$\frac{dx_3}{dt} = -a_2 x_3 x_4 + d_2 y_2 + k_1 y_1 - a_4 x_3 x_6 + d_4 y_4 + k_2 y_2 + k_4 y_4 \tag{3.25b}$$

$$\frac{dy_2}{dt} = a_2 x_3 x_4 - d_2 y_2 - k_2 y_2 \tag{3.25c}$$

$$\frac{dx_5}{dt} = -a_3 x_5 x_6 + d_3 y_3 + k_2 y_2 + k_3 y_3 \tag{3.25d}$$

$$\frac{dy_3}{dt} = a_3 x_5 x_6 - d_3 y_3 - k_3 y_3 \tag{3.25e}$$

$$\frac{dx_7}{dt} = k_3 y_3 + k_4 y_4 \tag{3.25f}$$

$$\frac{dy_4}{dt} = a_4 x_3 x_6 - k_4 y_4 - d_4 y_4 \tag{3.25e}$$

Calling standard quasi-steady-state-approximation (sQSSA) for complex formation here is necessary to proceed further analytically. sQSSA assumes the complex concentration remains constant if the measured reaction rate of product formation is approximately constant over the time interval concerned (Segel & Slemrod, 1989). This implies that concentration of complex is not changing with time, then it is said that $d\,[Complex]/dt = 0$. For our case, sQSSA simplifies Equations 3.25a, 3.25c, 3.25e and 3.25e to simple algebraic equations. Substituting the algebraic forms of the four equations to the remaining ones, the system is left with three ODEs representing the concentration changes of phosphorylated transcription factors given in Equation 3.26:

$$\frac{dx_3}{dt} = \frac{x_1 x_{2,T} k_1}{x_1 + \frac{d_1 + k_1}{a_1}} \tag{3.26a}$$

$$\frac{dx_5}{dt} = \frac{x_3 x_4 k_2}{\frac{d_2 + k_2}{a_2}} \tag{3.26b}$$

$$\frac{dx_7}{dt} = \frac{x_5 x_6 k_3}{\frac{d_3 + k_3}{a_3}} + \frac{x_3 x_6 k_4}{\frac{d_4 + k_4}{a_4}} \tag{3.26c}$$

Michaelis constant is defined as $K_M = \frac{d_i + k_i}{a_i}$ and the maximum velocity of an enzymatic reaction that can be reached is $V_{max} = k_i x_{i,T}$. Considering the effect of decay rate for each transcription factor can be added as an additional rate term to each ODE in an elementary reaction form (rate constant times concentration of degrading species). Re-writing Equation 3.27 in the form of K_m and V_{max} considering degradation of each transcription factor results the following set of equations:

$$\frac{d[pS1]}{dt} = \frac{V_{max,1} \cdot [BMP2]}{K_{M,1} + [S1]} - d_1 \cdot [pS1] \tag{3.27a}$$

$$\frac{d[pRunx2]}{dt} = \frac{V_{max,2} \cdot [Runx2]}{K_{M,2} + [Runx2]} - d_2 \cdot [pRunx2] \tag{3.27b}$$

$$\frac{d[pOsx]}{dt} = \frac{V_{max,3} \cdot [Osx]}{K_{M,3} + [Osx]} + \frac{V_{4,max} \cdot [Osx]}{K_{M4} + [Osx]} - d_3 \cdot [pOsx] \tag{3.27c}$$

where d_i is the degradation constant for each protein. The derived equations (Equation 3.27) are a representation of a standard Michaelis Menten approach to enzyme-substrate dynamics based on a tailored Hill function. The Hill function can be scaled to tune the non-linear responses in a biological system (Ang et al., 2013). BMP-2 behaves as the activator of transcription factors such that it phosphorylates Smad1/5 and then Smad1/5 activates both Runx2 and Osx. The output signal of transcription factors here is modeled as the concentration of the enzyme is more dominant in phosphorylation of the substrates rather than the substrate concentration. Thus, Equation 3.27 can be tuned to have enzyme concentrations in both numerator and denominator of the Michaelis Menten terms whereas the degradation of each TF still obeys first order chemical reaction (Equation 3.28) (X. Sun et al., 2013).

$$\frac{d[pS1]}{dt} = \frac{V_{max,1} \cdot [BMP2]}{K_{M,1} + [BMP2]}([TotalS1] - [pS1]) - d_1 \cdot [pS1] \qquad (3.28a)$$

$$\frac{d[pRunx2]}{dt} = \frac{V_{max,2} \cdot [pS1]}{K_{M,2} + [pS1]} - d_2 \cdot [pRunx2] \qquad (3.28a)$$

$$\frac{d[pOsx]}{dt} = \frac{V_{max,3} \cdot [pS1]}{K_{M,3} + [pS1]} - \frac{V_{max,4} \cdot [pRunx2]}{K_{M,4} + [pRunx2]} - d_3 \cdot [pOsx] \qquad (3.28a)$$

Equation 3.28 is the final system of ODEs representing the dynamics of considered BMP-2/Smad1/5 signaling pathway to regulate gene expression which cannot be solved analytically. At this point, another quasi-steady-state assumption can be applied for further simplification. Since the growth factor release is much slower than the intracellular signaling pathway reactions, it can be assumed that the changes in growth factor concentration affects the ODE system as a discrete input. This assumption is valid since the BMP-2 concentration in Equation 3.28a is evaluated from its release from degrading scaffold for 28-day period. However, reaching a steady state for intracellular reactions takes far less time such that it occurs in minutes or hours (Chung et al., 2007; X. Sun et al., 2013). Thus, by applying a QSSA to Equation 3.28, the ODE system can be reduced to a system of algebraic equations given in Equation 3.29.

$$[pS1] = \frac{[TotalS1]}{\left(1 + \frac{d_1 \cdot \left(K_{M,1} + [BMP2]\right)}{V_{max,1} \cdot [BMP2]}\right)} \qquad (3.29a)$$

$$[pRunx2] = \frac{1}{d_2} \cdot \left(\frac{V_{max,2} \cdot [S1]}{K_{M,2} + [S1]}\right) \qquad (3.29b)$$

$$[pOsx] = \frac{1}{d_3} \cdot \left(\frac{V_{max,3} \cdot [pS1]}{K_{M,3} + [pS1]} + \frac{V_{max,4} \cdot [pRunx2]}{K_{M,4} + [pRunx2]}\right) \qquad (3.29c)$$

The constants used in the model are borrowed from the reference study and provided in Table 4 below (X. Sun et al., 2013). Hence, the model used in this thesis relies on Michaelis Menten approach with Hill function. Also, a quasi-steady state assumption for phosphorylated transcription factor dynamics is solved using the final equations provided in Equation 3.29 via a code in MATLAB.

Table 4: Parameters used in intracellular signaling pathway

$V_{max,1}$	1.9608	nM/hr	maximal activation velocities of Smad1/5 by BMP2
$K_{m,1}$	33.7255	nM	Michaelis activation coefficient of Smad1/5 by BMP2
d_1	1	hr^{-1}	decay rate of phosphorylated Smad1/5
$V_{max,2}$	0.8198	nM/hr	maximal activation velocities of Runx2 by Smad1/5
$K_{m,2}$	93.451	nM	Michaelis activation coefficient of Runx2 by Smad1/5
d_2	36.8634	hr^{-1}	degradation rate of Runx2
$V_{max,3}$	0.0519	nM/hr	maximal activation velocities of Osx by Smad1/5
$K_{m,3}$	984.3137	nM	Michaelis activation coefficient of Osx by Smad1/5
$V_{max,4}$	0.0392	nM/hr	maximal activation velocities of Osx by Runx2
$K_{m,4}$	139.2157	nM	Michaelis activation coefficient of Osx by Runx2
d_4	0.0224	hr^{-1}	degradation rate of Osx

3.4.2. Model Development Details of BMP2-Smad Signaling Pathway

The derivation of standard Michaelis Menten approach is provided in the previous chapter. The final equation system was Equation 3.27. Then, Hill function was employed based on reference study to analyze the effect of enzyme concentration more efficiently (X. Sun et al., 2013). The output signal of transcription factors is modeled by focusing on the concentration of the enzyme, which is more influential in the phosphorylation of substrates than the substrate concentration itself. Therefore, Equation 3.27 is adjusted to use enzyme concentrations in both the numerator and denominator of the Hill functions. Meanwhile, the degradation of each transcription factor continues to follow a first-order chemical reaction, as described in Equation 3.28.

The final equation system for signaling pathway (Equation 3.29) is solved for a shorter time scale (in hours) using MATLAB software. The GF concentration obtained from the developed model in COMSOL is used as the input of this ODE system. The occurrence time period of the GF release is very different compared to signaling events such that GF release takes almost a month to reach a certain constant value in scaffold pores. On the other hand, the time it takes for transcription factors to be phosphorylated and reach a steady state value is reported in the order of minutes. Even though this variation in time scales makes it hard to analyze experimentally obtained kinetic data, it allows us to apply a quasi-steady-state assumption to simplify the system of ODEs. After QSSA, a nonlinear algebraic set of equations was obtained as shown in Equation 3.29. The very detailed derivation of Equation 3.29 was not provided here since it is a straightforward procedure. Shortly, assuming a steady state condition for each variable one by one as shown in Equation 3.30-3.32

$$d\,[pS1]/dt = 0 \tag{3.30}$$

$$d\,[pRunx2]/dt = 0 \tag{3.31}$$

$$d\,[pOsx]/dt = 0 \tag{3.32}$$

Equation 3.29 is obtained. Although the system is highly nonlinear, since it is in its current form an algebraic set of equations, it is easy to implement and solve this system in MATLAB (R2021b).

The Equation 3.29 which is the set of nonlinear algebraic equations requires the total Smad1/5 data. Considering that signaling events considered in this study takes place in cytoplasm, specifically total Smad 1/5 data is necessary. A singular total Smad1/5 concentration data is not available in literature; however, studies that cite cellular Smad4 concentrations (Inman et al., 2002; Schmierer et al., 2008). Also, similar data is available for nuclear concentrations of Smad2, Smad3 and Smad4 (D. C. Clarke et al., 2006; A. Sun, 2014). Although nuclear and cytoplasmic concentrations of transcription factors differ, total Smad1/5 concentration in the cytoplasm was calculated from Smad4 literature data based on the observation that there are no significant differences between Smad2, Smad3 and Smad4 concentrations in cytoplasm. In his study, Sun et al. employed Smad4 concentration as 5.61×10^{-8} mol/L for cell volume of 2.8×10^{-9} L (A. Sun, 2014). On the other hand, Clarke et al. used 1.2×10^{5} Smad4 molecules per cell (D. C. Clarke et al., 2006). To convert it to concentration units employed in the model (nM), the number of molecules is divided by Avogadro's number. In terms of nM, the difference between values is higher than an order of magnitude difference between the two literature values (Clarke et al suggested as 1993 nM yet A. Sun's was calculated as 56.1 nM) (D. C. Clarke et al., 2006; A. Sun, 2014). Since our reference study did not provide such information, we decided total Smad1/5 value considering literature. These abovementioned studies provide more detailed information including the GF concentration. In the meantime, the literature did not consist in terms of total Smad1/5 concentration. Thus, we have used a value that we obtained by tuning the intercepts of the system of algebraic equations to the reference study results of the literature data to find our total Smad1/5. Thus, we used 5200 nM for total Smad 1/5 concentration.

The calculated BMP-2 concentration based on the numerical solution of the PDE equations given in Equation 3.5 is used as input to Equations 3.29 as described. The calculated results obtained from the simulation model in COMSOL software refer essentially to time dependent dynamics of BMP-2 released from degrading 3D scaffold per the PDE Equation 3.5. However, after the QSSA application, the BMP-2 concentration must be supplied to the system of algebraic equations as time independent discrete values. The reference study did not specify the detail which time step they have used explicitly. We have assumed here that the BMP-2 concentration in the pore domain reaches a necessary level to activate the Smad1/5 in 21-days starting from the simulation events. Thus, we run the COMSOL simulation model constructing two consecutive study steps where the first simulates GF release on a weekly basis until the 21st day. The results of the first study are assigned as the initial values of the second study which refers to time steps of 2 hours for the following 50 hours. The second study results are exported, and these were taken as the inputs of the intracellular pathway equations.

3.5.Optimization

In this section, details regarding the optimization design study based on the integrated simulation model are described. Optimizing the concentrations of polymers and growth factors is crucial for enhancing the efficiency and effectiveness of biomedical applications, such as controlled drug delivery and tissue engineering. This part summarizes the implementation of the optimization study that was solved using MATLAB's well-known gradient based optimization solver, namely 'fmincon' function to conduct a multivariable design problem for the selected five design parameters of the integrated reaction-diffusion-GF release model after conducting an in-depth parametric analysis of the 3D scaffold in COMSOL Multiphysics software. The goal is to achieve optimal concentrations of both polymer and GF based on the given concentration and point coordinate data of the reference study as given in Table 5 (X. Sun et al., 2013). Optimizing both metrics at the same time can be achieved with a multi-objective multi-constraint optimization model. To solve a multi-objective optimization model using built-in fmincon function is not directly applicable, but instead a weighted sum approach can be adapted with pre-selected weights of polymer and growth factor concentrations targets. In order to avoid an iterative process to determine weights, we constructed and solved two separate and sequential optimization models for each objective target of concentrations.

Table 5: Reference study values for polymer concentration M, growth factor concentrations at pore and scaffold domains, Gp and Gs, respectively, over time (X. Sun et al., 2013).

Day	M	Gp	Gs
0	1	0	0
7	0.8	0.5	0.9
14	0.7	0.7	0.9
21	0.5	0.8	1
28	0.3	0.7	1

In these two optimization models, the construction logic was similar, and chosen design variables and objective value were assigned either to the polymer or GF concentration values. The main goal of the optimization models was to minimize the objective function which is defined as the sum of squared errors of desired concentrations of polymer and growth factor over respective time intervals, respectively. The minimization of objective functions is performed subject to only lower and upper bounds of design variables. The objective functions were defined as:

$$\text{Objective\_function\_1} = \sum ((PC7 - 0.8)^2 + (PC14 - 0.7)^2 + (PC21 - 0.6)^2 + (PC28 - 0.4)^2) \quad (3.33)$$

$$\text{Objective\_function\_2} = \sum((Gs7 - 0.9)^2 + (Gs14 - 0.9)^2 + (Gs21 - 1)^2 + (Gs28 - 1)^2 + (Gp7 - 0.5)^2 + (Gp14 - 0.7)^2 + (Gp21 - 0.8)^2 + (Gp28 - 0.7)^2) \quad (3.34)$$

where PCi refers to polymer concentration at the ith time steps in weeks within the simulation, and Gsi refers to the growth factor concentration in the scaffold at the ith week and Gpi is the growth factor concentration in the ith week within the pores.

The design variables for the first optimization model for PC are chosen based on the important PDE variables that affect the concentration profiles as:

- Diffusivity of water (D_W)
- Hydrolysis reaction rate constant (k)

The optimization is subject to the following constraints:

- Lower and upper bounds for each decision variable. In the performed optimization study, these limits are chosen as: (0.1, 100) m^2/s for D_W and (0.46, 460) 1/s for k.
- Initial values for D_W and k are chosen as: 5 **($*10^{-14}$)** m^2/s and 50 **($*10^{-5}$)** 1/s, respectively.
- The objective_function_1 must be minimized.

Similarly, the design variables for the second optimization model targeting GFs and GFp are chosen as the following design parameters affecting the GF release performance based on the corresponding PDE in Equation 3.5.

- Degradation rate of GF (d_G)
- Release constant of GF (r_G)
- Michaelis Menten constant (K_M)

The optimization is subject to the following constraints:

- Lower and upper bounds for each decision variable. These limits are chosen as: (0.04, 50) 1/s for d_G, (0.1, 20) 1/s for r_G and (0.01, 20) for K_M.
- Initial values for d_G, r_G and K_M are chosen as: 1 **($*10^{-7}$)** 1/s for d_G, 0.9 **($*10^{-5}$)** 1/s for r_G, and 1.5 for K_M.
- The objective_function_2 must be minimized.

Since the values of each variable in both models are in different magnitudes, they are scaled for the optimizers and still their original values are fed back to the COMSOL model. For example, values of D_W are on the order of 10^{-14} while that of k is 10^{-7} in the

COMSOL model called by the optimizer. For iterations steps of fmincon function, they multiplied by 10^{14} and 10^{7}, respectively. After each iteration of the optimizer, the parameters are turned back to their original values and written into COMSOL for the next run. The same is applied to the second model for d_G and r_G. Thus, the values provided in bulletheads for each variable are for the optimizer, they multiplied with the multiplier within the parenthesis, written bold, next to them.

The fmincon function in MATLAB was chosen for the optimization due its suitability to gradient based optimization and coupled to the COMSOL simulation model using MATLAB scripting. Problems involving a limited number of variables within a nonlinear optimization such as our integrated model are known to deliver efficient converging solutions but are known to be initial design dependent due to its local nature. The 'sqp' (Sequential Quadratic Programming) algorithm was selected among its available algorithms due to its precision and efficiency. Sequential Quadratic Programming (SQP) is an iterative method suitable for constrained nonlinear optimization models. At each iteration, SQP solves a Quadratic Programming (QP) subproblem, which approximates the original nonlinear problem. First, SQP finds an approximate model of the objective function and constraints are created using an approximate quadratic function of the objective and linear approximation of the constraints. Then, the QP subproblem is solved to determine the search direction. A line search or trust region method is used to find a step size that ensures sufficient decrease in the objective function. After arranging an appropriate step size for iteration direction, the variables are updated, and the process is repeated until convergence. The Hessian for an unconstrained problem is the matrix of second order derivatives of the objective function delivering a square matrix of the objective function's second-order partial derivatives. It offers key information regarding the function's curvature, which is helpful in choosing the direction and size of the search step during optimization. Since the Hessian matrix is employed in the SQP technique to define the QP subproblem, it is precise in terms of its higher order approximation when compared with first order methods yet capable of performing effective optimization.

Both optimization models use two different files; an M-file consisting of optimization scripts and an mph-file to perform COMSOL runs. Starting the optimization involves running the m-file, which contains the main optimizer that establishes communication between the two environments, initializes all necessary variables, and calls the objective function using the fmincon function. Once the fmincon function is executed within the main file, it calls the objective file which defines and calls the COMSOL model to be solved in each iteration of the fmincon function. During this process, the values of the optimization variables are changed to compute the subsequent objective functions by extracting the COMSOL run outputs and using these to compute to objective functions. Until the minimal value of the objective function is found, this iteration loop continues delivering a converged set of optimization variable values. The main code and script for optimization model 2 is provided as an example in Appendix C1 and C2.

CHAPTER 4

4. RESULTS

4.1.Results for Background Validation of 2D Axi-symmetric Geometry

The time-dependent concentration changes of spherical CaP scaffolds obtained solving coupled reaction-diffusion equations given in Equation 3.1 and 3.2 are shown (Figure 13). To observe the effect of crystallinity of the polymer matrix, this validation study was adapted from Rothstein et al. and the simulation was run at 4 different hydrolysis rate constants representing crystallinity of polymer matrices (Rothstein et al., 2009).

With a very slow degradation rate constant at the order of 10^{-11}, there is no bulk degradation observed (Figure 13c). The polymer concentration remains the same at the initial concentration value at the end of the 12-month period (the very below line) indicating that the degradation behavior totally obeys the surface degradation mode. This behavior is observed with high crystallinity polymer matrices such as poly(lactic-co-glycolic) acid (PLGA). Increasing the reaction rate constant 100 times (Figure 13a), bulk degradation mode starts to appear due to a linear decrease in polymer concentration over time within the depths of the scaffold matrix. However, still surface degradation mode is dominant since the polymer concentration is still 0.9 at the center at the last time step while the concentration drops more than half at the outer surface. The plots in (b) and (d) were obtained by decreasing the rate constant 100 times further while the rate constant in (b) is almost 3 times larger than that of (d). Both have a degradation mode closer to bulk, which implies that to alter the overall degradation behavior, the rate constant should be varied in high orders of magnitudes such as on the order of 100-fold. A three-fold difference only seems to affect the last 6 months.

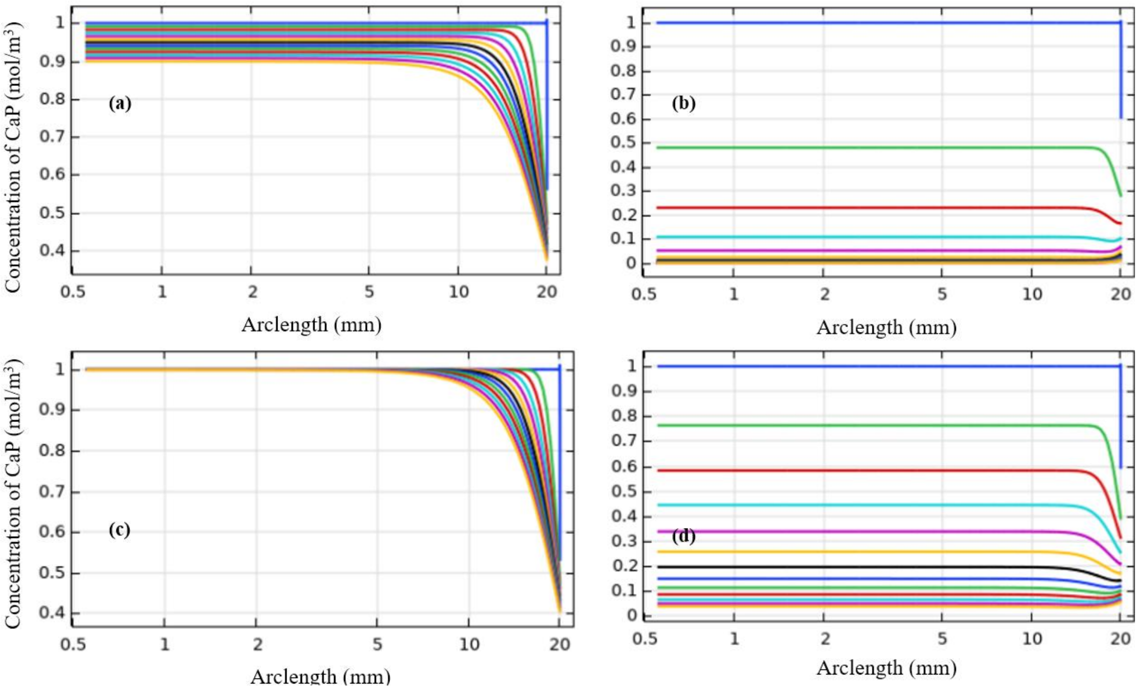

Figure 13: Concentration profiles of 2 cm spherical scaffolds with different degradation rate constants are shown. a) The $k=8.75x10^{-9}$ 1/s, b) $k=7.32x10^{-7}$ 1/s, c) $k=3.85x10^{-11}$ 1/s, d) $k=2.7x10^{-7}$ 1/s. Each line represents time, the blue line (on the top of each plot) represents the t=0, and the simulation was run for 1 month time steps.

To validate the developed simulation model, model parameters were assigned the same values as given in Rothstein et al. (Figure 14 and 15) using the same matrix radius and time steps. The validation study was performed for two scaffolds sizes of 20 mm and 2 mm. The time period was taken as 12 months as in the reference study (Rothstein et al., 2009). In Figure 14, the hydrolysis rate constant and diffusivity of water were taken as $5x10^{-4}$ 1/s and $3.7x10^{-12}$ m^2/s, respectively. It can be seen that the degradation behaviors in both scaffold sizes were very similar. For the smaller scaffold size of 2 mm, reaction rate constant and water diffusion coefficient was $6x10^{-5}$ 1/s and $1.5x10^{-13}$ m^2/s, respectively. This consistency was assumed to validate our previous analysis (given in Figure 13). The differences between variables are due to the scaffold sizes. As indicated in the reference model, larger matrix sizes will have a sharper water concentration gradient of water since the penetration distance of water increases with the size.

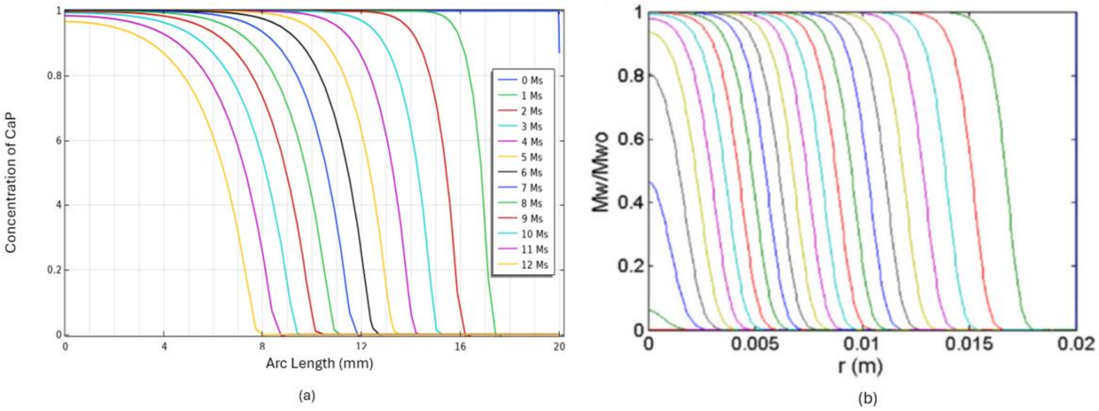

(a) (b)

Figure 14: Comparison of the model results with the reference study for 20 mm scaffold size. (a) Our simulation results (b) Reference study results. (Rothstein et al., 2009).

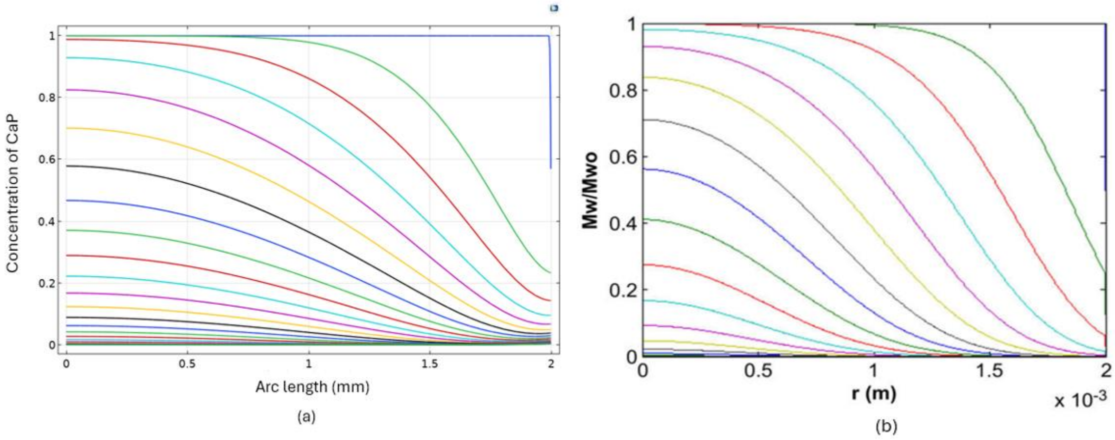

(a) (b)

Figure 15: Comparison of the model results with the reference study for 2 mm scaffold size. (a) Our simulation results (b) Reference study results. (Rothstein et al., 2009).

4.2.COMSOL Model Results of Degradation and Growth Factor Release

After validating the reference model for mainly the diffusion-reaction equations on a simple 2 D model as discussed in the previous section, the model was extended to a 3D scaffold geometry incorporating the degradation mechanism to a GF release model which is discussed in this section.

First, we constructed a polymer degradation and growth factor release system enhancing bone regeneration and investigated effective parameters tailoring concentrations on the model. The nondimensional molecular weight of the scaffold was evaluated on days 7, 14, 21 and 28. The data is extracted from a point near to a scaffold boundary on the yz plane (Figure 16). Although the most effective parameters for polymer degradation in the simulation was diffusivity of water (D_W) and reaction rate constant (k), other parameters related to growth factor dynamics are investigated and taken into consideration in the parametric study performed in this thesis. More specifically, the parametric study considering D_W, and k was performed to analyze the degradation behavior of the scaffold. Meanwhile, diffusivity of the growth factor (D_G) was kept constant to see the role of the other two parameters on polymer concentration. For degradation rate (d_G) and release rate (r_G) of growth factor, there was no observable effect on polymer concentration results, thus their variations were ignored in the following analysis. Based upon the literature, the diffusivity of water value ranges from $4.6x10^{-16}$ m²/s to $4.6x10^{-12}$ m²/s and polymer degradation rate constant, k ranges from $8.3x10^{-6}$ 1/s to $8.3x10^{-8}$ 1/s in different environments and similar use of polymer materials, suggesting different combinations in consideration to other model parameters (Little et al., 2008; Ribeiro et al., 2015; X. Sun et al., 2013; L. Wang et al., 2020).

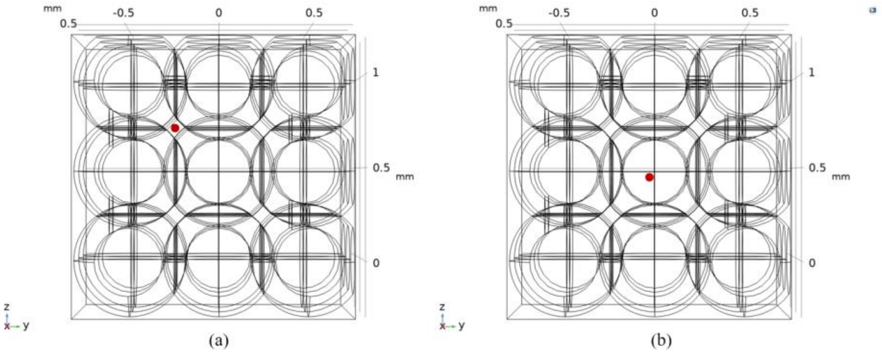

Figure 16: Representative points of scaffold and pore domains where numerical concentration results are extracted (a) point on scaffold with coordinates (1.2, -0.24, 0.72), and (b) point in pore at coordinates (0.45, -0.03, 0.45). All dimensions are in mm.

The results are shown in Tables 6-10 and a more detailed version in Appendix D. Unless otherwise noted, Mi indicates the normalized polymer concentration at the i^{th} day and Gsi/Gpi indicates the normalized GF concentration at the i^{th} day in the scaffold vs. pore. Overall, the results indicate that degradation rate of the bone scaffold can be tuned for specific purposes by tuning hydrolysis reaction rate and diffusivity of water. In addition to controlling degradation rate, degradation behavior is a result of the interplay between k and D_W. As expected, higher values of k and D_W fasten the degradation rate of the scaffold. When D_W is 4.6×10^{-14} m^2/s with k of 8.3×10^{-8} 1/s, the scaffold degrades very slowly, reducing from 0.95 on day 7 to 0.81 on day 28. Increasing k to 8.3×10^{-7} 1/s, almost 20% degradation was achieved at day 7 and the nondimensional concentration of scaffold is 0.46 at day 28. At k=8.3×10^{-6} 1/s M is almost completely degraded by day 7 (M7=0.05). For D_W of 4.6×10^{-16} m^2/s and k of 8.3×10^{-7} 1/s pursues a more dominant surface degradation behavior, increasing D_W to 4.6×10^{-12} m^2/s while keeping k constant enhances water diffusion into the scaffold and bulk degradation becomes dominant (Table 6). This implies that for the chosen geometry and dimensions, D_W of 4.6×10^{-16} m^2/s still allows water penetration through the scaffold while the value is comparably smaller than the literature where larger values are cited (Rothstein et al., 2009). For higher values of hydrolysis rates, for example when k is 8.3×10^{-6} 1/s, degradation rate is brutally fast.

For D_W values smaller than 4.6×10^{-14} m^2/s, extending down to 10^{-16}, the degradation of scaffold slows down due to decreasing penetration of water molecules to scaffold and varies with different k values. On the contrary, the numerical results imply that higher values than 4.6×10^{-14} m^2/s for water diffusivity does not affect the scaffold concentration regardless of k values. This implies that 4.6×10^{-14} m^2/s for D_W is large enough to allow diffusion through the scaffold's struts for the given geometry.

With D_W=4.6×10^{-12} m^2/s and k ranging from 8.3×10^{-7} to 4×10^{-7} 1/s, molecular weight at day 7 changes between 0.66 and 0.81. When k is 8.3×10^{-6} 1/s, M7 is approximately 0.05, indicating almost complete degradation in the first week. Besides, having k values around 10^{-6} 1/s seems to be the best value capable of controlling the variation of M values between weeks. Similarly, reducing diffusion of water decreases the percentage drop in molecular weight of the polymer. The reason for preventing water penetration to the scaffold is to limit the degradation reaction of the surface of the scaffold rather than causing bulk degradation of the material. The closest polymer concentration values to the simulation data of the chosen reference study of Sun et al. are attained with D_W values of 4.6×10^{-14} m^2/s or higher, and hydrolysis rate constants of 3×10^{-7} 1/s and 4×10^{-7} 1/s where k values with higher than 4×10^{-7} (5×10^{-7}) 1/s causes scaffold concentration to drop to 0.78 by day 7 and to 0.39 by day 28 (X. Sun et al., 2013). Furthermore, there is no observable effect on M for D_W values of 4.6×10^{-14} m^2/s r or higher neither in degradation rate nor its mechanism. The molecular weight distribution plot verifies this outcome as shown in Table 7. It may indicate that for the designed scaffold, D_W of 4.6×10^{-14} m^2/s is a sufficient value for the diffusion rate of water that maintains the degradation mode in a balance between surface and bulk degradation mechanisms. This allows a design flexibility of the scaffold in regard to its properties in tailoring them to reach a desired mechanical property.

Table 6: Numerical results of parametric analysis for weekly change in non-dimensional polymer concentration in scaffold domain. Initial concentration was assigned as M0 is 1 (DW in water is 10 times higher than the in polymer value).

DW in polymer [m^2/s]	**k [1/s]**	**M7**	**M14**	**M21**	**M28**
4.6E-16	8.3E-07	**0.90**	**0.78**	**0.66**	**0.55**
4.6E-15	3.0E-07	**0.90**	**0.78**	**0.67**	**0.58**
4.6E-15	8.3E-07	**0.78**	**0.55**	**0.39**	**0.28**
4.6E-15	1.0E-06	**0.75**	**0.50**	**0.34**	**0.21**
4.6E-14	8.3E-08	**0.95**	**0.90**	**0.86**	**0.81**
4.6E-14	3.0E-07	**0.86**	**0.74**	**0.64**	**0.55**
4.6E-14	4.0E-07	**0.82**	**0.67**	**0.56**	**0.47**
4.6E-14	5.0E-07	**0.78**	**0.62**	**0.49**	**0.40**
4.6E-14	6.0E-07	**0.74**	**0.57**	**0.44**	**0.34**
4.6E-14	8.3E-07	**0.67**	**0.47**	**0.34**	**0.23**
4.6E-14	8.3E-06	**0.05**	**0.01**	**0.01**	**0.00**
4.6E-13	3.0E-07	**0.85**	**0.73**	**0.64**	**0.56**
4.6E-13	8.3E-07	**0.66**	**0.46**	**0.33**	**0.24**
4.6E-12	3.0E-07	**0.85**	**0.74**	**0.64**	**0.55**
4.6E-12	4.0E-07	**0.81**	**0.67**	**0.56**	**0.47**
4.6E-12	5.0E-07	**0.77**	**0.61**	**0.49**	**0.40**
4.6E-12	8.3E-07	**0.67**	**0.47**	**0.34**	**0.24**

The distribution plots are more useful for analyzing the degradation mode in more detail than point data and are provided in Table 7. When the hydrolysis rate constant is kept constant at 3x10^{-7} 1/s a decrease in water diffusivity of 10-fold causes a slower degradation and higher polymer concentration near the outer boundaries of the scaffold. This information might not be captured by only analyzing the point data; thus, concentration profiles should be examined. By only changing the diffusion coefficient of water 1x10^{-4} times, the polymer is forced to almost totally degrade at the last time step (the bottom row). However, it is obvious that degradation rate constant is more effective in tailoring the polymer concentration profile rather than water diffusivity. Also, one of the outcomes from the point data was that water diffusivity is not effective for values higher than 4.6x10^{-14} m^2/s. Table 7 proves that this outcome is valid only at that point. Hence, it can be stated that the effect of water diffusivity is less pronounced as we move away from the water interface.

Table 7: 2D cross-sectional concentration distributions of scaffold molecular weight for different D$_W$-k values at the course of 4 weeks where Mi is descriptive of the ith day. The results are captured near the yz plane at x=-0.05 mm.

DW in polymer [m^2/s]	DW in water [m^2/s]	k1 [1/s]	M0	M7	M14	M21	M28
4.6E-16	4.6E-15	8.3E-07	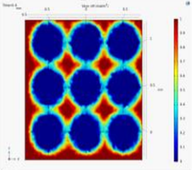	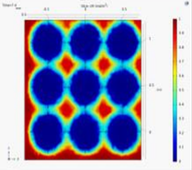	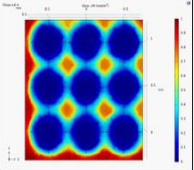	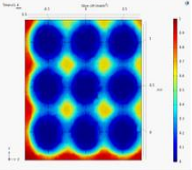	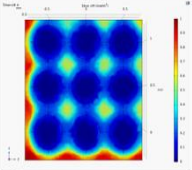
4.6E-15	4.6E-14	3.0E-07	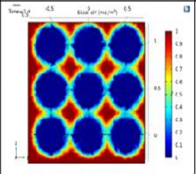	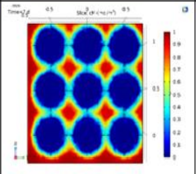	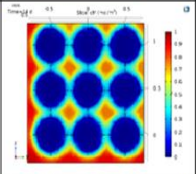	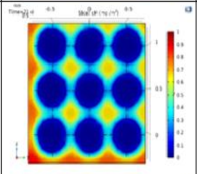	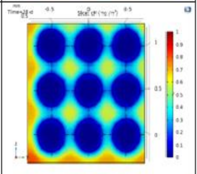
4.6E-14	4.6E-13	8.3E-08	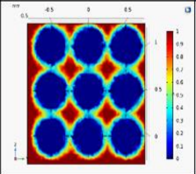	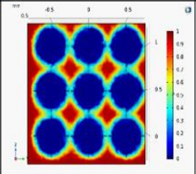	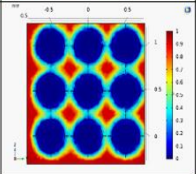	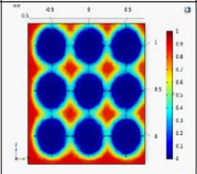	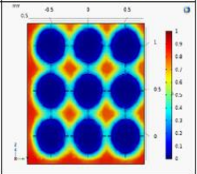
4.6E-14	4.6E-13	3.0E-07	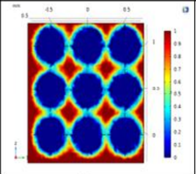	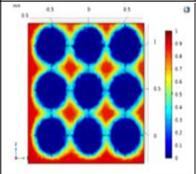	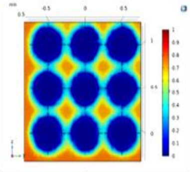	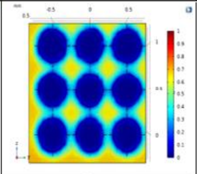	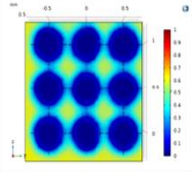
4.6E-14	4.6E-13	8.3E-06	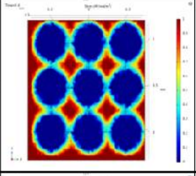	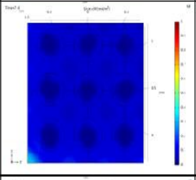	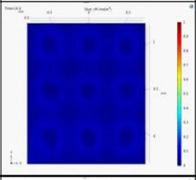	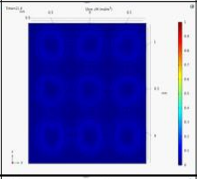	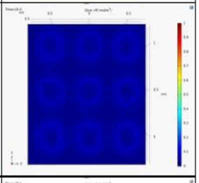
4.6E-12	4.6E-11	8.3E-07	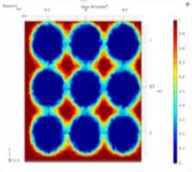	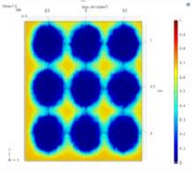	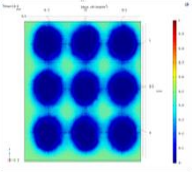	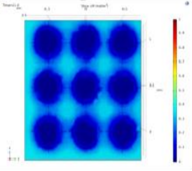	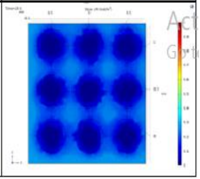

We also examined growth factor release and spatio-temporal distribution of growth factor concentration (Tables 8, 9, 10). The results were obtained from the exact same point date used in Table 6 and shown in Figure 16. The diffusivity of the growth factor ranged from 2.9x10^{-16} m^2/s to 2.9x10^{-14} m^2/s while the other parameters were varied to analyze the effect of each parameter separately. Thus, Tables 8, 9 and 10 consist of data obtained using D_G=2.9x10^{-16}, 2.9x10^{-15} and 2.9x10^{-14} m^2/s, respectively. GFs initially only present at scaffold surface and time independent diffusivity of GF is 1000 times higher in pores (for all simulations). For D_W of 4.6x10^{-14} m^2/s and k of 8.3x10^{-7} 1/s (d_G = 3.4x10^{-7} 1/s and r_G= 2x10^{-5} 1/s); increasing D_G from 2.9x10^{-16} m^2/s to 2.9x10^{-15} m^2/s decreases Gs and increases Gp. However, increasing D_G further to 2.9x10^{-14} m^2/s does not affect Gs while it keeps increasing Gp values. For values of D_W= 4.6x10^{-12} m^2/s and k = 8.3x10^{-7} 1/s (d_G = 3.4x10^{-7} 1/s and r_G = 2x10^{-5} 1/s); increasing D_G from 2.9x10^{-16} to 2.9x10^{-15} m^2/s decreases Gs and increases Gp over the course period at all days. Increasing D_G further to 2.9x10^{-14} m^2/s continues increasing Gpore while decreasing Gscaff values. For D_W = 4.6x10^{-12} m^2/s and k = 4x10^{-7} 1/s (d_G = 1x10^{-8} 1/s and r_G = 2x10^{-5} 1/s); raising D_G from 2.9x10^{-16} m^2/s to 2.9x10^{-15} m^2/s results higher GF concentration in pores at day 7 (from 0.55 to 0.60) but no change at day 28 (0.78). In the scaffold domain, the same changes induce a decrease in GF concentration at day 7 (from 0.74 to 0.72) and no change in day 28 as was the case earlier. An order of magnitude increases of D_G to 10^{-14} from 10^{-15} m^2/s has exactly the same effect on each day both in the scaffold and pores.

Table 8: Numerical results of parametric analysis for weekly change in growth factor concentration in scaffold and pores. Initial concentration was assigned as G0 in pore-matrix interface as 0.8 (D_G is 2.9x10^{-16} m^2/s; D_W in water is 10 times higher than the in polymer value).

DW in polymer [m^2/s]	**k1 [1/s]**	**dGi [1/s]**	**rGi [1/s]**	**Pores**				**Scaffold**			
				G7	**G14**	**G21**	**G28**	**G7**	**G14**	**G21**	**G28**
4.6E-14	8.3E-07	3.4E-07	2.0E-05	**0.50**	**0.60**	**0.63**	**0.64**	**0.72**	**0.74**	**0.75**	**0.75**
4.6E-14	8.3E-07	1.0E-08	1.0E-05	**0.43**	**0.58**	**0.66**	**0.71**	**0.68**	**0.73**	**0.75**	**0.77**
4.6E-12	8.3E-07	3.4E-07	2.0E-05	**0.50**	**0.60**	**0.63**	**0.64**	**0.72**	**0.74**	**0.75**	**0.75**

4.6E-12	4.0E-07	3.4E-07	2.0E-05	**0.50**	**0.61**	**0.64**	**0.64**	**0.72**	**0.74**	**0.75**	**0.75**
4.6E-12	4.0E-07	1.0E-08	2.0E-05	**0.56**	**0.71**	**0.76**	**0.78**	**0.75**	**0.78**	**0.79**	**0.80**
4.6E-12	4.0E-07	1.0E-08	1.0E-05	**0.43**	**0.58**	**0.67**	**0.72**	**0.68**	**0.73**	**0.75**	**0.78**

A decreasing value of D_G (where $D_W = 4.6x10^{-12}$ m²/s, $k = 4x10^{-7}$ 1/s, $d_G = 1x10^{-8}$ 1/s and $r_G = 2x10^{-5}$ 1/s) gives a rise to the gap between weekly GF concentration results in pores. As D_G decreases, GF tends to diffuse to the pore domain rather than the scaffold domain especially in the first week. For $D_W = 4.6x10^{-12}$ m²/s and $D_G = 2.9x10^{-15}$ m²/s (with $d_G = 3.4x10^{-7}$ 1/s and $r_G = 2x10^{-5}$ 1/s) with a decrease of k value from $8.3x10^{-6}$ to $8.3x10^{-7}$ 1/s, Gp and Gs slightly increases at all days, however the increase is comparatively higher in pores and later days. There is an interplay between hydrolysis rate constant and GF release such that as the degradation rate fastens, GF is released more quickly as we expected intuitively. On the 28th day the concentration of GF at $k = 8.3x10^{-7}$ 1/s attains a value of 0.66 and at $k = 8.3x10^{-6}$ 1/s, GF concentration a value of 0.62. As k increases, GF concentration decreases in the scaffold domain. Here, we would have expected to have a less pronounced but linear relationship between k and D_W values because a decrease in k is expected to cause slower degradation of the scaffold, and occasionally tends to dominate bulk degradation mode. In a more slowly degrading matrix, while all other parameters are constant, GF is expected to be released more slowly, especially in a matrix that is prone to bulk degradation. For $D_G = 2.9x10^{-15}$ m²/s (with $d_G = 3.4x10^{-7}$ 1/s and $r_G = 2x10^{-5}$ 1/s; even though the D_W value is increased from the order of 10^{-14} to 10^{-12} while k is kept constant at $3.4x10^{-6}$ 1/s, GF concentration results are the same in both pores and scaffold. This is valid at different k values such as $8.3x10^{-7}$ 1/s where D_W changes between orders of 10^{-14} and 10^{-12} m²/s. For $D_W = 4.6x10^{-14}$ m²/s, $D_G = 2.9x10^{-15}$ m²/s, $k = 8.3x10^{-7}$ 1/s, and $r_G = 2x10^{-5}$ 1/s; and a d_G value of $5x10^{-9}$ 1/s, scaffold domain values of GF concentration at day 28 reach a value of 0.737 whereas a value for $d_G = 3.4x10^{-7}$ 1/s the GF concentration reaches a higher value of 0.795 than for $d_G = 5x10^{-9}$ 1/s. Also, a similar effect on day 7 is to day 28 is observed.

Table 9: Numerical results of parametric analysis for weekly change in growth factor concentration in scaffold and pores. Initial concentration was assigned as G0 in pore-matrix interface as 0.8 (D_G is $2.9x10^{-15}$ m^2/s; D_W in water is 10 times higher than the in-polymer value).

DW in polymer [m^2/s]	k1 [1/s]	dGi [1/s]	rGi [1/s]	Pores				Scaffold			
				G7	**G14**	**G21**	**G28**	**G7**	**G14**	**G21**	**G28**
4.6E-14	8.3E-07	3.4E-07	2.0E-04	**0.78**	**0.78**	**0.78**	**0.78**	**0.80**	**0.80**	**0.80**	**0.80**
4.6E-14	8.3E-07	3.4E-07	7.0E-05	**0.73**	**0.75**	**0.75**	**0.75**	**0.79**	**0.79**	**0.79**	**0.79**
4.6E-14	8.3E-07	2.4E-07	2.0E-05	**0.56**	**0.66**	**0.69**	**0.70**	**0.71**	**0.74**	**0.75**	**0.75**
4.6E-14	8.3E-07	3.4E-07	2.0E-05	**0.54**	**0.63**	**0.66**	**0.66**	**0.70**	**0.73**	**0.74**	**0.74**
4.6E-14	8.3E-07	3.4E-07	1.0E-05	**0.42**	**0.51**	**0.55**	**0.56**	**0.59**	**0.63**	**0.65**	**0.66**
4.6E-14	8.3E-06	3.4E-07	2.0E-05	**0.52**	**0.60**	**0.62**	**0.62**	**0.68**	**0.71**	**0.71**	**0.71**
4.6E-14	4.0E-07	3.4E-07	2.0E-05	**0.55**	**0.64**	**0.66**	**0.67**	**0.70**	**0.73**	**0.74**	**0.74**
4.6E-14	8.3E-08	3.4E-07	2.0E-05	**0.55**	**0.64**	**0.66**	**0.67**	**0.70**	**0.73**	**0.74**	**0.74**
4.6E-14	8.3E-07	2.4E-07	1.0E-05	**0.43**	**0.54**	**0.58**	**0.61**	**0.60**	**0.65**	**0.68**	**0.69**
4.6E-14	8.3E-07	1.0E-07	2.0E-05	**0.58**	**0.70**	**0.74**	**0.75**	**0.72**	**0.76**	**0.77**	**0.78**
4.6E-14	8.3E-07	8.0E-08	2.0E-05	**0.58**	**0.71**	**0.75**	**0.76**	**0.72**	**0.76**	**0.78**	**0.78**
4.6E-14	8.3E-07	5.0E-08	2.0E-05	**0.59**	**0.72**	**0.76**	**0.77**	**0.72**	**0.77**	**0.78**	**0.79**
4.6E-14	8.3E-07	1.0E-08	2.0E-05	**0.60**	**0.73**	**0.77**	**0.79**	**0.73**	**0.77**	**0.79**	**0.80**
4.6E-14	8.3E-07	5.0E-09	2.0E-05	**0.60**	**0.73**	**0.77**	**0.79**	**0.73**	**0.77**	**0.79**	**0.80**
4.6E-12	8.3E-06	3.4E-07	2.0E-05	**0.52**	**0.60**	**0.62**	**0.62**	**0.68**	**0.71**	**0.71**	**0.71**
4.6E-12	8.3E-07	3.4E-07	2.0E-05	**0.55**	**0.64**	**0.66**	**0.66**	**0.70**	**0.73**	**0.74**	**0.74**
4.6E-12	3.0E-07	3.4E-07	2.0E-05	**0.55**	**0.64**	**0.66**	**0.67**	**0.70**	**0.73**	**0.74**	**0.74**
4.6E-12	4.0E-07	1.0E-08	2.0E-05	**0.61**	**0.73**	**0.77**	**0.79**	**0.73**	**0.78**	**0.79**	**0.80**
4.6E-12	4.0E-07	1.0E-08	1.5E-05	**0.55**	**0.69**	**0.75**	**0.77**	**0.69**	**0.75**	**0.78**	**0.79**
4.6E-12	4.0E-07	1.0E-08	1.0E-05	**0.47**	**0.61**	**0.69**	**0.74**	**0.63**	**0.70**	**0.74**	**0.77**

Besides, a shift in the d_G value causes a decrease in GF concentration in pores with values of 0.78 dropping to 0.66 at day 28 and concentrations decreasing from 0.59 to 0.54 at day 7. It can be stated that the d_G value has a more dominant effect in the pore domain because the change in scaffold is around 0.06 and reaches a value of 0.12 on day 28. For D_W = $4.6x10^{-12}$ m^2/s, k = $8.3x10^{-7}$ 1/s, D_G = $2.9x10^{-15}$ m^2/s, and r_G = $2x10^{-5}$ 1/s; decreasing d_G value below $1x10^{-8}$ 1/s does not affect the GF concentration neither in pores nor the scaffold domain. For d_G values of $3.4x10^{-7}$ 1/s; r_G can tune GF concentration with a value of $2x10^{-5}$ 1/s and less because its higher values result in saturated GF concentrations in both pores and scaffold at all days. However, r_G can tune GF when its values are at levels of $1x10^{-5}$ 1/s or less if $d_G = 2.4x10^{-7}$ 1/s. Thus, for smaller degradation constants of GF, its release rate should be arranged accordingly considering higher d_G values are likely to result in less GF present. Furthermore, changing d_G or D_G values has no effect when r_G values are equal to $7x10^{-5}$ 1/s and $2x10^{-4}$ 1/s due to significantly higher values of its release constant. For $d_G = 3.4x10^{-7}$ 1/s, the greatest jump in GF concentration among days were obtained when r_G values are in the range of $2x10^{-5}$ 1/s and $7x10^{-6}$ 1/s. If GFs are released more slowly, with r_G values ranging from $1x10^{-8}$ 1/s to $7x10^{-6}$ 1/s, the GF concentration saturates as well but to smaller values than the desired values of the reference study. The desired concentration of GF at around 0.8 in the last two weeks is achieved with r_G values larger than or close to $1x10^{-5}$ 1/s.

Table 10: Numerical results of parametric analysis for weekly change in growth factor concentration in scaffold and pores. Initial concentration was assigned as G0 in pore-matrix interface as 0.8 (D_G is $2.9\mathrm{x}10^{-14}$ m^2/s; D_W in water is 10 times higher than the in-polymer value).

D_W in polymer [m^2/s]	**k [1/s] (x10^{-7})**	**d_G [1/s] (x10^{-7})**	**r_G [1/s] (x10^{-5})**	**Pores**				**Scaffold**			
				G7	**G14**	**G21**	**G28**	**G7**	**G14**	**G21**	**G28**
$4.6\mathrm{x}10^{-12}$	4.0	0.1	2.0	**0.64**	**0.76**	**0.79**	**0.79**	**0.71**	**0.77**	**0.79**	**0.80**
$4.6\mathrm{x}10^{-12}$	8.3	3.4	2.0	**0.59**	**0.67**	**0.68**	**0.68**	**0.68**	**0.72**	**0.73**	**0.72**
$4.6\mathrm{x}10^{-14}$	8.3	0.1	2.0	**0.64**	**0.76**	**0.79**	**0.79**	**0.72**	**0.78**	**0.79**	**0.80**
$4.6\mathrm{x}10^{-14}$	8.3	3.4	2.0	**0.59**	**0.67**	**0.68**	**0.68**	**0.70**	**0.72**	**0.73**	**0.72**

In order to analyze the complete response, GF concentration distribution results are also plotted throughout the whole scaffold geometry. as their visual inspection is important rather than relying on a single point data as provided in Tables 8, 9 and 10 that were obtained from two representative points selected from the scaffold domain and the pore domain, respectively. Table 11 shows the concentration distribution of GF in the analyzed 4-week time period, for different values of the considered parameters. Although polymer concentration profiles give more insight on the degradation mode, in the case of growth factors, their distributions seem to be not of relevance since they result in almost totally uniform distributions in each time step in both domains. It is also noted that the interface of pore-matrix is initially loaded with growth factors and their diffusion is mostly through the pore domain (as can be observed from Tables 8, 9 and 10) due to the relatively large difference orders of diffusivities (which is 1000-fold higher in the pores than the scaffold).

Table 11: 2D cross-sectional concentration distribution of released growth factor from scaffold-pore interface for different diffusivity of water and growth factor, release and degradation constants of GF. The values are taken at the course of 4 weeks where Gi is descriptive of the GF concentration at the ith day. The results are captured near the yz plane at x=-0.05 mm. DW and DG values in pores are higher by 10x and 1000x than their scaffold domain values, respectively.

DW in polymer [m^2/s]	k1 [1/s]	DG in polymer [m^2/s]	dG [1/s]	rG [1/s]	G0	G7	G14	G21	G28
4.6E-12	4.0E-07	2.9E-16	1.0E-08	1.0E-05	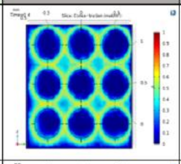	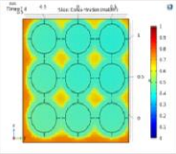	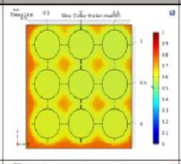	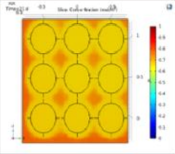	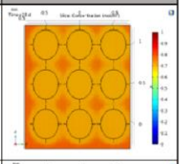
4.6E-14	8.3E-07	2.9E-15	5.0E-09	2.0E-05	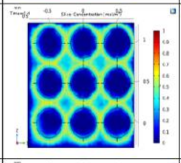	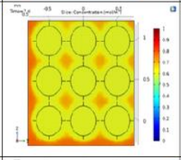	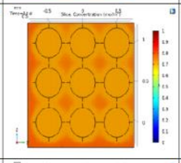	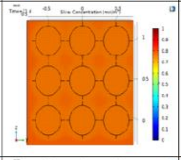	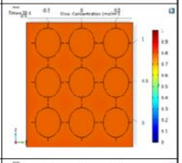
4.6E-13	3.0E-07	2.9E-15	1.0E-08	2.0E-05	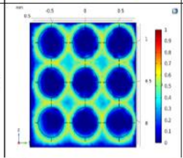	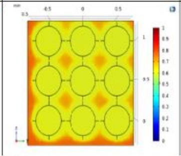	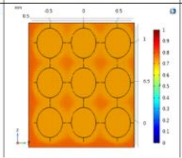	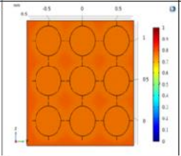	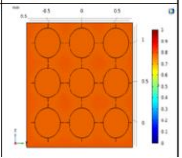
4.6E-14	8.3E-07	2.9E-15	5.0E-08	2.0E-05	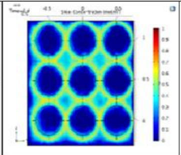	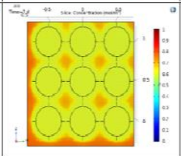	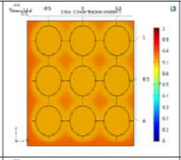	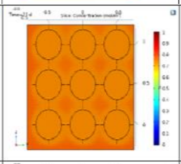	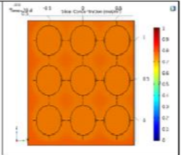
4.6E-14	8.3E-08	2.9E-15	3.4E-07	2.0E-05	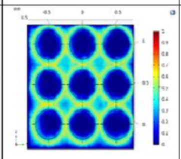	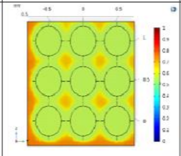	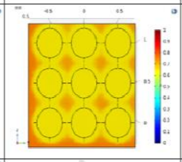	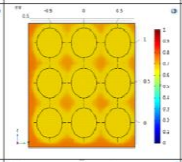	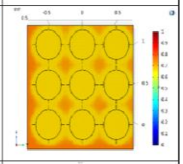
4.6E-14	8.3E-06	2.9E-15	3.4E-07	2.0E-05	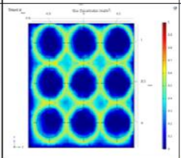	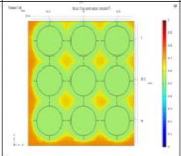	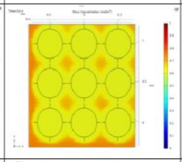	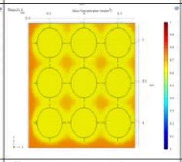	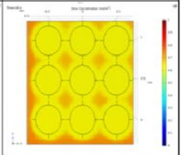
4.6E-14	8.3E-07	2.9E-15	1.0E-05	2.0E-04	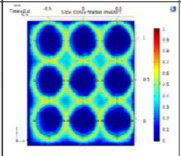	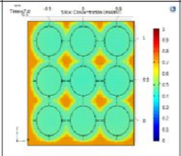	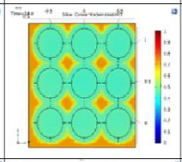	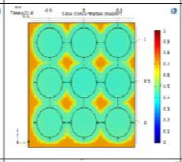	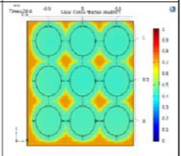
4.6E-16	8.3E-07	2.9E-15	2.4E-07	2.0E-05	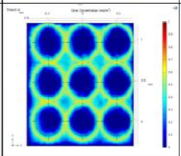	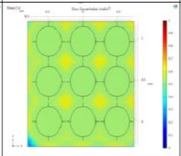	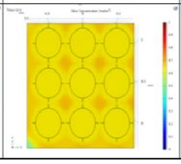	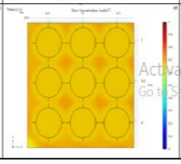	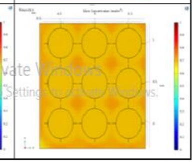

Figure 17 shows the comparison between our simulation and the reference study results as 2D cross-sectional concentration distributions of scaffold molecular weight and released growth factor. The results are obtained with the selected values of each parameter considered in the parametric study. Finally, the values used are: $D_W = 4.6\times10^{-12}$ m²/s, $k = 4\times10^{-7}$ 1/s, $D_G = 2.9\times10^{-15}$ m²/s, $d_G = 1\times10^{-8}$ 1/s and $r_G = 2\times10^{-5}$ 1/s.

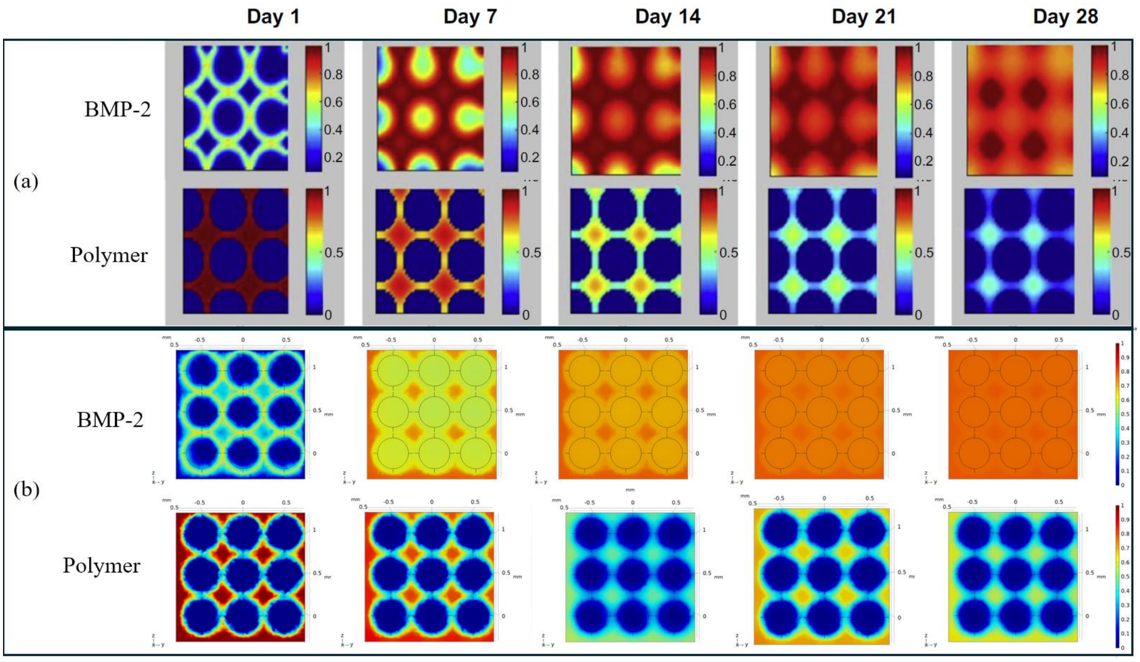

Figure 17: 2D cross-sectional concentration distributions of scaffold molecular weight and released growth factor; a) Reference study results, b) Our simulation results. The profiles are taken over the course of 4 weeks and our results are obtained with the selected parameters as a result of the parametric study. The results are captured near the yz plane at x=-0.05 mm.

The data on cumulative release of BMP-2 from scaffold are provided in Figure 18 and 19. Figure 18 demonstrates the cumulative release of BMP-2 from scaffold for a 4-week period. It shows a consistent behavior with the literature at the same pore size of 300 μm radius (X. Sun et al., 2013). The released cumulative BMP-2 percentage from the matrix-pore interface is shown in Figure 19 compared to the release profile provided in the reference study (X. Sun et al., 2013). It is also noted that their scaffold geometry was the same as ours. On day 28, the cumulative released BMP-2 from interface to pores is 75%. The cumulative release is evaluated on pore domain only although some of the initially loaded BMP-2 remains in scaffold domain due to the decreasing molecular weight of the scaffold. Figure 19 is obtained from a point at the center of the middle spherical pore (shown in Figure 16) which is assumed to be one of the last points that BMP-2 concentration is expected to be kept at its maximum value. As expected, the BMP-2 concentration value at this point reaches almost the maximum and at the same time loaded with an initial GF concentration value of 0.8.

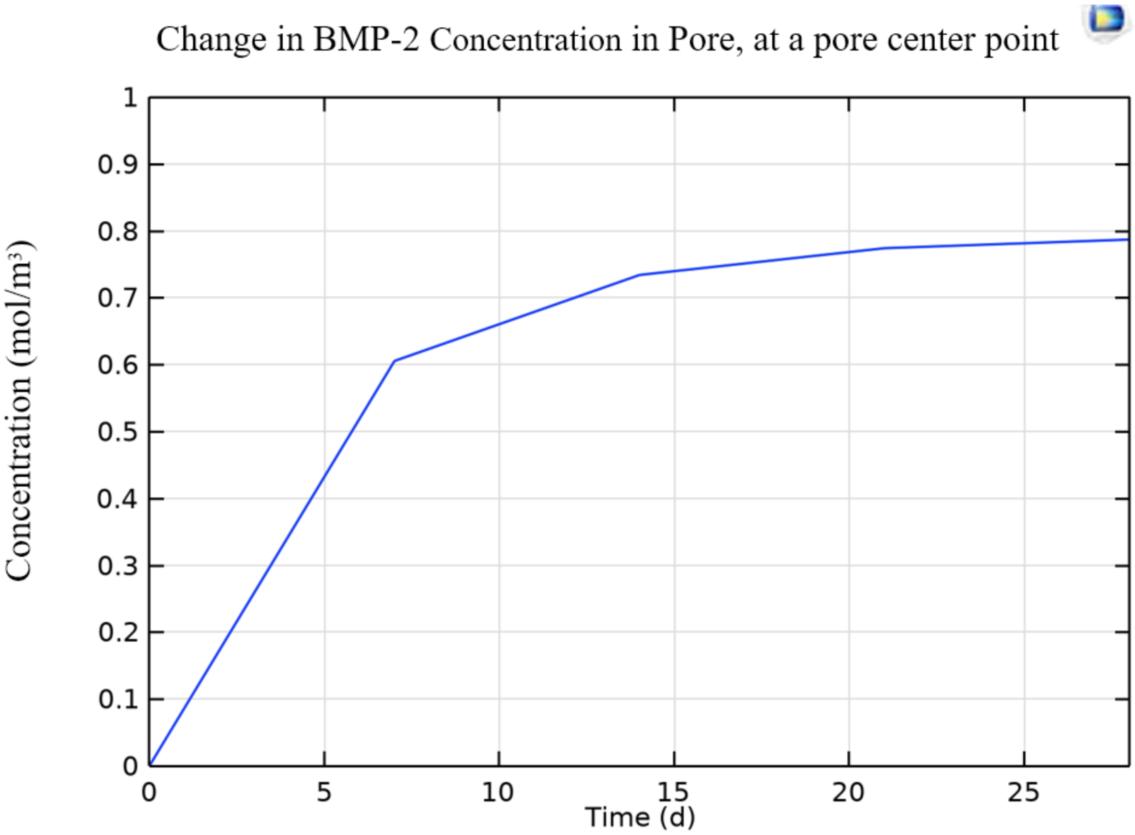

Figure 18: Growth factor/BMP-2 cumulative release prediction from scaffold (measured in the pore domain) at a selected point in the pore domain at (0.45, -0.03, 0.45) coordinates.

To evaluate the cumulative release of BMP-2, the volume average on pores for daily time steps was obtained from the model. Since there is a significant amount of initially loaded BMP-2, the initial volume average value is subtracted from the ones in the later days as shown in Equation 3.35. Then, its percentage is calculated based on our loading amount which is 0.8.

$$Cumulative\ Released\ \% = \frac{\left(V.A.\,in\,pores(t) - V.A.\ \,in\,pores(t=0)\right) * 100}{0.8} \tag{3.35}$$

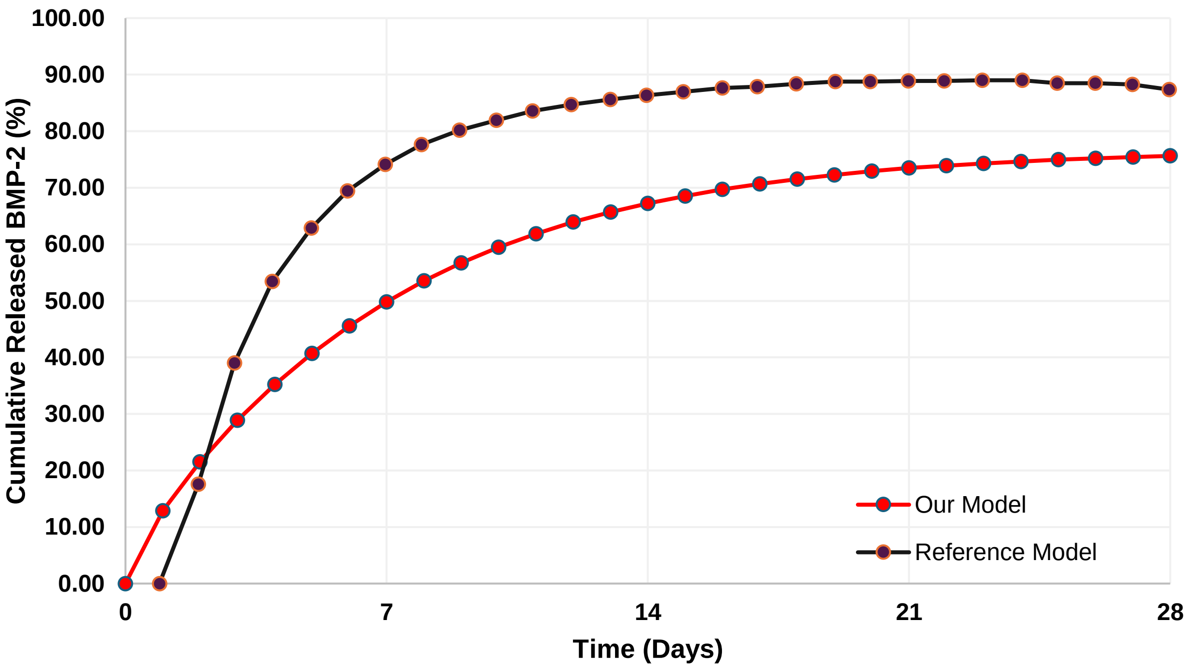

Figure 19: Growth factor/BMP-2 cumulative release prediction from pore-matrix interface compared with the reference model's (X. Sun et al., 2013) cumulative release profile.

4.3.Intracellular Signaling Pathway Results

Dynamic data of BMP-2 activated intracellular signaling pathway results are presented in Figures 20, 21 and 22, respectively. Time span for reaching its steady state for phosphorylated Smad1/5 is determined to be 4 hours. However, this value is comparatively higher than values cited in literature. For example, the reference study Sun et al. reported that phosphorylated Smad2 reaches its steady state in 93 minutes corresponding to a shorter timeframe than half of the calculated steady state value of the model developed in this thesis (X. Sun et al., 2012, 2013). However, corresponding concentration values are consistent with values from the same reference study. Moreover, for phosphorylated Runx2, steady state is reached at around 50 hours. The time required for phosphorylated Runx2 to reach its steady state was found to be around 30 hours in the reference study which implies that our results are not in exact agreement. However, the calculated phosphorylated Smad1/5 results are consistent with phosphorylated Runx2 results of the developed model considering that the Runx2 factor is downstream of Smad1/5 factor. Under the circumstances that Smad1/5 factor is faster reaching a steady state concentration, Runx2 results are expected to directly adapt to the same trend. Also, steady state condition requires more than 50 hours for Osx factor, and that prediction seems to be consistent with cited values of the reference study. However, no information as to when exactly Osx reaches its steady state is provided in the reference study. Thus, we have not enough information to comment on the exact consistency of Osx factor with literature data.

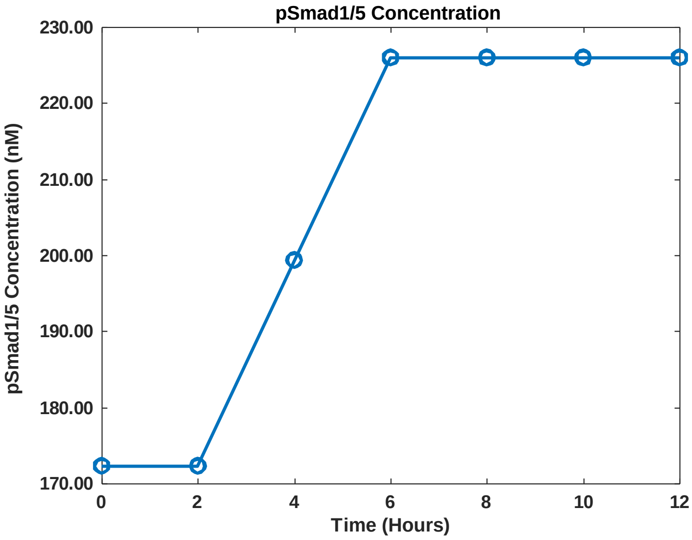

Figure 20: Concentration versus time for phosphorylated Smad1/5.

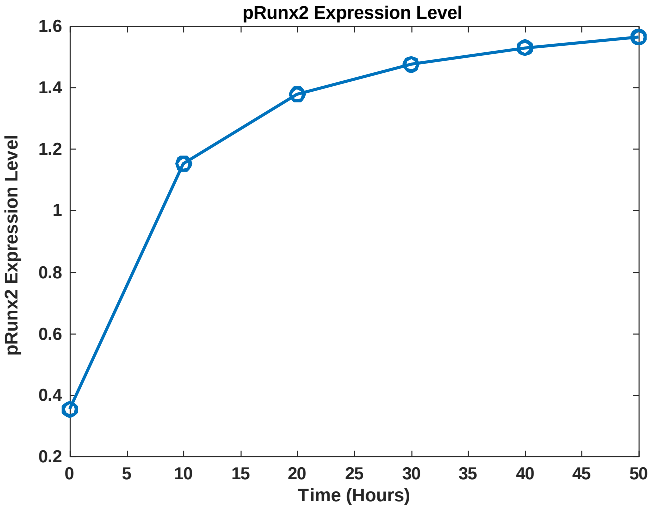

Figure 21: Concentration versus time for Runx2.

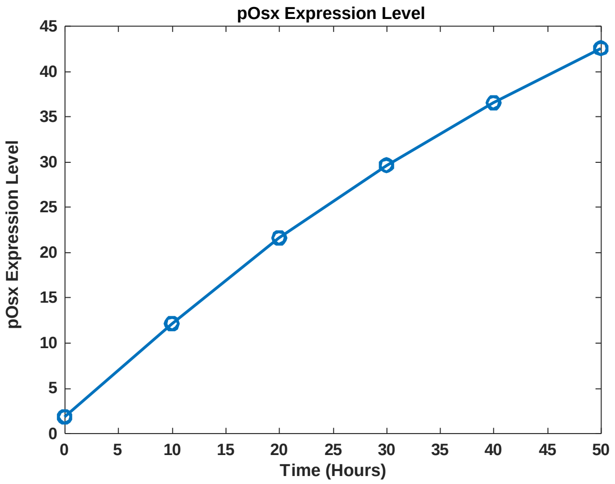

Figure 22: Concentration versus time for phosphorylated Osx.

We can say that the consistent late steady state reaching time frames of both Smad1/5 and Runx2 is most probably due to the difference between the amount of released GF results of our simulation model compared to the reference study. The input of the equation set given in Equation 3.29 of the intracellular signaling pathway model is the BMP-2 concentration as explained in Chapter 3 and there is a linear relationship between BMP-2 concentration and phosphorylated Smad1/5 concentration based on the signaling pathway equations. Our simulation results considering both cumulative release and point data implied that the reference study reaches higher BMP-2 concentrations at 21st day. More importantly, our BMP-2 concentration keeps increasing until the 28th day. This tendency is likely to prevent a steady state behavior of phosphorylated Smad1/5.

4.4.Optimization Results

4.4.1. Optimization Model 1

The primary objective of the optimization model is to minimize a custom-defined objective function that is based in this thesis on matching the desired polymer concentration at 4-time steps, namely day 7, 14, 21 and 28, respectively in the first optimization model presented here as described in Equation 3.33. The chosen design variables correspond to the relevant PDE coefficients and effecting system parameters, namely the reaction rate k and diffusion coefficient of water, D_W, respectively. Initial values for starting the search for their optimal values reaching the desired polymer concentration values of the reference study is chosen to be the design variable vector **x0** = [5x10^{-14} m^2/s, 50x10^{-7} 1/s] where the first element represents the D_w, and the second one is the initial k value. To avoid order of magnitude differences in the design variable values, and hence convergence stability issues when performing sensitivity analysis, these are scaled to values of 5 and 50, respectively in the optimization search itself and their back-scaled magnitudes are fed back when conducting the simulation analysis in COMSOL software with updated values at each iteration of the design cycle. The resulting convergence curve of the objective function for optimization model 1 is given in Figure 23. The value of the sum of square differences from desired concentration values almost diminished completely converging to a value of 0.008.

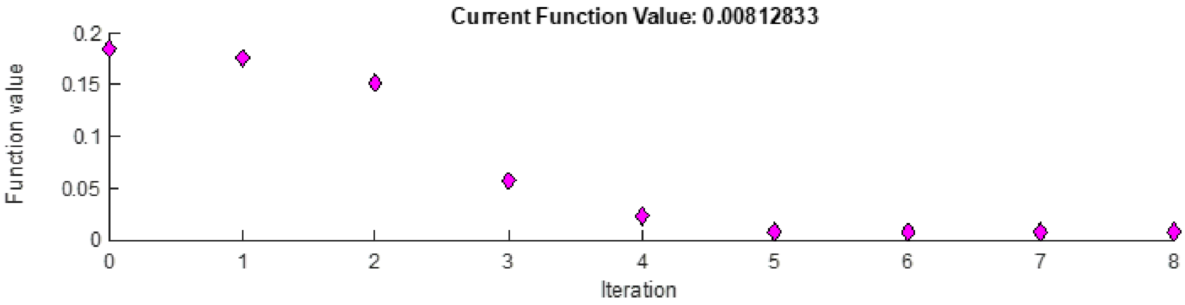

Figure 23: Convergence history of optimization model 1 with design variables D_w and k values to match desired polymer concentration values of the reference study (X. Sun et al., 2013).

The optimization model 1 converged to optimum values for D_w and k presented in Table 12 in comparison with the best parameter set that was determined based on the parametric study outputs of polymer concentration.

Table 12: Optimum values obtained from optimization model 1 vs. the best values obtained via the parametric study presented in Chapter 4.2 .

Parameter	**Best Parameter Set from Parametric Study**	**Optimum Values Found**
D_w (m^2/s)	4.6x10^{-12}	2.99x10^{-12}
k (1/s)	4x10^{-7}	3.85x10^{-7}

The results are within acceptable closeness of the discrete set of values analyzed in the parametric study presented in Chapter 4.2. considering the local nature of the gradient based optimization schemes. This implies that the optimization model is capable of delivering optimal system parameters and the parametric analysis was effective to determine a possible best set of D_W and k within the analyzed ranges of parametric values. The corresponding concentration values at the selected representative point data of the optimal values are also compared with the reference study results (Table 13). Although the parametric study and optimized values of DW are consistent with each other, a deviation still exists in the comparative polymer concentration values especially in the last time step (28th day). Therefore, the developed model in this thesis and the reference study possess model differences attributed to the uncertainties and lack of data in the former as well as possible numerical modeling differences.

Table 13: Comparison of polymer concentration results obtained using optimized design parameter values vs. reference study results over 28-day period.

	Reference Study Results	**Our Results**
M1	1	1
M7	0.8	0.81
M14	0.7	0.68
M21	0.5	0.57
M28	0.3	0.48

4.4.2. Optimization Model 2

The primary objective of optimization model 2 presented in this section, is similar to the first optimization model, namely, to match the desired GF concentration at 4-time steps, namely day 7, 14, 21 and 28, respectively as described in Equation 3.34. The chosen design variables correspond to the relevant PDE coefficients and effecting system parameters, namely the optimization of design parameters d_G, r_G, and K_M assigned as design variables and searched for optimal values to achieve desired growth factor concentration values starting with initial design variable vector **x0** = [$1\text{x}10^{-7}$ 1/s, $0.9\text{x}10^{-5}$ 1/s, 1.5] in the same variable order. Similar to the first optimization model, to avoid order of magnitude differences in the three design variable values, and hence convergence stability issues when performing sensitivity analysis, these are scaled to values of 1, 0.9

and 1.5, respectively in the optimization search itself and their back-scaled magnitudes are fed back when conducting the simulation analysis in COMSOL software with updated values at each iteration of the design cycle. The optimization model 2 converged to optimum values for d_G, r_G, and K_M presented in Table 14. Results in comparison to the best parameter set as determined per the parametric study show a similarity in the orders of magnitude but not exact matching of the parametric study vs. optimization study. The locality of the optimization solver and the finite set of discrete values chosen in the parametric study are likely the sources of the difference in these two parameter sets.
The convergence history of the optimization model 2 is given in Figure 24. The value of the sum of square differences from desired GF concentration values did not diminish completely converging to a value of 0.133 instead of a value close to zero prompting for possible improvements within the local neighborhood of the design domain. However, overall, the proposed optimization models are capable of locating improved design solutions matching desired concentrations at an acceptable level. Further improvements could be achieved with increased number of design variables and additional desired metrics such as the combination of both optimization models as well as integration of desired concentration distributions in the future.

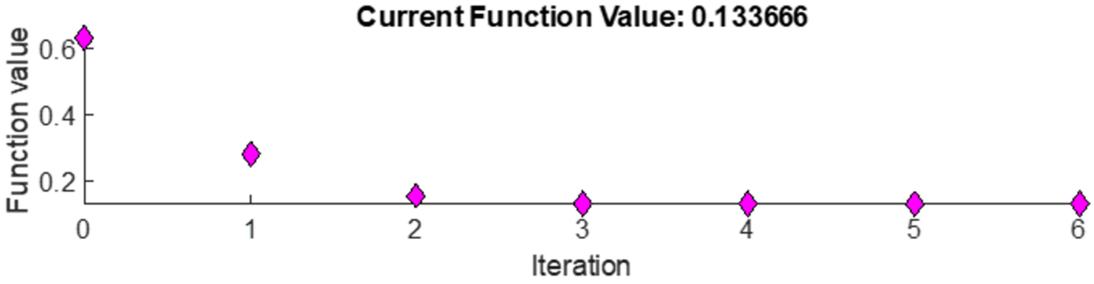

Figure 24: Convergence history curve of optimization model 2 with design variables for d_G, r_G and K_M to match desired GF concentration values (Gp and Gs) of the reference study (X. Sun et al., 2013).

The optimum values of optimization model 2 for design variables found are presented in Table 14 in comparison with the best parameter set that was determined based on the parametric study carried out in Chapter 4.2. Although r_G is found to be very close to the determined value of the parametric study, the optimal value of d_G differs from the pre-determined parametric analysis value by 6-fold. This result can be interpreted as a numerical uncertainty as the parametric study indicated that GF concentration was not as sensitive as to d_G changes among other parameters, and very close GF concentration results were obtained with d_G values of 3.4×10^{-7} 1/s by tailoring r_G in accordance with d_G. This prompts again that a continuous parametric search over a more inclusive design region is needed to exactly match the results of a design optimization model or a given concentration of an existing study. As regards the final model parameter, namely the Michaelis Menten constant K_M of Equation 3.5 is found to be very close to the literature value of 0.5. Hence, the assumption of using the K_M value provided by the reference study to conduct the parametric runs is observed to be a valid method.

Table 14: Optimum values obtained from optimization model 2 vs. the best values obtained based on the parametric study presented in Chapter 4.2.

Parameter	**Best Parameter Set from Parametric Study**	**Optimum Values Found**
r_G (1/s)	2×10^{-5}	2.48×10^{-5}
d_G (1/s)	1×10^{-8}	6×10^{-8}
K_M (-)	0.5	0.53

Table 15: Comparison of GF concentration results obtained using optimized design parameter values vs. reference study results over 28-day period.

	Reference Study Results	**Our Results**
Gp1	0	0
Gp7	0.5	0.59
Gp14	0.7	0.72
Gp21	0.8	0.76
Gp28	0.7	0.77
Gs1	0	0
Gs7	0.9	0.75
Gs14	0.9	0.78
Gs21	1	0.79
Gs28	1	0.81

Finally, the GF concentration values at the selected reference data point obtained from optimization model 2 are compared with the reference study results for BMP-2 concentration both in pores and scaffold domains and the results are shown in Table 15.

The difference in later days in both domains are intuitively expected as the parametric study results are based on a model with an initial loaded BMP-2 amount of 0.8, hence the saturation to a maximum value of 0.8 in each domain in the case of complete release. However, although the reference study is based on the same amount of initial loading (determined based on their concentration profile results), GF concentration somehow increased to the values larger than its initial loaded concentration values, namely to 1, in the reference study. Other than that, the change of the GF concentration values had the same exact trend in the pores and a similar trend in the scaffold converging to the respective maximum values over the same time period. Overall, both similar to optimization model 1, optimization model 2 presents the working ability of the optimization model to locate improved design solutions matching desired GF concentrations at an acceptable level. Further improvements could be achieved with increased number of design variables such as the size of the scaffold, the combination of all affecting PDE coefficients and additional desired metrics such as the combination of both optimization models as well as integration of desired concentration distributions in the future.

CHAPTER 5

5. CONCLUSIONS AND FUTURE WORK

5.1.Conclusions

This thesis provides an in-depth examination of the degradation of a 3D porous polymeric bone tissue scaffold, aiming to enhance bone healing through the release of growth factors. The study utilized COMSOL Multiphysics software, which employs the finite element method (FEM), to solve a set of time-dependent reaction-diffusion equations. In the first part of the thesis, a parametric study was conducted using the developed FEM model, focusing primarily on scaffold degradation rate and the release and degradation rates of BMP-2. These parameters were fine-tuned based on existing computational models and experimental data available in the literature. Prior to the construction of the 3D scaffold model, an initial validation was performed using a simpler geometry. A 2D axisymmetrical non-porous spherical scaffold degradation was analyzed and the results were found to be consistent with the reference study selected (Rothstein et al., 2009). Moving on to the model development for a 3D scaffold geometry, we had to deal with the lack of certain parameter data and tried to solve this problem by performing a detailed parametric study. The literature is not very rich in terms of parametric analysis of degrading and growth factor release incorporating studies. It is known that degradation rate of scaffold and water diffusivity are the most important parameters for tailoring polymer concentration and our study proves this effect while providing a tunable range for these parameters. Similarly, results showed that degradation rate of BMP-2 and its release constant are the most effective parameters on the resulting BMP-2 concentration profiles. Also, the dominancy of diffusion coefficient of BMP-2 is not as effective as the former two parameters on the initial and final released BMP-2 concentration, however it enables us to tune the BMP-2 concentration at the intermediate time steps in possible design studies.

Additionally, a signaling pathway induced by the released BMP-2 was modeled by deriving a set of ordinary differential equations (ODEs) based on the mass action law. This system of ODEs was then analyzed using the Michaelis-Menten approach incorporating Hill functions, with a mathematical derivation for which the details were also provided. We concluded that transcription factor dynamics are extremely dependent on BMP-2 release dynamics while a steady state cannot be reached before sustaining the BMP-2 concentration.

Finally, two optimization models were developed to determine optimal values for the parameters governing scaffold degradation and growth factor release kinetics in an initial FEA based model. The objective functions for these optimization models were defined as the minimization of the squared differences between desired and actual polymer and growth factor concentrations over the considered time frame of the reference study (X. Sun et al., 2013). For the scaffold degradation, design variables included water diffusivity and hydrolysis rate constant, while for growth factor release, the variables included degradation and release rates, as well as the Michaelis-Menten constant. These algorithms successfully identified optimal values for each variable, ensuring acceptable consistency with both the literature and the outcomes of the earlier parametric study. The optimization models show that our parametric analysis was consistent in terms of reaching a similar reference polymer and BMP-2 concentration. Also, we can conclude that an optimization algorithm is useful to shorten iterative steps in mathematical approaches while parametric study is still necessary to determine the appropriate constraints and bounds as well as the more important parameters in performance tuning.

5.2.Future Work

Future work on this thesis may involve several key enhancements and integrations to advance the current research. First, scaffold degradation may be modeled using a level set method to more accurately capture the dynamic changes in scaffold geometry over time. Assigning a surface movement velocity defined by a level set method can model release dynamics better since the scaffold geometry will change below a certain threshold defined for polymer concentration. Additionally, the incorporation of cellular activities on growth factor dynamics will provide a more comprehensive understanding of their impact on bone healing. The depletion rate of growth factor due to the osteoblast/osteoclast activities, mesenchymal stem proliferation, and differentiation may be considered for their effect of growth factor dynamics.

Furthermore, the developed model may be integrated to key mechanisms such as angiogenesis, tissue regeneration, and mechanical response simulations. This integrated holistic approach should enable a more complete assessment of the scaffold's performance and its interaction with the biological environment. The optimization study can also be extended to this integrated model, allowing it to run for different scenarios and requirements, thereby identifying optimal parameters that satisfy multiple design criteria simultaneously.

For the signaling pathway model, additional pathways not considered in this thesis may be included. In addition to considering BMP-2, TGF-β, Wnt for osteogenesis, VEGF could be incorporated into a possible angiogenesis modeling in the future within a more comprehensive bone regeneration model. The addition of various growth factors will highly increase the complexity of the mathematical model due to their downregulatory pathways and crosstalk between their signaling cascades. However, their inclusion should provide a more detailed representation of the cellular signaling mechanisms involved in bone regeneration. As a final improvement, the signaling pathway model could be solved as a time-dependent system to capture the dynamic interactions and changes over the healing period.

By incorporating these enhancements, future work will significantly advance the current research, providing a more accurate model which can represent additional regenerative events stimulated by bone tissue engineering scaffolds, and offering valuable insights into the optimization of scaffold design and functionality for improved clinical outcomes.

REFERENCES

Abbasi, N., Hamlet, S., Love, R. M., & Nguyen, N. T. (2020). Porous scaffolds for bone regeneration. In *Journal of Science: Advanced Materials and Devices* (Vol. 5, Issue 1, pp. 1–9). Elsevier B.V. https://doi.org/10.1016/j.jsamd.2020.01.007

Adachi, T., Osako, Y., Tanaka, M., Hojo, M., & Hollister, S. J. (2006). Framework for optimal design of porous scaffold microstructure by computational simulation of bone regeneration. *Biomaterials*, *27*(21), 3964–3972. https://doi.org/10.1016/j.biomaterials.2006.02.039

Aldridge, B. B., Burke, J. M., Lauffenburger, D. A., & Sorger, P. K. (2006). Physicochemical modelling of cell signalling pathways. In *NATURE CELL BIOLOGY* (Vol. 8, Issue 11).

Anbumathi, P. (2014). Chemical kinetics based modelling approaches and tools for investigating complex biological systems. In *Asian Journal of Chemistry* (Vol. 26, Issue 9, pp. 2511–2517). Chemical Publishing Co. https://doi.org/10.14233/ajchem.2014.15756

Ang, J., Harris, E., Hussey, B. J., Kil, R., & McMillen, D. R. (2013). Tuning response curves for synthetic biology. In *ACS Synthetic Biology* (Vol. 2, Issue 10, pp. 547–567). American Chemical Society. https://doi.org/10.1021/sb4000564

Ansari, M. (2019). Bone tissue regeneration: biology, strategies and interface studies. In *Progress in Biomaterials* (Vol. 8, Issue 4, pp. 223–237). Springer Science and Business Media Deutschland GmbH. https://doi.org/10.1007/s40204-019-00125-z

Arifin, D. Y., Lee, L. Y., & Wang, C. H. (2006). Mathematical modeling and simulation of drug release from microspheres: Implications to drug delivery systems. In *Advanced Drug Delivery Reviews* (Vol. 58, Issues 12–13, pp. 1274–1325). https://doi.org/10.1016/j.addr.2006.09.007

Artel, A., Mehdizadeh, H., Chiu, Y. C., Brey, E. M., & Cinar, A. (2011). An agent-based model for the investigation of neovascularization within porous scaffolds. *Tissue Engineering - Part A*, *17*(17–18), 2133–2141. https://doi.org/10.1089/ten.tea.2010.0571

Askarizadeh, M., Esfandiari, N., Honarvar, B., Sajadian, S. A., & Azdarpour, A. (2023). Kinetic Modeling to Explain the Release of Medicine from Drug

Delivery Systems. In *ChemBioEng Reviews* (Vol. 10, Issue 6, pp. 1006–1049). John Wiley and Sons Inc. https://doi.org/10.1002/cben.202300027

Bakhshayesh, A. R. D. N., Khalilov, R., Akbarzadeh, A., Samiei, M., Alizadeh, E., Alizadeh-Ghodsi, M., Davaran, S., & Montaseri, A. (2018). Recent advances on biomedical applications of scaffolds in wound healing and dermal tissue engineering. In *Artificial Cells, Nanomedicine and Biotechnology* (Vol. 46, Issue 4, pp. 691–705). Taylor and Francis Ltd. https://doi.org/10.1080/21691401.2017.1349778

Bazyar, P., & Sheidaee, E. (2024). Design and simulating lattice structures in the FE analysis of the femur bone. In *Bioprinting* (Vol. 37). Elsevier B.V. https://doi.org/10.1016/j.bprint.2023.e00326

Bing, L. (2005). *Honours Year Project Report Computational Modeling of Biological Pathways*.

Blackwood, K. A., Bock, N., Dargaville, T. R., & Ann Woodruff, M. (2012). Scaffolds for growth factor delivery as applied to bone tissue engineering. In *International Journal of Polymer Science* (Vol. 2012). Hindawi Limited. https://doi.org/10.1155/2012/174942

Calori, I. R., Braga, G., de Jesus, P. da C. C., Bi, H., & Tedesco, A. C. (2020). Polymer scaffolds as drug delivery systems. In *European Polymer Journal* (Vol. 129). Elsevier Ltd. https://doi.org/10.1016/j.eurpolymj.2020.109621

Camal Ruggieri, I. N., & Feldman, S. (2020). Signaling pathways of nucleic acids for bone healing: A review. *Pharmacy & Pharmacology International Journal*, *8*(5), 291–295. https://doi.org/10.15406/ppij.2020.08.00308

Caplan. (2001). *caplan2001*.

Celil, A. B., Hollinger, J. O., & Campbell, P. G. (2005). Osx transcriptional regulation is mediated by additional pathways to BMP2/Smad signaling. *Journal of Cellular Biochemistry*, *95*(3), 518–528. https://doi.org/10.1002/jcb.20429

Chen, G., Deng, C., & Li, Y. P. (2012). TGF-β and BMP signaling in osteoblast differentiation and bone formation. In *International Journal of Biological Sciences* (Vol. 8, Issue 2, pp. 272–288). https://doi.org/10.7150/ijbs.2929

Chen, Y., Zhou, S., & Li, Q. (2011). Mathematical modeling of degradation for bulk-erosive polymers: Applications in tissue engineering scaffolds and drug delivery systems. *Acta Biomaterialia*, *7*(3), 1140–1149. https://doi.org/10.1016/j.actbio.2010.09.038

Chung, Y. Il, Ahn, K. M., Jeon, S. H., Lee, S. Y., Lee, J. H., & Tae, G. (2007). Enhanced bone regeneration with BMP-2 loaded functional nanoparticle-hydrogel complex. *Journal of Controlled Release*, *121*(1–2), 91–99. https://doi.org/10.1016/j.jconrel.2007.05.029

Clarke, B. (2008). Normal bone anatomy and physiology. In *Clinical journal of the American Society of Nephrology : CJASN: Vol. 3 Suppl 3*. https://doi.org/10.2215/CJN.04151206

Clarke, D. C. (2000). *THE QUANTITATIVE ANALYSIS OF TGF-β/SMAD SIGNALING DYNAMICS*.

Clarke, D. C., Betterton, M. D., & Liu, X. (2006). Systems theory of Smad signalling. *IEE Proceedings: Systems Biology*, *153*(6), 412–424. https://doi.org/10.1049/ip-syb:20050055

COMSOL. (2022). *User´s Guide Comsol Multiphysics* ®. www.comsol.com/support/knowledgebase

Crampin, E. J., Schnell, S., & McSharry, P. E. (2004). Mathematical and computational techniques to deduce complex biochemical reaction mechanisms. *Progress in Biophysics and Molecular Biology*, *86*(1), 77–112. https://doi.org/10.1016/j.pbiomolbio.2004.04.002

Davis, H. E., & Leach, J. K. (2011). Designing bioactive delivery systems for tissue regeneration. *Annals of Biomedical Engineering*, *39*(1), 1–13. https://doi.org/10.1007/s10439-010-0135-y

Davison, N. L., Barrère-de Groot, F., & Grijpma, D. W. (2014). Degradation of Biomaterials. In *Tissue Engineering: Second Edition* (pp. 177–215). Elsevier Inc. https://doi.org/10.1016/B978-0-12-420145-3.00006-7

De Witte, T. M., Fratila-Apachitei, L. E., Zadpoor, A. A., & Peppas, N. A. (2018). Bone tissue engineering via growth factor delivery: From scaffolds to complex matrices. *Regenerative Biomaterials*, *5*(4), 197–211. https://doi.org/10.1093/rb/rby013

dos Santos, V., Brandalise, R. N., & Savaris, M. (2017). Biomaterials: Characteristics and Properties. In *Topics in Mining, Metallurgy and Materials Engineering* (pp. 5–15). Springer Science and Business Media Deutschland GmbH. https://doi.org/10.1007/978-3-319-58607-6_2

Eilertsen, J., Roussel, M. R., Schnell, S., & Walcher, S. (2021). *On the quasi-steady-state approximation in an open Michaelis--Menten reaction mechanism*. https://doi.org/10.3934/math.2021398

Eilertsen, J., & Schnell, S. (2020). The quasi-steady-state approximations revisited: Timescales, small parameters, singularities, and normal forms in enzyme kinetics. *Mathematical Biosciences*, *325*. https://doi.org/10.1016/j.mbs.2020.108339

Einhorn, T. A., & Gerstenfeld, L. C. (2015). Fracture healing: Mechanisms and interventions. In *Nature Reviews Rheumatology* (Vol. 11, Issue 1, pp. 45–54). Nature Publishing Group. https://doi.org/10.1038/nrrheum.2014.164

Farzan, M., Roth, R., Schoelkopf, J., Huwyler, J., & Puchkov, M. (2023). The processes behind drug loading and release in porous drug delivery systems. In *European Journal of Pharmaceutics and Biopharmaceutics* (Vol. 189, pp. 133–151). Elsevier B.V. https://doi.org/10.1016/j.ejpb.2023.05.019

Ferraz, M. P. (2024). An Overview on the Big Players in Bone Tissue Engineering: Biomaterials, Scaffolds and Cells. In *International Journal of Molecular Sciences* (Vol. 25, Issue 7). Multidisciplinary Digital Publishing Institute (MDPI). https://doi.org/10.3390/ijms25073836

Fletcher, A. G., & Osborne, J. M. (2022). Seven challenges in the multiscale modeling of multicellular tissues. In *WIREs Mechanisms of Disease* (Vol. 14, Issue 1). John Wiley and Sons Inc. https://doi.org/10.1002/wsbm.1527

Fratzl, P., & Weinkamer, R. (2007). Nature's hierarchical materials. In *Progress in Materials Science* (Vol. 52, Issue 8, pp. 1263–1334). https://doi.org/10.1016/j.pmatsci.2007.06.001

Garzón-Alvarado, D. A., Velasco, M. A., & Narváez-Tovar, C. A. (2012). Modeling porous scaffold microstructure by a reaction-diffusion system and its degradation by hydrolysis. *Computers in Biology and Medicine*, *42*(2), 147–155. https://doi.org/10.1016/j.compbiomed.2011.11.002

Ghosh, P. K., Boruah, N., & Sharma, H. K. (2018). Brain and bone delivery of drugs: a review on various techniques of drug delivery. *Egyptian Pharmaceutical Journal*, *17*, 141–149. https://doi.org/10.4103/epj.epj_21_18

Göpferich, A. (1996). Mechanisms of polymer degradation and erosion1. In *The Biomaterials: Silver Jubilee Compendium* (pp. 117–128). Elsevier Ltd. https://doi.org/10.1016/B978-008045154-1.50016-2

Gopferich, A., & Langer, R. (1993). Modeling of Polymer Erosiont. In *Macromolecules* (Vol. 26). https://pubs.acs.org/sharingguidelines

Hayrapetyan, A., Jansen, J. A., & Van Den Beucken, J. J. J. P. (2015). Signaling pathways involved in osteogenesis and their application for bone regenerative medicine. *Tissue Engineering - Part B: Reviews*, *21*(1), 75–87. https://doi.org/10.1089/ten.teb.2014.0119

Hettiaratchi, M. H., & Coulter, W. H. (2016). *HEPARIN MICROPARTICLE-MEDIATED DELIVERY OF BMP-2 AND PLURIPOTENT STEM CELL MORPHOGENS FOR BONE REPAIR in the*.

Hollister, S. J. (2005). *Porous scaffold design for tissue engineering*. www.nature.com/naturematerials

Hollister, S. J., Maddox, R. D., & Taboas, J. M. (2002). Optimal design and fabrication of scaffolds to mimic tissue properties and satisfy biological constraints. In *Biomaterials* (Vol. 23).

Huang, D., Hou, X., Zhang, D., Zhang, Q., & Yan, C. (2020). Two novel polysaccharides from rhizomes of Cibotium barometz promote bone formation via activating the BMP2/SMAD1 signaling pathway in MC3T3-E1 cells. *Carbohydrate Polymers*, *231*. https://doi.org/10.1016/j.carbpol.2019.115732

Huang, G. X., Arany, P. R., & Mooney, D. J. (2015). Modeling and Validation of Multilayer Poly(Lactide-Co-Glycolide) Scaffolds for in Vitro Directed Differentiation of Juxtaposed Cartilage and Bone. *Tissue Engineering - Part A*, *21*(15–16), 2228–2240. https://doi.org/10.1089/ten.tea.2015.0089

Huang, X., & Brazel, C. S. (2001). On the importance and mechanisms of burst release in matrix-controlled drug delivery systems. In *Journal of Controlled Release* (Vol. 73). www.elsevier.com/locate/jconrel

Huang, Z., Nelson, E. R., Smith, R. L., & Goodman, S. B. (2007). The sequential expression profiles of growth factors from osteroprogenitors to osteoblasts in vitro. *Tissue Engineering*, *13*(9), 2311–2320. https://doi.org/10.1089/ten.2006.0423

Hussein, K. H., Park, K. M., Kang, K. S., & Woo, H. M. (2016). Biocompatibility evaluation of tissue-engineered decellularized scaffolds for biomedical application. In *Materials Science and Engineering C* (Vol. 67, pp. 766–778). Elsevier Ltd. https://doi.org/10.1016/j.msec.2016.05.068

Ideker, T., Galitski, T., & Hood, L. (2001). *A NEW APPROACH TO DECODING LIFE: Systems Biology*. www.annualreviews.org

Inman, G. J., Nicolá, F. J., & Hill, C. S. (2002). Nucleocytoplasmic Shuttling of Smads 2, 3, and 4 Permits Sensing of TGF-Receptor Activity The R-Smads appear to be retained in the cytoplasm in. In *Molecular Cell* (Vol. 10). http://www.molecule.

Kahlem, P., & Birney, E. (2006). Dry work in a wet world: Computation in systems biology. In *Molecular Systems Biology* (Vol. 2). Nature Publishing Group. https://doi.org/10.1038/msb4100080

Kang, H. S. (2010). *Hierarchical Design and Simulation of Tissue Engineering Scaffold Mechanical, Mass Transport, and Degradation Properties*.

Kang, H.-W., KhudaBukhsh, W. R., Koeppl, H., & Rempała, G. A. (2017). *Quasi-steady-state approximations derived from the stochastic model of enzyme kinetics*. http://arxiv.org/abs/1711.02791

Karlebach, G., & Shamir, R. (2008). Modelling and analysis of gene regulatory networks. In *Nature Reviews Molecular Cell Biology* (Vol. 9, Issue 10, pp. 770–780). https://doi.org/10.1038/nrm2503

Khotib, J., Gani, M. A., Budiatin, A. S., Lestari, M. L. A. D., Rahadiansyah, E., & Ardianto, C. (2021). Signaling pathway and transcriptional regulation in osteoblasts during bone healing: Direct involvement of hydroxyapatite as a biomaterial. In *Pharmaceuticals* (Vol. 14, Issue 7). MDPI AG. https://doi.org/10.3390/ph14070615

Kim, J. N., Lee, J. Y., Shin, K. J., Gil, Y. C., Koh, K. S., & Song, W. C. (2015). Haversian system of compact bone and comparison between endosteal and periostealsides using three-dimensional reconstructionin rat. *Anatomy and Cell Biology*, *48*(4), 258–261. https://doi.org/10.5115/acb.2015.48.4.258

Kitano, H. (2002). *Systems Biology: A Brief Overview*. http://www.stke.org/

Klipp, E., Liebermeister, W., Wierling, C., & Kowald, A. (2016). *Systems Biology*.

Komori, T. (2005). Regulation of skeletal development by the Runx family of transcription factors. In *Journal of Cellular Biochemistry* (Vol. 95, Issue 3, pp. 445–453). https://doi.org/10.1002/jcb.20420

Komori, T. (2022). Whole Aspect of Runx2 Functions in Skeletal Development. In *International Journal of Molecular Sciences* (Vol. 23, Issue 10). MDPI. https://doi.org/10.3390/ijms23105776

Kopf, J., Petersen, A., Duda, G. N., & Knaus, P. (2012). BMP2 and mechanical loading cooperatively regulate immediate early signalling events in the BMP pathway. *BMC Biology*, *10*. https://doi.org/10.1186/1741-7007-10-37

Kuttappan, S., Mathew, D., Jo, J. ichiro, Tanaka, R., Menon, D., Ishimoto, T., Nakano, T., Nair, S. V., Nair, M. B., & Tabata, Y. (2018). Dual release of growth factor from nanocomposite fibrous scaffold promotes vascularisation and bone regeneration in rat critical sized calvarial defect. *Acta Biomaterialia*, *78*, 36–47. https://doi.org/10.1016/j.actbio.2018.07.050

Lang, A., Benn, A., Collins, J. M., Wolter, A., Balcaen, T., Kerckhofs, G., Zwijsen, A., & Boerckel, J. D. (2024). Endothelial SMAD1/5 signaling couples angiogenesis to osteogenesis in juvenile bone. *Communications Biology*, *7*(1). https://doi.org/10.1038/s42003-024-05915-1

Lanza, R. (2014). *Principles of Tissue Engineering*.

Le Novere, N. (2015). Quantitative and logic modelling of molecular and gene networks. In *Nature Reviews Genetics* (Vol. 16, Issue 3, pp. 146–158). Nature Publishing Group. https://doi.org/10.1038/nrg3885

Lee, K.-S., Hong, S.-H., & Bae, S.-C. (2002). Both the Smad and p38 MAPK pathways play a crucial role in Runx2 expression following induction by transforming growth factor-b and bone morphogenetic protein. *Oncogene*, *21*, 7156–7163. https://doi.org/10.1038/sj.onc

Lee, K.-S., Kim, H.-J., Li, Q.-L., Chi, X.-Z., Ueta, C., Komori, T., Wozney, J. M., Kim, E.-G., Choi, J.-Y., Ryoo, H.-M., & Bae, S.-C. (2000). *Runx2 Is a Common Target of Transforming Growth Factor 1 and Bone Morphogenetic Protein 2, and Cooperation between Runx2 and Smad5 Induces Osteoblast-Specific Gene Expression in the Pluripotent Mesenchymal Precursor Cell Line C2C12* (Vol. 20, Issue 23).

Leong, K. W., & Langer, R. (1987). Polymeric controlled drug delivery. In *Advanced Drug Dehvery Revtews* (Vol. 1).

Li, Y., Liao, C., & Tjong, S. C. (2019). Synthetic biodegradable aliphatic polyester nanocomposites reinforced with nanohydroxyapatite and/or graphene oxide for bone tissue engineering applications. *Nanomaterials*, *9*(4). https://doi.org/10.3390/nano9040590

Liebschner, M. A. K., & Wettergreen, M. A. (2003). *Chapter 6 II Bone*.

Lienemann, P. S., Lutolf, M. P., & Ehrbar, M. (2012). Biomimetic hydrogels for controlled biomolecule delivery to augment bone regeneration. In *Advanced Drug Delivery Reviews* (Vol. 64, Issue 12, pp. 1078–1089). https://doi.org/10.1016/j.addr.2012.03.010

Liu, J., Roque, R., Barbosa, G. F., & Malavolta, A. T. (2021). Compression stiffness evaluation of polycaprolactone-amorphous calcium phosphate 3D-designed scaffolds oriented by finite element analysis. *Journal of Applied Polymer Science*, *138*(42). https://doi.org/10.1002/app.51245

Mac Gabhann, F., Yang, M. T., & Popel, A. S. (2005). Monte Carlo simulations of VEGF binding to cell surface receptors in vitro. *Biochimica et Biophysica Acta - Molecular Cell Research*, *1746*(2), 95–107. https://doi.org/10.1016/j.bbamcr.2005.09.004

Maes, C., & Kronenberg, H. M. (2011). Postnatal Bone Growth: Growth Plate Biology, Bone Formation, and Remodeling. In *Pediatric Bone: Biology and Diseases* (pp. 55–82). Elsevier. https://doi.org/10.1016/B978-0-12-382040-2.10004-8

Majidinia, M., Sadeghpour, A., & Yousefi, B. (2018). The roles of signaling pathways in bone repair and regeneration. In *Journal of Cellular Physiology* (Vol. 233, Issue 4, pp. 2937–2948). Wiley-Liss Inc. https://doi.org/10.1002/jcp.26042

Manhas, V., Guyot, Y., Kerckhofs, G., Chin Chai, Y., & Geris, L. (2017). *Computational modelling of local calcium ions release from calcium phosphate-based scaffolds*.

Mark Saltzman, W. (2009). *BIOMEDICAL ENGINEERING: Bridging Medicine and Technology*.

Marsell, R., & Einhorn, T. A. (2011). The biology of fracture healing. *Injury*, *42*(6), 551–555. https://doi.org/10.1016/j.injury.2011.03.031

Massagué, J., Seoane, J., & Wotton, D. (2005). Smad transcription factors. In *Genes and Development* (Vol. 19, Issue 23, pp. 2783–2810). https://doi.org/10.1101/gad.1350705

Meyer, U., Meyer, T., Handschel, J., & Wiesmann, H. P. (2009). Fundamentals of tissue engineering and regenerative medicine. In *Fundamentals of Tissue Engineering and Regenerative Medicine*. Springer Berlin Heidelberg. https://doi.org/10.1007/978-3-540-77755-7

Min Lee, J., Gianchandani, E. P., Eddy, J. A., & Papin, J. A. (2008). Dynamic analysis of integrated signaling, metabolic, and regulatory networks. *PLoS Computational Biology*, *4*(5). https://doi.org/10.1371/journal.pcbi.1000086

Mohseni-Motlagh, S. F., Dolatabadi, R., Baniassadi, M., Karimpour, M., & Baghani, M. (2023). Tablet Geometry Effect on the Drug Release Profile from a Hydrogel-Based Drug Delivery System. *Pharmaceutics*, *15*(7). https://doi.org/10.3390/pharmaceutics15071917

N. Musthafa, H. S., Walker, J., & Domagala, M. (2024). Computational Modelling and Simulation of Scaffolds for Bone Tissue Engineering. In *Computation* (Vol. 12, Issue 4). Multidisciplinary Digital Publishing Institute (MDPI). https://doi.org/10.3390/computation12040074

Nasir, N. J. N., Arifin, N., Noordin, K. B. A. A., & Yusop, N. (2023). Bone repair and key signalling pathways for cell-based bone regenerative therapy: A review. In *Journal of Taibah University Medical Sciences* (Vol. 18, Issue 6, pp. 1350–1363). Elsevier B.V. https://doi.org/10.1016/j.jtumed.2023.05.015

Oliveira, É. R., Nie, L., Podstawczyk, D., Allahbakhsh, A., Ratnayake, J., Brasil, D. L., & Shavandi, A. (2021). Advances in growth factor delivery for bone tissue engineering. In *International Journal of Molecular Sciences* (Vol. 22, Issue 2, pp. 1–33). MDPI AG. https://doi.org/10.3390/ijms22020903

Oliveira, S. R. P., Lima, G. G., Azevedo, M. M. F. de, Furtado, A. S. A., Gusmão, S. B. soares, Nascimento, E. da S., Bento, R. R. de F., Santo, F. E. P., Pinto, L. S. S., Stocco, T. D., Filho, A. M. M., Viana, B. C., Lobo, A. O., & Gusmão, G. O. de M. (2024). Controlled drug release from policaprolactone-piperine electrospun scaffold for bone tissue engineering. *Journal of Drug Delivery Science and Technology*, *91*. https://doi.org/10.1016/j.jddst.2023.105188

Oyane, A., Kim, H.-M., Furuya, T., Kokubo, T., Miyazaki, T., & Nakamura, T. (2003). *Preparation and assessment of revised simulated body fluids*.

Patel, Z. S., Young, S., Tabata, Y., Jansen, J. A., Wong, M. E. K., & Mikos, A. G. (2008). Dual delivery of an angiogenic and an osteogenic growth factor for bone regeneration in a critical size defect model. *Bone*, *43*(5), 931–940. https://doi.org/10.1016/j.bone.2008.06.019

Piñero, J., Furlong, L. I., & Sanz, F. (2018). In silico models in drug development: where we are. In *Current Opinion in Pharmacology* (Vol. 42, pp. 111–121). Elsevier Ltd. https://doi.org/10.1016/j.coph.2018.08.007

Raja, N., Han, S. H., Cho, M., Choi, Y. J., Jin, Y. Z., Park, H., Lee, J. H., & Yun, H. suk. (2022). Effect of porosity and phase composition in 3D printed calcium phosphate scaffolds on bone tissue regeneration in vivo. *Materials and Design*, *219*. https://doi.org/10.1016/j.matdes.2022.110819

Rama, M., & Vijayalakshmi, U. (2023). Drug delivery system in bone biology: an evolving platform for bone regeneration and bone infection management. In *Polymer Bulletin* (Vol. 80, Issue 7, pp. 7341–7388). Springer Science and Business Media Deutschland GmbH. https://doi.org/10.1007/s00289-022-04442-5

Ratner, B. D., Hoffman Allan S., Schoen Frederick J., & Lemons Jack E. (2013). *Biomaterials Science: An Introduction to Materials in Medicine* (3rd ed.). Elsevier Science & Technology.

Ribeiro, F. O., Gómez-Benito, M. J., Folgado, J., Fernandes, P. R., & García-Aznar, J. M. (2015). In silico mechano-chemical model of bone healing for the regeneration of critical defects: The effect of BMP-2. *PLoS ONE*, *10*(6). https://doi.org/10.1371/journal.pone.0127722

Rodríguez-Montaño, Ó. L., Cortés-Rodríguez, C. J., Naddeo, F., Uva, A. E., Fiorentino, M., Naddeo, A., Cappetti, N., Gattullo, M., Monno, G., & Boccaccio, A. (2019). Irregular Load Adapted Scaffold Optimization: A Computational Framework Based on Mechanobiological Criteria. *ACS Biomaterials Science and Engineering*, *5*(10), 5392–5411. https://doi.org/10.1021/acsbiomaterials.9b01023

Rosen, V. (2009). BMP2 signaling in bone development and repair. In *Cytokine and Growth Factor Reviews* (Vol. 20, Issues 5–6, pp. 475–480). https://doi.org/10.1016/j.cytogfr.2009.10.018

Rothstein, S. N., Federspiel, W. J., & Little, S. R. (2009). A unified mathematical model for the prediction of controlled release from surface and bulk eroding polymer matrices. *Biomaterials*, *30*(8), 1657–1664. https://doi.org/10.1016/j.biomaterials.2008.12.002

Sanz-Herrera, J. A., García-Aznar, J. M., & Oblaré, M. D. (2009). A mathematical approach to bone Tissue engineering. *Philosophical Transactions of the Royal Society A: Mathematical, Physical and Engineering Sciences*, *367*(1895), 2055–2078. https://doi.org/10.1098/rsta.2009.0055

Schmierer, B., Tournier, A. L., Bates, P. A., & Hill, C. S. (2008). *Mathematical modeling identifies Smad nucleocytoplasmic shuttling as a dynamic signal-interpreting system*. www.pnas.org/cgi/content/full/

Schrade, S., Ritschl, L., Süss, R., Schilling, P., & Seidenstuecker, M. (2022). Gelatin Nanoparticles for Targeted Dual Drug Release out of Alginate-di-Aldehyde-Gelatin Gels. *Gels*, *8*(6). https://doi.org/10.3390/gels8060365

Segel, L. A., & Slemrod, M. (1989). *THE QUASI-STEADY-STATE ASSUMPTION: A CASE STUDY IN PERTURBATION* * (Vol. 31, Issue 3). http://www.siam.org/journals/ojsa.php

Sharma, S., Sudhakara, P., Singh, J., Ilyas, R. A., Asyraf, M. R. M., & Razman, M. R. (2021). Critical review of biodegradable and bioactive polymer composites for bone tissue engineering and drug delivery applications. In *Polymers* (Vol. 13, Issue 16). MDPI AG. https://doi.org/10.3390/polym13162623

Siepmann, J., Elkharraz, K., Siepmann, F., & Klose, D. (2005). How autocatalysis accelerates drug release from PLGA-based microparticles: A quantitative treatment. *Biomacromolecules*, *6*(4), 2312–2319. https://doi.org/10.1021/bm050228k

Siepmann, J., & Gopferich, A. (2001). Mathematical modeling of bioerodible, polymeric drug delivery systems. In *Advanced Drug Delivery Reviews* (Vol. 48). www.elsevier.com/locate/drugdeliv

Sobie, E. (2011). *The Need for a Systems Biology Course Systems biology focuses*. www.SCIENCESIGNALING.org

Song, B., Estrada, K. D., & Lyons, K. M. (2009). Smad signaling in skeletal development and regeneration. *Cytokine and Growth Factor Reviews*, *20*(5–6), 379–388. https://doi.org/10.1016/j.cytogfr.2009.10.010

Sorgente, T., Biasotti, S., Manzini, G., & Spagnuolo, M. (2023). A Survey of Indicators for Mesh Quality Assessment. *Computer Graphics Forum*, *42*(2), 461–483. https://doi.org/10.1111/cgf.14779

Suamte, L., Tirkey, A., Barman, J., & Jayasekhar Babu, P. (2023). Various manufacturing methods and ideal properties of scaffolds for tissue engineering applications. *Smart Materials in Manufacturing*, *1*, 100011. https://doi.org/10.1016/j.smmf.2022.100011

Sun, A. (2014). *UCLA UCLA Electronic Theses and Dissertations Title Modeling Bone Morphogenetic Protein Binding Peptide Action on Perfused Osteoblast Growth*. https://escholarship.org/uc/item/1hj680xf

Sun, X., Kang, Y., Bao, J., Zhang, Y., Yang, Y., & Zhou, X. (2013). Modeling vascularized bone regeneration within a porous biodegradable CaP scaffold loaded with growth factors. *Biomaterials*, *34*(21), 4971–4981. https://doi.org/10.1016/j.biomaterials.2013.03.015

Sun, X., Su, J., Bao, J., Peng, T., Zhang, L., Zhang, Y., Yang, Y., & Zhou, X. (2012). Cytokine combination therapy prediction for bone remodeling in tissue engineering based on the intracellular signaling pathway. *Biomaterials*, *33*(33), 8265–8276. https://doi.org/10.1016/j.biomaterials.2012.07.041

Tajvar, S., Hadjizadeh, A., & Samandari, S. S. (2023). Scaffold degradation in bone tissue engineering: An overview. In *International Biodeterioration and Biodegradation* (Vol. 180). Elsevier Ltd. https://doi.org/10.1016/j.ibiod.2023.105599

Takayama, T., Imamura, K., & Yamano, S. (2023). Growth Factor Delivery Using a Collagen Membrane for Bone Tissue Regeneration. In *Biomolecules* (Vol. 13, Issue 5). MDPI. https://doi.org/10.3390/biom13050809

Thakur, J. S., Thakur, A., & Lum, L. G. (2023). Mathematical Model to Predict Polyclonal T-Cell-Dependent Antibody Synthetic Responses. *Mathematics*, *11*(18). https://doi.org/10.3390/math11184017

Thaweesapphithak, S., Theerapanon, T., Rattanapornsompong, K., Intarak, N., Kanpittaya, P., Trachoo, V., Porntaveetus, T., & Shotelersuk, V. (2023). Functional consequences of C-terminal mutations in RUNX2. *Scientific Reports*, *13*(1). https://doi.org/10.1038/s41598-023-39293-1

Tohmonda, T., Miyauchi, Y., Ghosh, R., Yoda, M., Uchikawa, S., Takito, J., Morioka, H., Nakamura, M., Iwawaki, T., Chiba, K., Toyama, Y., Urano, F., & Horiuchi, K. (2011). The IRE1α-XBP1 pathway is essential for osteoblast differentiation through promoting transcription of Osterix. *EMBO Reports*, *12*(5), 451–457. https://doi.org/10.1038/embor.2011.34

Tu, X., Delgado-Calle, J., Condon, K. W., Maycas, M., Zhang, H., Carlesso, N., Taketo, M. M., Burr, D. B., Plotkin, L. I., & Bellido, T. (2015). Osteocytes mediate the anabolic actions of canonical Wnt/β-catenin signaling in bone.

Proceedings of the National Academy of Sciences of the United States of America, *112*(5), E478–E486. https://doi.org/10.1073/pnas.1409857112

Tzafriri, A. R. (2000). Mathematical modeling of diffusion-mediated release from bulk degrading matrices. In *Journal of Controlled Release* (Vol. 63). www.elsevier.com/locate/jconrel

Verardi, S., Swoboda, J., Rebaudi, F., & Rebaudi, A. (2018). Osteointegration of tissue-level implants with very low insertion torque in soft bone: A clinical study on SLA surface treatment. *Implant Dentistry*, *27*(1), 5–9. https://doi.org/10.1097/ID.0000000000000714

Von Burkersroda, F., Schedl, L., & Opferich, A. G. (2002). Why degradable polymers undergo surface erosion or bulk erosion. In *Biomaterials* (Vol. 23).

von Doernberg, M. C., von Rechenberg, B., Bohner, M., Grünenfelder, S., van Lenthe, G. H., Müller, R., Gasser, B., Mathys, R., Baroud, G., & Auer, J. (2006). In vivo behavior of calcium phosphate scaffolds with four different pore sizes. *Biomaterials*, *27*(30), 5186–5198. https://doi.org/10.1016/j.biomaterials.2006.05.051

Wang, L., Shi, Q., Cai, Y., Chen, Q., Guo, X., & Li, Z. (2020). Mechanical–chemical coupled modeling of bone regeneration within a biodegradable polymer scaffold loaded with VEGF. *Biomechanics and Modeling in Mechanobiology*, *19*(6), 2285–2306. https://doi.org/10.1007/s10237-020-01339-y

Wang, M., Jiang, G., Yang, H., & Jin, X. (2024). Computational models of bone fracture healing and applications: a review. In *Biomedizinische Technik* (Vol. 69, Issue 3, pp. 219–239). Walter de Gruyter GmbH. https://doi.org/10.1515/bmt-2023-0088

Wang, M., & Yang, N. (2017). A review of bioregulatory and coupled mechanobioregulatory mathematical models for secondary fracture healing. In *Medical Engineering and Physics* (Vol. 48, pp. 90–102). Elsevier Ltd. https://doi.org/10.1016/j.medengphy.2017.06.031

Wang, Q., Xiong, F., Wu, G., Wang, D., Liu, W., Chen, J., Qi, Y., Wang, B., & Chen, Y. (2023). SMAD Proteins in TGF-β Signalling Pathway in Cancer: Regulatory Mechanisms and Clinical Applications. In *Diagnostics* (Vol. 13, Issue 17). Multidisciplinary Digital Publishing Institute (MDPI). https://doi.org/10.3390/diagnostics13172769

Wang, R. S., Saadatpour, A., & Albert, R. (2012). Boolean modeling in systems biology: An overview of methodology and applications. In *Physical Biology* (Vol. 9, Issue 5). https://doi.org/10.1088/1478-3975/9/5/055001

Wang, Y., Pan, J., Han, X., Sinka, C., & Ding, L. (2008). A phenomenological model for the degradation of biodegradable polymers. *Biomaterials*, *29*(23), 3393–3401. https://doi.org/10.1016/j.biomaterials.2008.04.042

Wu, J., Zhang, Y., Lyu, Y., & Cheng, L. (2023). On the Various Numerical Techniques for the Optimization of Bone Scaffold. In *Materials* (Vol. 16, Issue 3). MDPI. https://doi.org/10.3390/ma16030974

Yang, D., Xiao, J., Wang, B., Li, L., Kong, X., & Liao, J. (2019). The immune reaction and degradation fate of scaffold in cartilage/bone tissue engineering. In *Materials Science and Engineering C* (Vol. 104). Elsevier Ltd. https://doi.org/10.1016/j.msec.2019.109927

Yang, Y., Zhao, Z., Qi, X., Hu, Y., Li, B., & Zhang, L. (2024). Computational Modeling of Bone Fracture Healing Under Different Initial Conditions and Mechanical Load. *IEEE Transactions on Biomedical Engineering*, *71*(7), 2105–2118. https://doi.org/10.1109/TBME.2024.3361893

Yin, S., Zhang, W., Zhang, Z., & Jiang, X. (2019). Recent Advances in Scaffold Design and Material for Vascularized Tissue-Engineered Bone Regeneration. In *Advanced Healthcare Materials* (Vol. 8, Issue 10). Wiley-VCH Verlag. https://doi.org/10.1002/adhm.201801433

Zamani, M., & Mohammadi, S. (2024). Finite element solution of coupled multiphysics reaction-diffusion equations for fracture healing in hard biological tissues. *Computers in Biology and Medicine*, *179*. https://doi.org/10.1016/j.compbiomed.2024.108829

Zhang, G., Liu, W., Wang, R., Zhang, Y., Chen, L., Chen, A., Luo, H., Zhong, H., & Shao, L. (2020). The role of tantalum nanoparticles in bone regeneration involves the BMP2/Smad4/Runx2 signaling pathway. *International Journal of Nanomedicine*, *15*, 2419–2435. https://doi.org/10.2147/IJN.S245174

Zhang, H., Zhou, L., & Zhang, W. (2014). Control of scaffold degradation in tissue engineering: A review. In *Tissue Engineering - Part B: Reviews* (Vol. 20, Issue 5, pp. 492–502). Mary Ann Liebert Inc. https://doi.org/10.1089/ten.teb.2013.0452

Zhang, Q., Jiang, Y., Zhang, Y., Ye, Z., Tan, W., & Lang, M. (2013). Effect of porosity on long-term degradation of poly (ε-caprolactone) scaffolds and their cellular response. *Polymer Degradation and Stability*, *98*(1), 209–218. https://doi.org/10.1016/j.polymdegradstab.2012.10.008

Zhang, S., Vijayavenkataraman, S., Lu, W. F., & Fuh, J. Y. H. (2019a). A review on the use of computational methods to characterize, design, and optimize tissue engineering scaffolds, with a potential in 3D printing fabrication. In *Journal of Biomedical Materials Research - Part B Applied Biomaterials* (Vol. 107, Issue 5, pp. 1329–1351). John Wiley and Sons Inc. https://doi.org/10.1002/jbm.b.34226

Zhang, S., Vijayavenkataraman, S., Lu, W. F., & Fuh, J. Y. H. (2019b). A review on the use of computational methods to characterize, design, and optimize tissue engineering scaffolds, with a potential in 3D printing fabrication. In *Journal of Biomedical Materials Research - Part B Applied Biomaterials* (Vol. 107, Issue 5, pp. 1329–1351). John Wiley and Sons Inc. https://doi.org/10.1002/jbm.b.34226

Zi, Z. (2012). A tutorial on mathematical modeling of biological signaling pathways. In *Methods in Molecular Biology* (Vol. 880, pp. 41–51). Humana Press Inc. https://doi.org/10.1007/978-1-61779-833-7_3

Zou, M. L., Chen, Z. H., Teng, Y. Y., Liu, S. Y., Jia, Y., Zhang, K. W., Sun, Z. L., Wu, J. J., Yuan, Z. D., Feng, Y., Li, X., Xu, R. S., & Yuan, F. L. (2021). The Smad Dependent TGF-β and BMP Signaling Pathway in Bone Remodeling and Therapies. In *Frontiers in Molecular Biosciences* (Vol. 8). Frontiers Media S.A. https://doi.org/10.3389/fmolb.2021.593310

APPENDICES

A. COMSOL MODEL SETTINGS FOR BACKGROUND VALIDATION OF 2D AXISYMMETRIC GEOMETRY OF ROTHSTEIN ET AL.

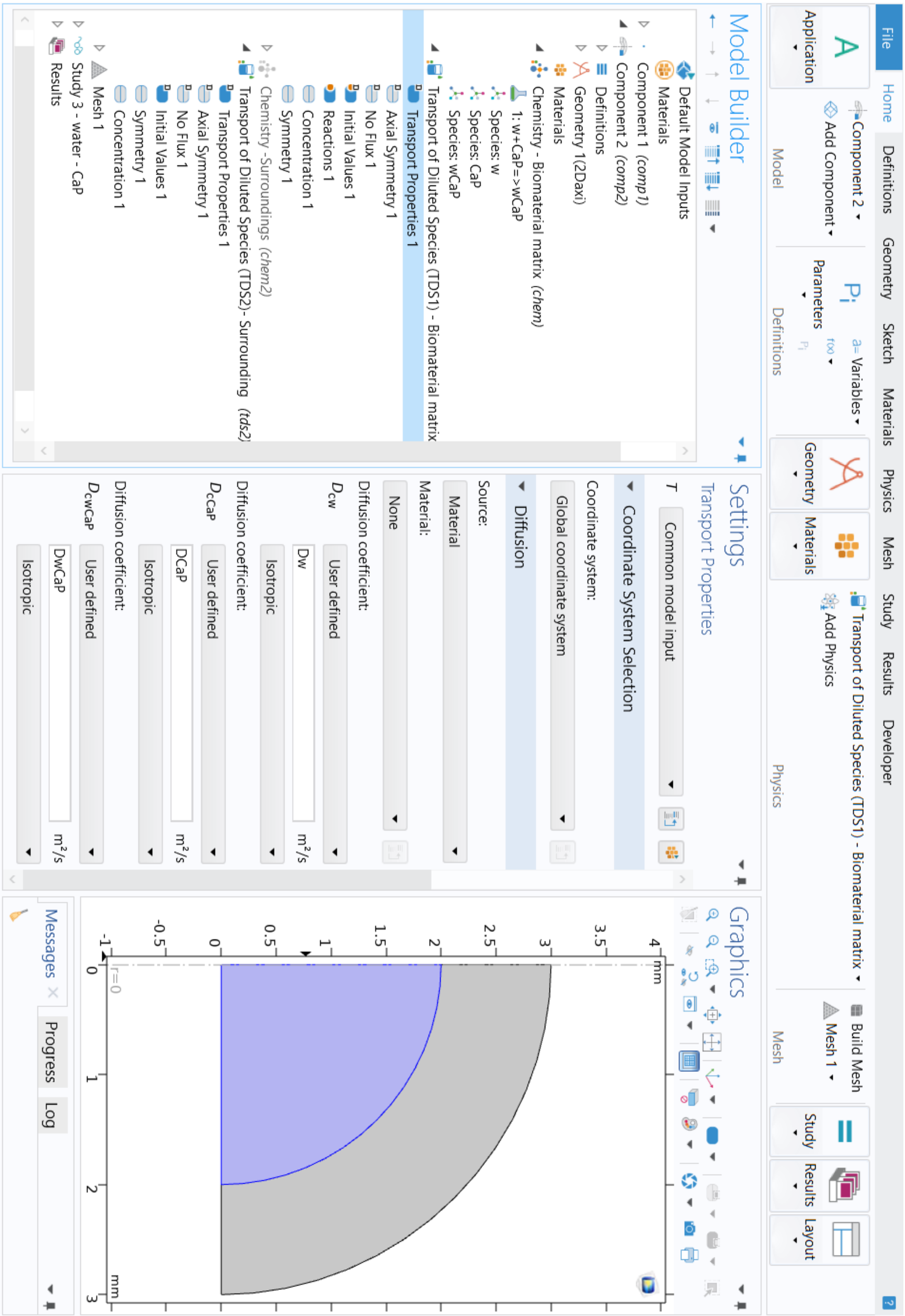

Model Builder

- Default Model Inputs
- Materials
- Component 1 *(comp1)*
- Component 2 *(comp2)*
  - Definitions
  - Geometry 1(2Daxi)
  - Materials
  - Chemistry - Biomaterial matrix *(chem)*
    - 1: w+CaP=>wCaP
    - Species: w
    - Species: CaP
    - Species: wCaP
  - Transport of Diluted Species (TDS1) - Biomaterial matrix
    - Transport Properties 1
    - Axial Symmetry 1
    - No Flux 1
    - Initial Values 1
    - Reactions 1
    - Concentration 1
    - Symmetry 1
  - Chemistry -Surroundings *(chem2)*
  - Transport of Diluted Species (TDS2)- Surrounding *(tds2)*
    - Transport Properties 1
    - Axial Symmetry 1
    - No Flux 1
    - Initial Values 1
    - Symmetry 1
    - Concentration 1
  - Mesh 1
- Study 3 - water - CaP
- Results

Settings
Transport Properties

T: Common model input

Coordinate System Selection

Coordinate system: Global coordinate system

Diffusion

Source: Material

Material: None

Diffusion coefficient: D_{cw} User defined, Dw m^2/s, Isotropic

Diffusion coefficient: D_{CaP} User defined, DCaP m^2/s, Isotropic

Diffusion coefficient: D_{cwCaP} User defined, DwCaP m^2/s, Isotropic

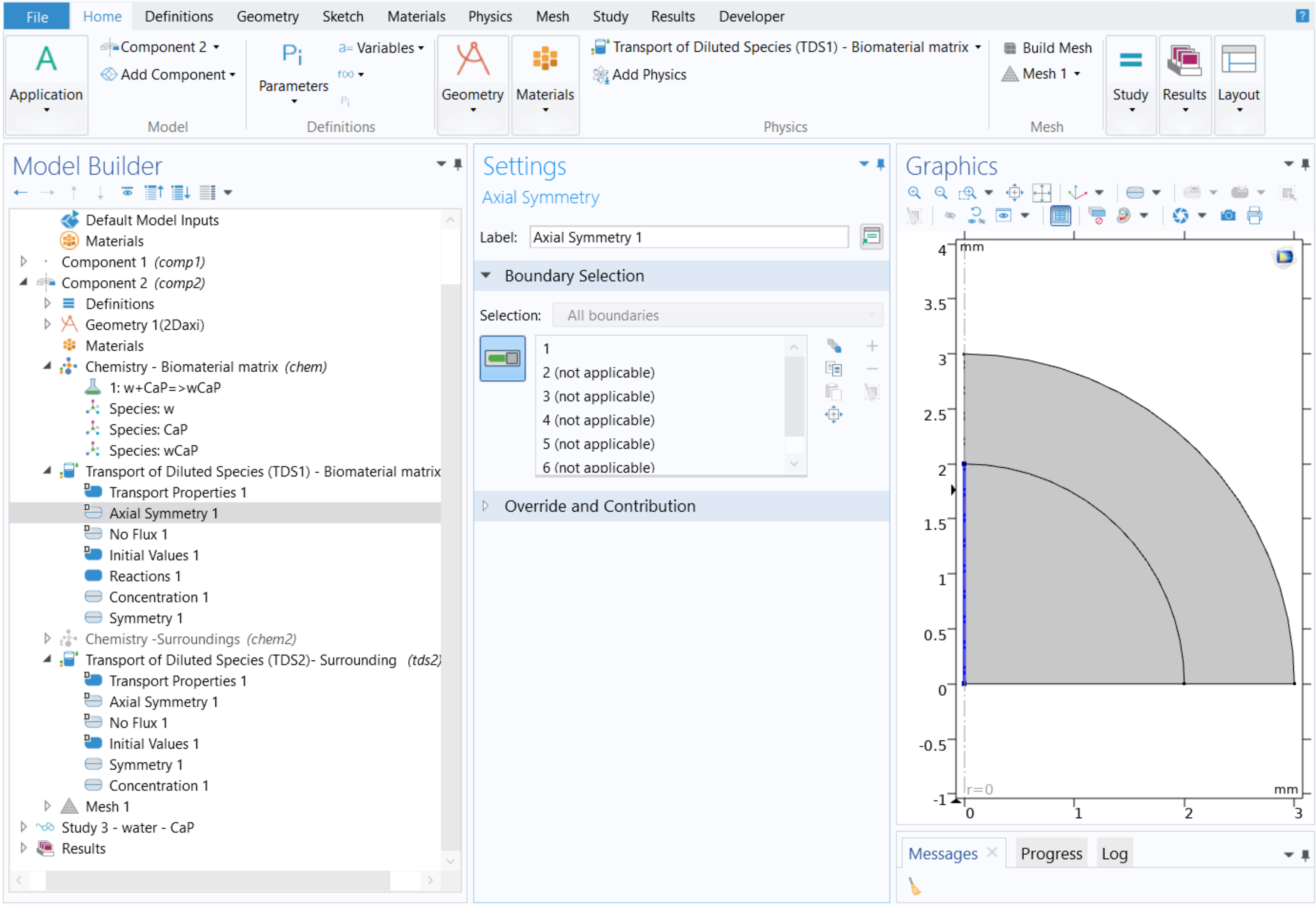

- Default Model Inputs
- Materials
- Component 1 *(comp1)*
- Component 2 *(comp2)*
  - Definitions
  - Geometry 1(2Daxi)
  - Materials
  - Chemistry - Biomaterial matrix *(chem)*
    - 1: w+CaP=>wCaP
    - Species: w
    - Species: CaP
    - Species: wCaP
  - Transport of Diluted Species (TDS1) - Biomaterial matrix
    - Transport Properties 1
    - Axial Symmetry 1
    - No Flux 1
    - Initial Values 1
    - Reactions 1
    - Concentration 1
    - Symmetry 1
  - Chemistry -Surroundings *(chem2)*
  - Transport of Diluted Species (TDS2)- Surrounding *(tds2)*
    - Transport Properties 1
    - Axial Symmetry 1
    - No Flux 1
    - Initial Values 1
    - Symmetry 1
    - Concentration 1
  - Mesh 1
- Study 3 - water - CaP
- Results

Settings

Axial Symmetry

Label: Axial Symmetry 1

Boundary Selection

Selection: All boundaries

1
2 (not applicable)
3 (not applicable)
4 (not applicable)
5 (not applicable)
6 (not applicable)

Override and Contribution

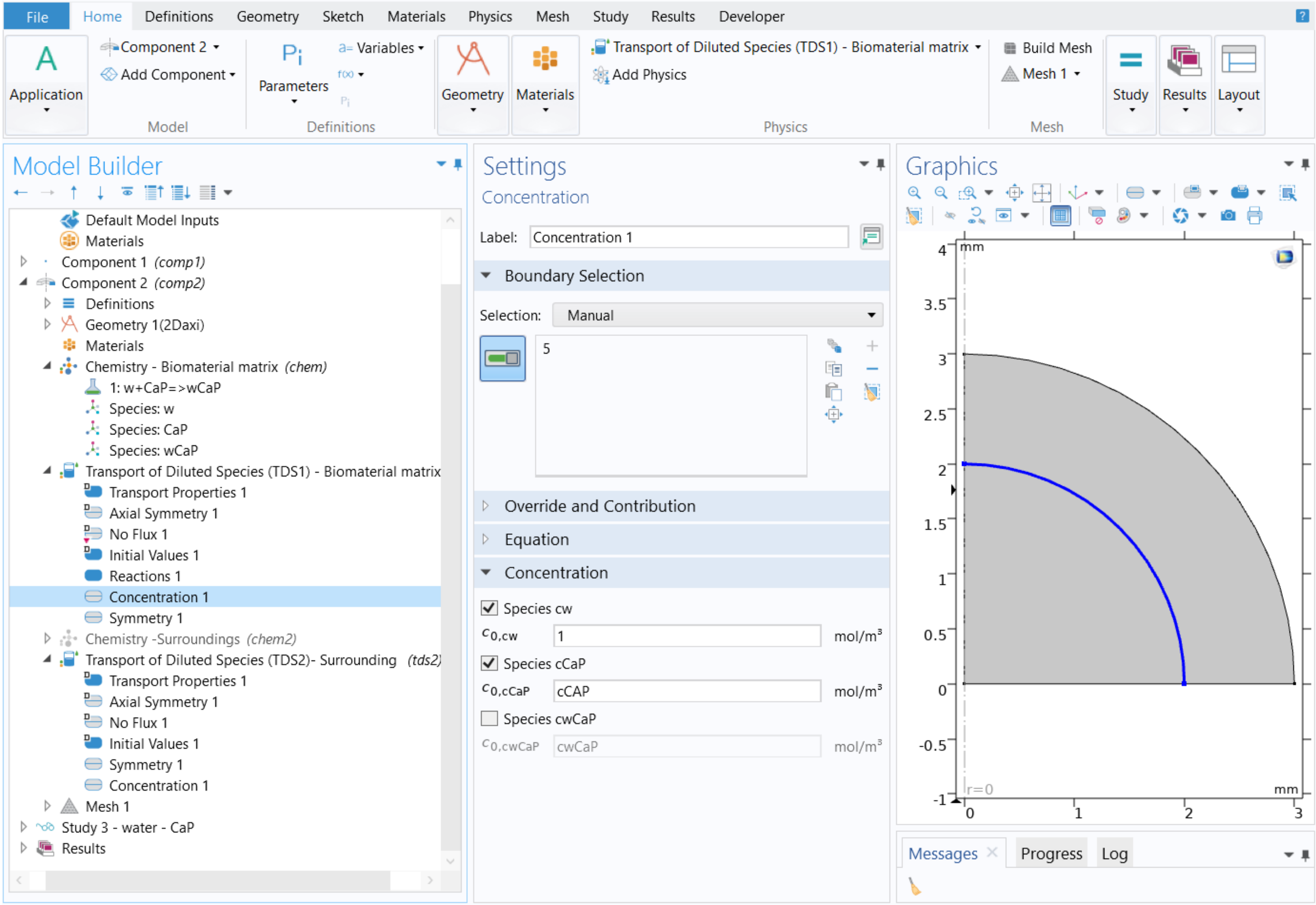

Model Builder

- Default Model Inputs
- Materials
- Component 1 *(comp1)*
- Component 2 *(comp2)*
  - Definitions
  - Geometry 1(2Daxi)
  - Materials
  - Chemistry - Biomaterial matrix *(chem)*
    - 1: w+CaP=>wCaP
    - Species: w
    - Species: CaP
    - Species: wCaP
  - Transport of Diluted Species (TDS1) - Biomaterial matrix
    - Transport Properties 1
    - Axial Symmetry 1
    - No Flux 1
    - Initial Values 1
    - Reactions 1
    - Concentration 1
    - Symmetry 1
  - Chemistry -Surroundings *(chem2)*
  - Transport of Diluted Species (TDS2)- Surrounding *(tds2)*
    - Transport Properties 1
    - Axial Symmetry 1
    - No Flux 1
    - Initial Values 1
    - Symmetry 1
    - Concentration 1
  - Mesh 1
- Study 3 - water - CaP
- Results

Settings

Concentration

Label: Concentration 1

Boundary Selection

Selection: Manual

5

Override and Contribution

Equation

Concentration

☑ Species cw

$c_{0,cw}$ 1 mol/m³

☑ Species cCaP

$c_{0,cCaP}$ cCAP mol/m³

☐ Species cwCaP

$c_{0,cwCaP}$ cwCaP mol/m³

B. COMSOL MODEL SETTINGS FOR INTEGRATED POLYMER DEGRADATION AND GROWTH FACTOR RELEASE MODEL

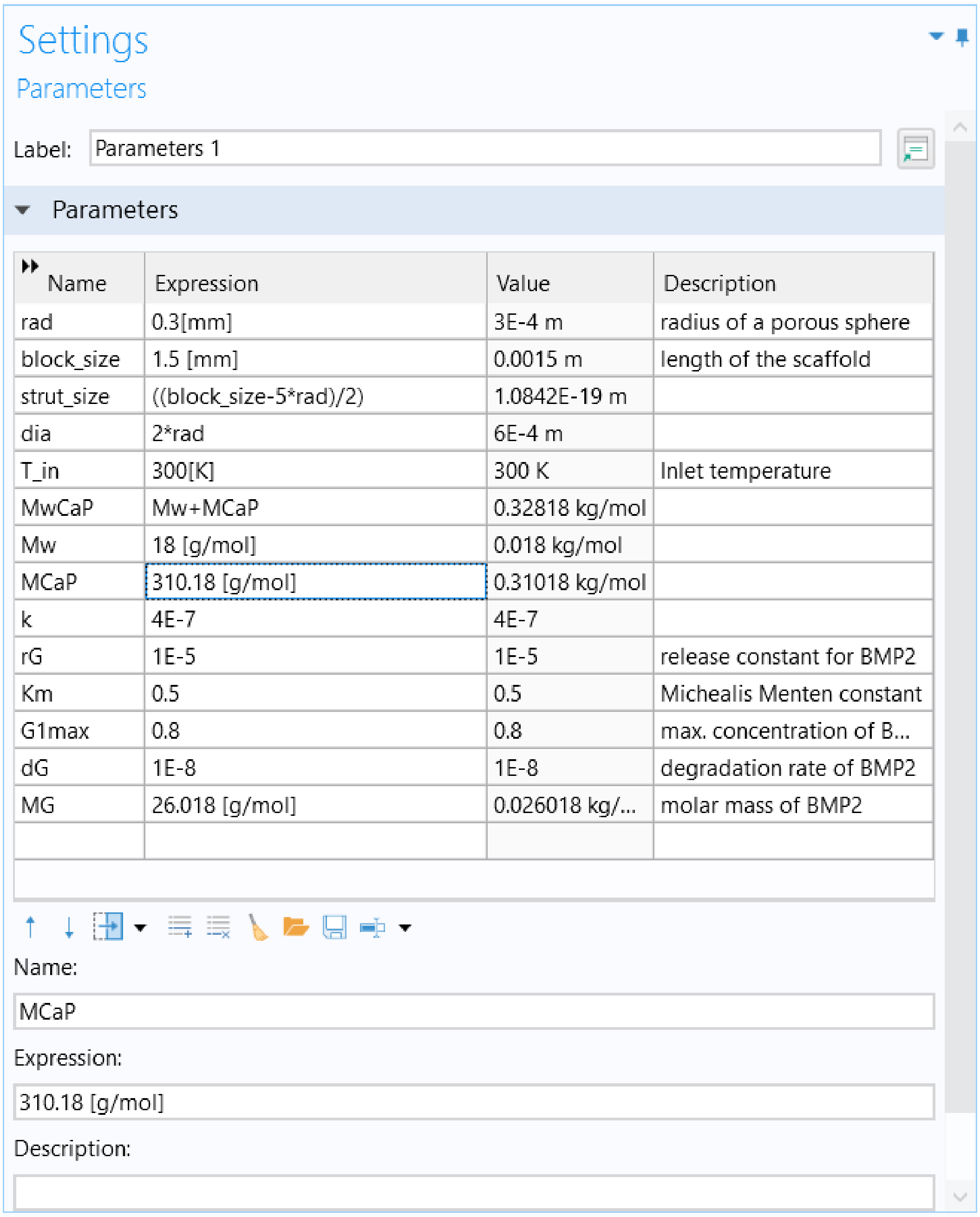

Settings

Parameters

Label: Parameters 1

Parameters

Name	Expression	Value	Description
rad	0.3[mm]	3E-4 m	radius of a porous sphere
block_size	1.5 [mm]	0.0015 m	length of the scaffold
strut_size	((block_size-5*rad)/2)	1.0842E-19 m	
dia	2*rad	6E-4 m	
T_in	300[K]	300 K	Inlet temperature
MwCaP	Mw+MCaP	0.32818 kg/mol	
Mw	18 [g/mol]	0.018 kg/mol	
MCaP	310.18 [g/mol]	0.31018 kg/mol	
k	4E-7	4E-7	
rG	1E-5	1E-5	release constant for BMP2
Km	0.5	0.5	Michealis Menten constant
G1max	0.8	0.8	max. concentration of B...
dG	1E-8	1E-8	degradation rate of BMP2
MG	26.018 [g/mol]	0.026018 kg/...	molar mass of BMP2

Name:

MCaP

Expression:

310.18 [g/mol]

Description:

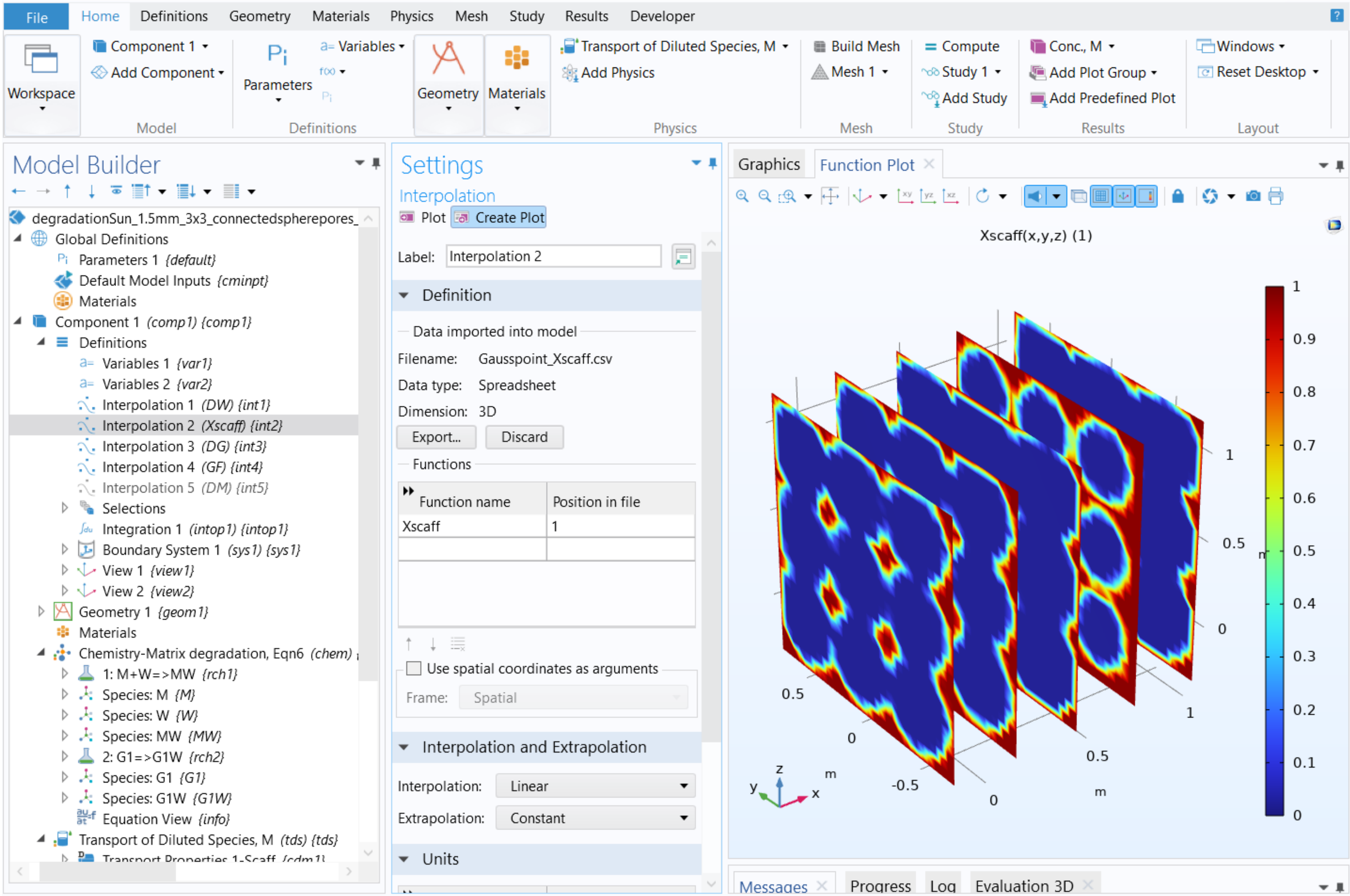

Label: Interpolation 2

Data imported into model

Filename: Gausspoint_Xscaff.csv

Data type: Spreadsheet

Dimension: 3D

Functions

Function name	Position in file
Xscaff	1

☐ Use spatial coordinates as arguments

Frame: Spatial

Interpolation: Linear

Extrapolation: Constant

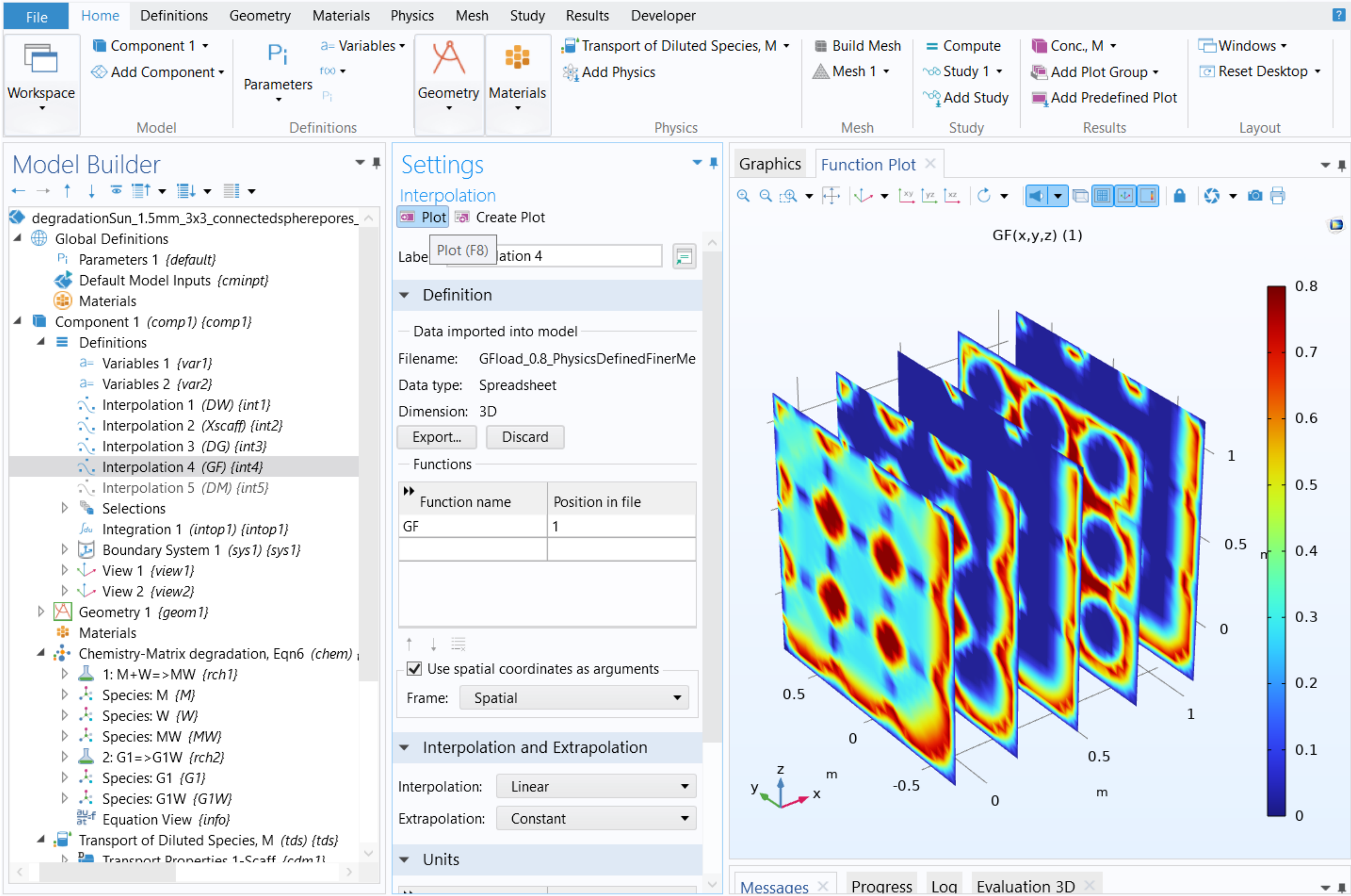

Label: Interpolation 4

Data imported into model

Filename: GFload_0.8_PhysicsDefinedFinerMe

Data type: Spreadsheet

Dimension: 3D

Functions

Function name	Position in file
GF	1

☑ Use spatial coordinates as arguments

Frame: Spatial

Interpolation: Linear

Extrapolation: Constant

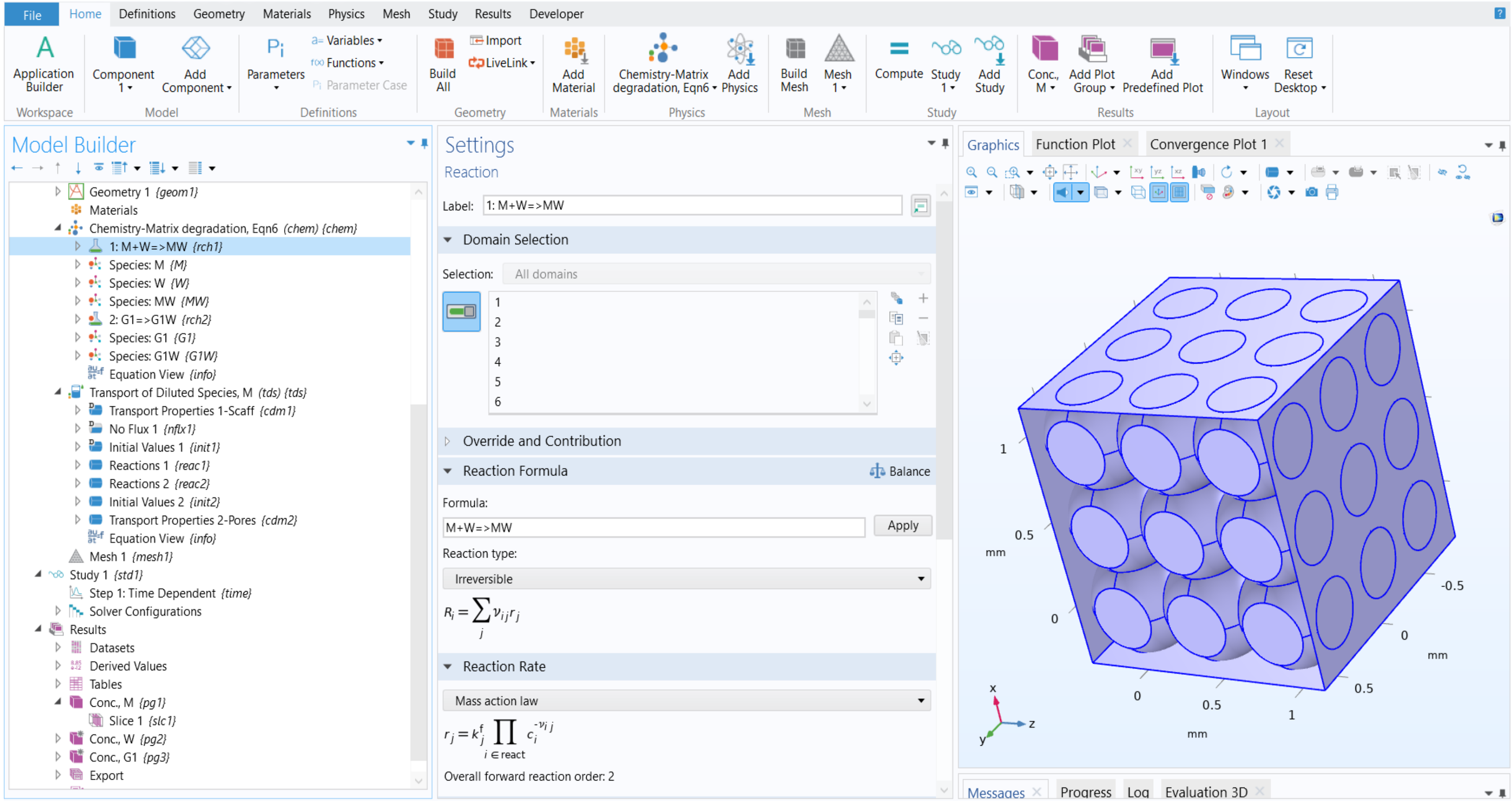

Label: 1: M+W=>MW

Selection: All domains

Formula: M+W=>MW

Reaction type: Irreversible

$$R_i = \sum_j \nu_{ij} r_j$$

Mass action law

$$r_j = k_j^f \prod_{i \in \text{react}} c_i^{-\nu_{ij}}$$

Overall forward reaction order: 2

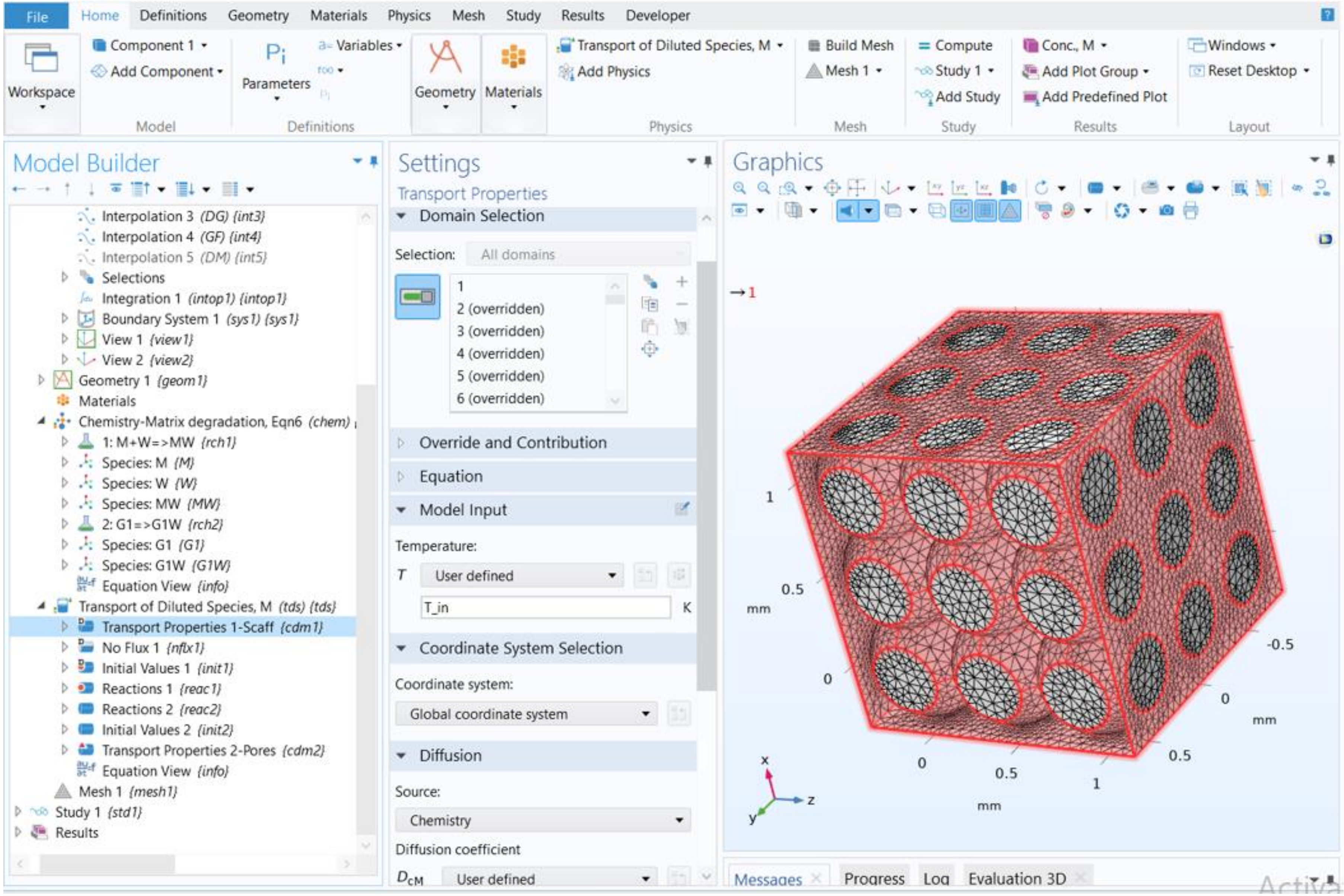

Interpolation 3 (DG) {int3}
Interpolation 4 (GF) {int4}
Interpolation 5 (DM) {int5}
Selections
Integration 1 (intop1) {intop1}
Boundary System 1 (sys1) {sys1}
View 1 {view1}
View 2 {view2}
Geometry 1 {geom1}
Materials
Chemistry-Matrix degradation, Eqn6 (chem)
1: M+W=>MW {rch1}
Species: M {M}
Species: W {W}
Species: MW {MW}
2: G1=>G1W {rch2}
Species: G1 {G1}
Species: G1W {G1W}
Equation View {info}
Transport of Diluted Species, M (tds) {tds}
Transport Properties 1-Scaff {cdm1}
No Flux 1 {nflx1}
Initial Values 1 {init1}
Reactions 1 {reac1}
Reactions 2 {reac2}
Initial Values 2 {init2}
Transport Properties 2-Pores {cdm2}
Equation View {info}
Mesh 1 {mesh1}
Study 1 {std1}
Results

Transport Properties

Domain Selection

Selection: All domains

1
2 (overridden)
3 (overridden)
4 (overridden)
5 (overridden)
6 (overridden)

Override and Contribution

Equation

Model Input

Temperature:

T User defined

T_in K

Coordinate System Selection

Coordinate system:

Global coordinate system

Diffusion

Source:

Chemistry

Diffusion coefficient

D_{cM} User defined

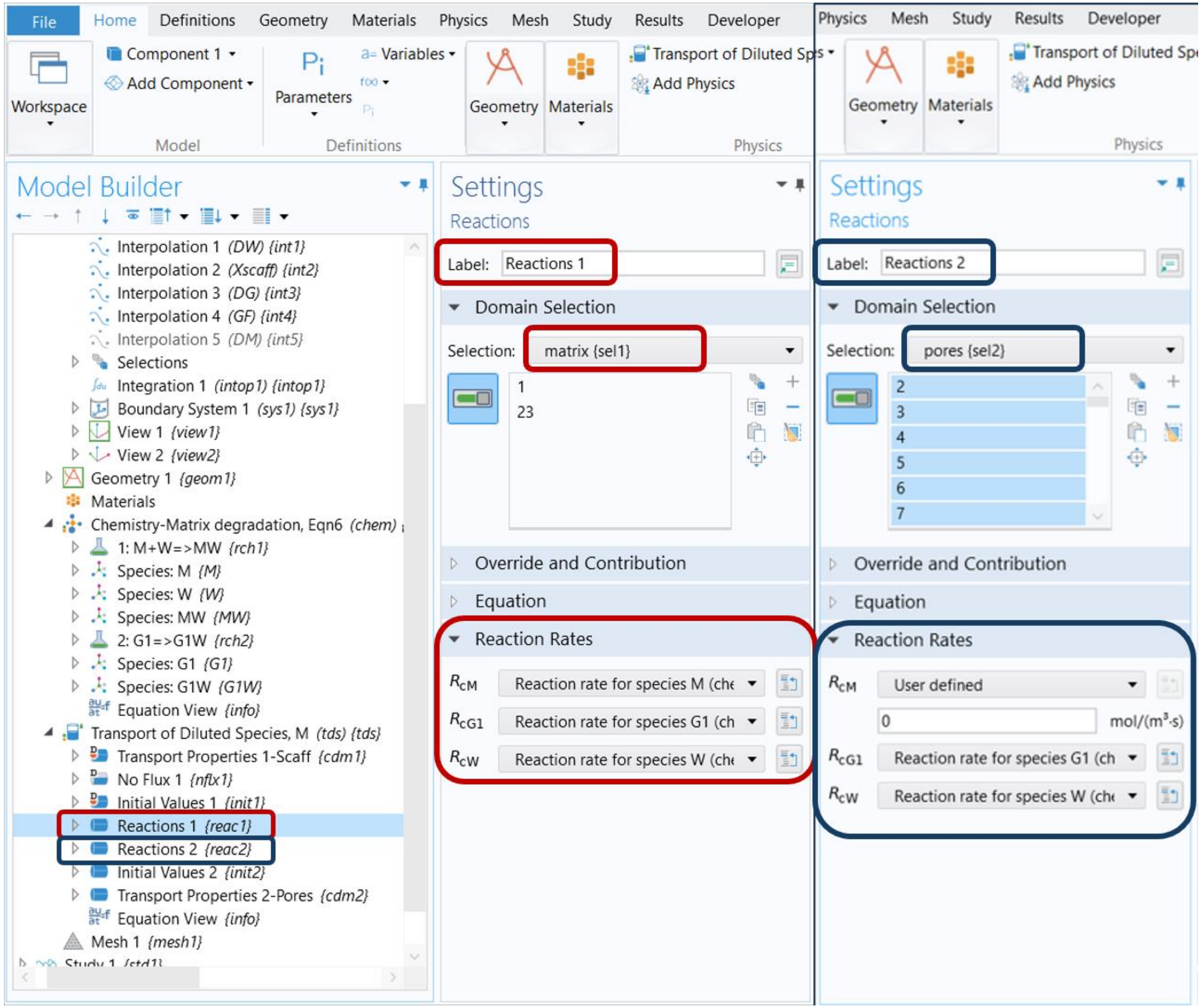

Settings

Reactions

Label: Reactions 1

Domain Selection

Selection: matrix {sel1}

1
23

Reaction Rates

R_{cM} Reaction rate for species M (che

R_{cG1} Reaction rate for species G1 (ch

R_{cW} Reaction rate for species W (che

Settings

Reactions

Label: Reactions 2

Domain Selection

Selection: pores {sel2}

2
3
4
5
6
7

Reaction Rates

R_{cM} User defined

0 mol/(m³·s)

R_{cG1} Reaction rate for species G1 (ch

R_{cW} Reaction rate for species W (che

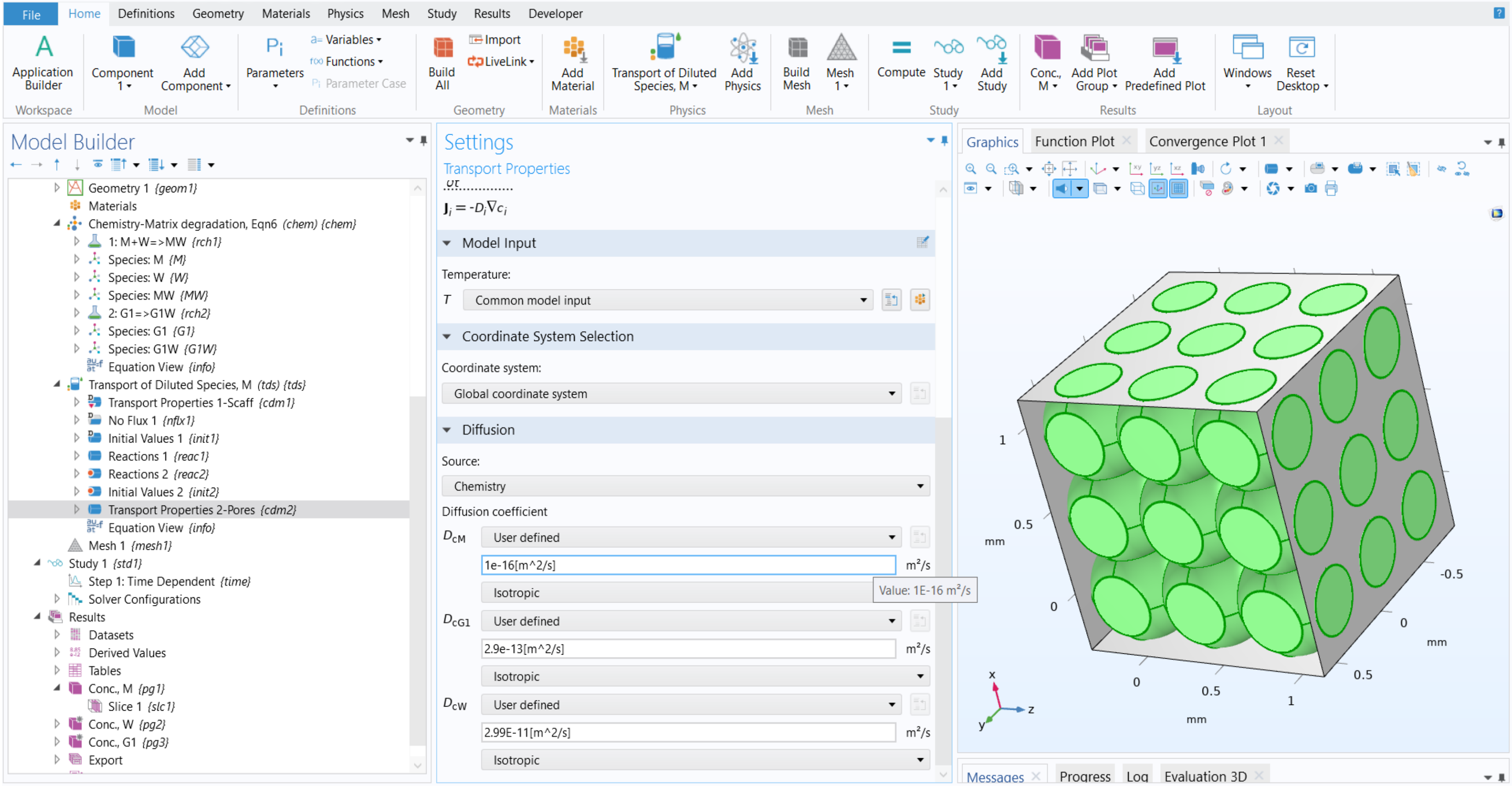

Model Builder

- Geometry 1 *{geom1}*
- Materials
- Chemistry-Matrix degradation, Eqn6 *(chem) {chem}*
  - 1: M+W=>MW *{rch1}*
  - Species: M *{M}*
  - Species: W *{W}*
  - Species: MW *{MW}*
  - 2: G1=>G1W *{rch2}*
  - Species: G1 *{G1}*
  - Species: G1W *{G1W}*
  - Equation View *{info}*
- Transport of Diluted Species, M *(tds) {tds}*
  - Transport Properties 1-Scaff *{cdm1}*
  - No Flux 1 *{nflx1}*
  - Initial Values 1 *{init1}*
  - Reactions 1 *{reac1}*
  - Reactions 2 *{reac2}*
  - Initial Values 2 *{init2}*
  - Transport Properties 2-Pores *{cdm2}*
  - Equation View *{info}*
- Mesh 1 *{mesh1}*
- Study 1 *{std1}*
  - Step 1: Time Dependent *{time}*
  - Solver Configurations
- Results
  - Datasets
  - Derived Values
  - Tables
  - Conc., M *{pg1}*
    - Slice 1 *{slc1}*
  - Conc., W *{pg2}*
  - Conc., G1 *{pg3}*
  - Export

Settings

Transport Properties

$\mathbf{J}_i = -D_i \nabla c_i$

Model Input

Temperature:

T: Common model input

Coordinate System Selection

Coordinate system:

Global coordinate system

Diffusion

Source:

Chemistry

Diffusion coefficient

D_{cM}: User defined

1e-16[m^2/s] m²/s

Isotropic

Value: 1E-16 m²/s

D_{cG1}: User defined

2.9e-13[m^2/s] m²/s

Isotropic

D_{cW}: User defined

2.99E-11[m^2/s] m²/s

Isotropic

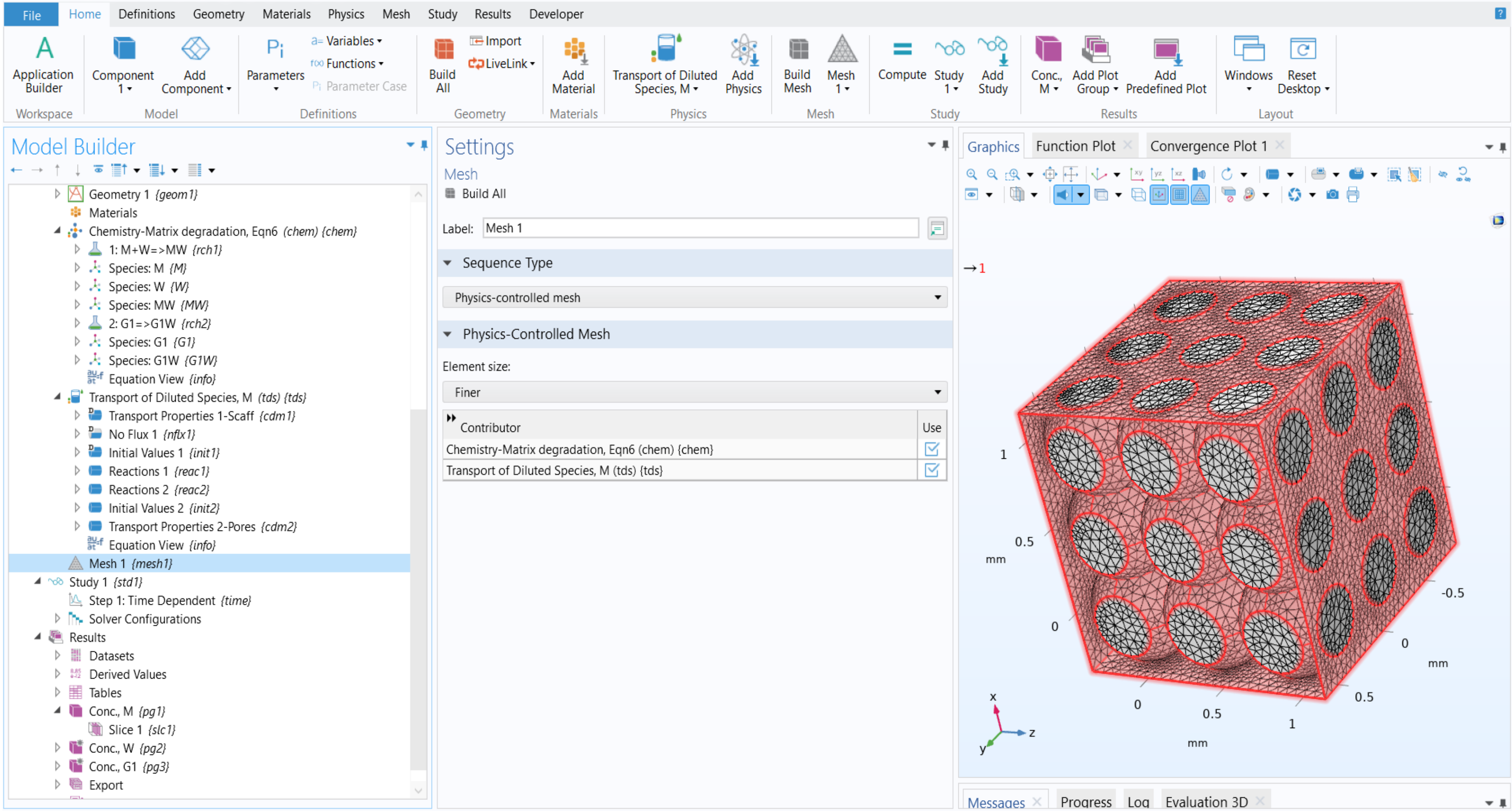

- Geometry 1 *{geom1}*
- Materials
- Chemistry-Matrix degradation, Eqn6 *(chem) {chem}*
  - 1: M+W=>MW *{rch1}*
  - Species: M *{M}*
  - Species: W *{W}*
  - Species: MW *{MW}*
  - 2: G1=>G1W *{rch2}*
  - Species: G1 *{G1}*
  - Species: G1W *{G1W}*
  - Equation View *{info}*
- Transport of Diluted Species, M *(tds) {tds}*
  - Transport Properties 1-Scaff *{cdm1}*
  - No Flux 1 *{nflx1}*
  - Initial Values 1 *{init1}*
  - Reactions 1 *{reac1}*
  - Reactions 2 *{reac2}*
  - Initial Values 2 *{init2}*
  - Transport Properties 2-Pores *{cdm2}*
  - Equation View *{info}*
- Mesh 1 *{mesh1}*

- Study 1 *{std1}*
  - Step 1: Time Dependent *{time}*
  - Solver Configurations
- Results
  - Datasets
  - Derived Values
  - Tables
  - Conc., M *{pg1}*
    - Slice 1 *{slc1}*
  - Conc., W *{pg2}*
  - Conc., G1 *{pg3}*
  - Export

Label: Mesh 1

Sequence Type

Physics-controlled mesh

Physics-Controlled Mesh

Element size:

Finer

Contributor	Use
Chemistry-Matrix degradation, Eqn6 (chem) {chem}	☑
Transport of Diluted Species, M (tds) {tds}	☑

C. OPTIMIZATION MODEL SCRIPTS

C1. Optimizer Module for Optimization Model 2

```
cd D:\
cd D:\sezen\Optimizasyon\dG&rG
clc
clear
%% The optimization code
%%
tic
format long
diary 'diary.txt' % Saves everything on the Command Window

x0 = [10, 5, 0.1];  % degradation rate and release rate of GF, respecitively
(1/s)
A = [];   %Linear and nonlinear inequaility constraints
B = [];
Aeq = [];
Beq = [];

lb  = [0.04, 0.1, 0.01]; % lower limit, multiply dG by 1E-7 and rG by 1E-5
before giving it to COMSOL.
ub = [50, 20, 20];  % upper limit

import com.comsol.model.*
import com.comsol.model.util.*
model = ModelUtil.create('Model'); % Load the model

history.x = [];
history.fval = [];
searchdir = [];

opts  =  optimoptions('fmincon','Display','iter-detailed',  'Algorithm','sqp',
...
    'PlotFcn',{@optimplotx,@optimplotfval,@optimplotfirstorderopt},
'ScaleProblem', true, ...
    'OptimalityTolerance',0.01, 'DiffMinChange', 0.05, 'DiffMaxChange', 5);
opts.Display = ' iter-detailed';
sprintf('ScaleProblem : true\n')
```

```
[xopt, fval,exitflag,output,lambda,grad,hessian]  = fmincon(@(x) Main_obj(x),
x0, A, B, Aeq, Beq, lb, ub, [], opts);


toc  % calculates how long the run took

function [f] = Main_obj(x)
    sprintf('\n - - - - OBJECTIVE FUNC - - -\n')
    format long

    [objective_value] = Main_obj_all_t_DG(x);
    sprintf('%f:');
    f = objective_value % GF conc.

end
```

C2. Main Module for Optimization Model 2

```
function [objective_value] = Main_obj_all_t_DG(x)
%global x_values

    sprintf('\n - - - - MAIN SCRIPT - - -\n')
    format long

    import com.comsol.model.*
    import com.comsol.model.util.*
    model = ModelUtil.create('Model'); % Load the model
    model.modelPath('D:\sezen\Optimizasyon\dG&rG');  % lokasyonu ekle
    model=mphload('Model_FinalResults_Case5h_ForOptof_dGand_rG.mph'); %% ekle

    model.param.set('dG1', [num2str(x(1)*1E-7,'%.9f')], 'degradation rate of
BMP2');

    model.param.set('rG1', [num2str(x(2)*1E-5,'%.7f')], 'release constant for
BMP2');

    model.param.set('Kc', [num2str(x(3),'%.4f')], 'Michealis Menten
constant');
```

```
   % Define the folder where you want to save Excel files
   folder1 = 'D:\sezen\Optimizasyon\dG&rG';

   folder_num=sprintf('dG&rG_%x',x);
   folder = fullfile(folder1,folder_num);
        if ~exist(folder, 'dir')
        mkdir(folder);
        end

   mphsave(model,'D:\sezen\Optimizasyon\dG&rG_%x\OptimizasyonModel_%x.mph')

    %To activate the progress bar
    ModelUtil.showProgress(true);

    model.study('std1').run;

    %Get model result by mphinterp in a node
    point_coord_scaffold = [1.2; -0.24; 0.72];  % coordinates of a scaffold point to evaluate, (transposition) --> coords. in column

    point_coord_pore = [0.45; -0.03; 0.45];     % coordinates of a pore point to evaluate, (transposition) --> coords. in column

    GF_matrix_scaffold = mphinterp(model,'cG1','coord',point_coord_scaffold); % evaluation of polymer concentration (PC) at selected scaffold node

    GF_matrix_pore  =  mphinterp(model,'cG1','coord',point_coord_pore);  % evaluation of polymer concentration (PC) at selected scaffold node

    GF7_scaff  =  GF_matrix_scaffold(2)  %GF  value  at  2nd  time  step,  to  be optimized
    GF14_scaff = GF_matrix_scaffold(3)
    GF21_scaff = GF_matrix_scaffold(4)
    GF28_scaff = GF_matrix_scaffold(5)

    GF7_pore = GF_matrix_pore(2) %GF value at 2nd time step, to be optimized
    GF14_pore = GF_matrix_pore(3)
    GF21_pore = GF_matrix_pore(4)
    GF28_pore = GF_matrix_pore(5)
```

```
    % Perform necessary computations on the data to calculate the objective
value(your computation code here)
    objective_value = sum((GF7_scaff - 0.9).^2 + (GF14_scaff - 0.9).^2 +
(GF21_scaff - 1).^2 + (GF28_scaff - 1).^2 + ...
        (GF7_pore - 0.5).^2 + (GF14_pore - 0.7).^2 + (GF21_pore - 0.8).^2 +
(G28_pore - 0.7).^2);

end
```

D. RESULTS OF PARAMETRIC STUDIES BASED ON 3D SIMULATION MODEL

(D_W: diffusivity of water, k: hydrolysis rate constant, D_G: diffusivity of BMP-2, r_G: release constant of BMP-2, d_G: degradation constant of BMP-2)

D1. Effect of k (and D_W)

D_W: 4.6x10^{-14} m^2/s, D_G: 2.9x10^{-15} m^2/s, d_G: 3.4x10^{-7} 1/s, r_G: 2x10^{-5} 1/s.

Changing parameter	**Pores**										**Scaffold**									
k [1/s]	**M0**	**G0**	**M7**	**G7**	**M14**	**G14**	**M21**	**G21**	**M28**	**G28**	**M0**	**G0**	**M7**	**G7**	**M14**	**G14**	**M21**	**G21**	**M28**	**G28**
8.30E-06	0.000	0.000	0.003	0.525	0.005	0.604	0.005	0.622	0.006	0.623	1.000	0.000	0.053	0.682	0.013	0.707	0.005	0.710	0.002	0.706
8.30E-07	0.000	0.000	0.000	0.541	0.001	0.634	0.002	0.658	0.002	0.662	1.000	0.000	0.667	0.698	0.466	0.729	0.343	0.736	0.235	0.737
6.00E-07	0.000	0.000	0.000	0.547	0.001	0.639	0.001	0.661	0.001	0.665	1.000	0.000	0.743	0.700	0.565	0.731	0.437	0.739	0.343	0.737
5.00E-07	0.000	0.000	0.000	0.550	0.001	0.640	0.001	0.661	0.001	0.666	1.000	0.000	0.780	0.701	0.615	0.732	0.493	0.740	0.398	0.740
4.00E-07	0.000	0.000	0.000	0.550	0.000	0.640	0.001	0.662	0.001	0.667	1.000	0.000	0.817	0.701	0.672	0.732	0.559	0.740	0.468	0.741
3.00E-07	0.000	0.000	0.000	0.550	0.000	0.641	0.001	0.663	0.001	0.668	1.000	0.000	0.857	0.702	0.736	0.733	0.637	0.741	0.555	0.742
8.30E-08	0.000	0.000	0.000	0.552	0.000	0.643	0.000	0.664	0.000	0.670	1.000	0.000	0.950	0.703	0.901	0.734	0.856	0.742	0.813	0.744

D_W: 4.6x10^{-12} m^2/s, D_G: 2.9x10^{-15} m^2/s, d_G: 3.4x10^{-7} 1/s, r_G: 2x10^{-5} 1/s.

Changing parameter	**Pores**										**Scaffold**									
k [1/s]	**M0**	**G0**	**M7**	**G7**	**M14**	**G14**	**M21**	**G21**	**M28**	**G28**	**M0**	**G0**	**M7**	**G7**	**M14**	**G14**	**M21**	**G21**	**M28**	**G28**
8.30E-06	0.000	0.000	0.003	0.524	0.005	0.604	0.006	0.623	0.006	0.624	1.000	0.000	0.056	0.679	0.016	0.705	0.006	0.710	0.003	0.707
1.00E-06	0.000	0.000	0.000	0.543	0.001	0.634	0.001	0.657	0.001	0.661	1.000	0.000	0.611	0.696	0.405	0.728	0.274	0.735	0.179	0.736
8.30E-07	0.000	0.000	0.000	0.541	0.001	0.634	0.002	0.658	0.002	0.662	1.000	0.000	0.667	0.698	0.466	0.729	0.343	0.736	0.235	0.737
6.00E-07	0.000	0.000	0.000	0.545	0.001	0.638	0.001	0.660	0.001	0.664	1.000	0.000	0.738	0.699	0.563	0.731	0.438	0.739	0.345	0.739
5.00E-07	0.000	0.000	0.000	0.544	0.000	0.634	0.001	0.660	0.001	0.665	1.000	0.000	0.774	0.700	0.611	0.731	0.491	0.738	0.400	0.740
4.00E-07	0.000	0.000	0.000	0.550	0.000	0.640	0.001	0.661	0.001	0.666	1.000	0.000	0.814	0.700	0.672	0.732	0.559	0.740	0.466	0.741
3.00E-07	0.000	0.000	0.000	0.551	0.000	0.641	0.001	0.663	0.001	0.668	1.000	0.000	0.854	0.702	0.737	0.733	0.638	0.741	0.557	0.742

D2. Effect of D_W (and d_G)

k: 8.3x10^{-7} 1/s, D_G: 2.9x10^{-15} m^2/s, d_G: 3.4x10^{-7} 1/s, r_G: 2x10^{-5} 1/s.

Changing parameter	**Pores**										**Scaffold**									
D_W in polymer [m^2/s]	**M0**	**G0**	**M7**	**G7**	**M14**	**G14**	**M21**	**G21**	**M28**	**G28**	**M0**	**G0**	**M7**	**G7**	**M14**	**G14**	**M21**	**G21**	**M28**	**G28**
4.60E-16	0.000	0.000	0.000	0.508	0.001	0.614	0.001	0.647	0.001	0.656	1.000	0.000	0.904	0.606	0.781	0.686	0.662	0.707	0.555	0.714

4.60E-15	0.000	0.000	0.000	0.541	0.001	0.635	0.002	0.657	0.002	0.662	1.000	0.000	0.778	0.686	0.554	0.728	0.394	0.737	0.278	0.738
4.60E-14	0.000	0.000	0.000	0.541	0.001	0.634	0.002	0.658	0.002	0.662	1.000	0.000	0.667	0.698	0.466	0.729	0.343	0.736	0.235	0.737
4.60E-13	0.000	0.000	0.000	0.543	0.001	0.634	0.002	0.658	0.002	0.662	1.000	0.000	0.662	0.698	0.462	0.727	0.334	0.737	0.240	0.739
4.60E-12	0.000	0.000	0.000	0.548	0.001	0.637	0.001	0.658	0.002	0.662	1.000	0.000	0.667	0.698	0.467	0.729	0.336	0.737	0.243	0.737

k: $8.3x10^{-7}$ 1/s, D_G: $2.9x10^{-15}$ m^2/s, **d_G: $2.4x10^{-7}$ 1/s**, r_G: $2x10^{-5}$ 1/s.

Changing parameter	**Pores**										**Scaffold**									
D_W in polymer [m^2/s]	**M0**	**G0**	**M7**	**G7**	**M14**	**G14**	**M21**	**G21**	**M28**	**G28**	**M0**	**G0**	**M7**	**G7**	**M14**	**G14**	**M21**	**G21**	**M28**	**G28**
4.60E-12	0.000	0.000	0.000	0.548	0.001	0.637	0.001	0.658	0.002	0.662	1.000	0.000	0.667	0.698	0.467	0.729	0.336	0.737	0.243	0.737
4.60E-14	0.000	0.000	0.000	0.557	0.001	0.660	0.002	0.689	0.002	0.696	1.000	0.000	0.667	0.707	0.466	0.741	0.343	0.750	0.235	0.753
4.60E-15	0.000	0.000	0.000	0.557	0.001	0.662	0.001	0.690	0.002	0.697	1.000	0.000	0.780	0.696	0.556	0.740	0.395	0.752	0.277	0.754
4.60E-16	0.000	0.000	0.000	0.523	0.001	0.641	0.001	0.679	0.001	0.690	1.000	0.000	0.903	0.619	0.778	0.704	0.657	0.745	0.550	0.736

k: 3x10^{-7} 1/s, D_G: 2.9x10^{-15} m^2/s, **d$_G$: 1x10^{-8} 1/s**, r_G: 2x10^{-5} 1/s.

Changing parameter	**Pores**										**Scaffold**									
D_W in polymer [m^2/s]	**M0**	**G0**	**M7**	**G7**	**M14**	**G14**	**M21**	**G21**	**M28**	**G28**	**M0**	**G0**	**M7**	**G7**	**M14**	**G14**	**M21**	**G21**	**M28**	**G28**
4.60E-15	0.000	0.000	0.000	0.598	0.000	0.733	0.000	0.775	0.001	0.789	1.000	0.000	0.901	0.722	0.777	0.775	0.670	0.791	0.580	0.796
4.60E-14	0.000	0.000	0.000	0.605	0.000	0.729	0.001	0.774	0.001	0.788	1.000	0.000	0.857	0.731	0.735	0.776	0.636	0.789	0.557	0.799
4.60E-13	0.000	0.000	0.000	0.600	0.000	0.731	0.000	0.776	0.001	0.789	1.000	0.000	0.852	0.729	0.734	0.773	0.637	0.793	0.556	0.798
4.60E-12	0.000	0.000	0.000	0.603	0.000	0.734	0.001	0.776	0.001	0.788	1.000	0.000	0.853	0.728	0.735	0.775	0.638	0.791	0.555	0.796

k: 1x10^{-6} 1/s, D_G: 2.9x10^{-15} m^2/s, **d$_G$: 1x10^{-8} 1/s**, r_G: 2x10^{-5} 1/s.

Changing parameter	**Pores**										**Scaffold**									
D_W in polymer [m^2/s]	**M0**	**G0**	**M7**	**G7**	**M14**	**G14**	**M21**	**G21**	**M28**	**G28**	**M0**	**G0**	**M7**	**G7**	**M14**	**G14**	**M21**	**G21**	**M28**	**G28**
4.60E-15	0.000	0.000	0.000	0.595	0.001	0.728	0.001	0.772	0.002	0.787	1.000	0.000	0.754	0.714	0.504	0.772	0.336	0.789	0.214	0.795
4.60E-14	0.000	0.000	0.001	0.602	0.001	0.728	0.002	0.770	0.002	0.786	1.000	0.000	0.624	0.728	0.401	0.774	0.264	0.789	0.175	0.794
4.60E-12	0.000	0.000	0.000	0.599	0.001	0.730	0.002	0.773	0.002	0.788	1.000	0.000	0.612	0.725	0.405	0.773	0.275	0.789	0.180	0.795
4.60E-11	0.000	0.000	0.000	0.602	0.001	0.727	0.002	0.772	0.002	0.787	1.000	0.000	0.617	0.728	0.402	0.772	0.275	0.790	0.179	0.794

4.60E-06	0.000	0.000	0.000	0.603	0.001	0.730	0.002	0.770	0.002	0.785	1.000	0.000	0.619	0.728	0.407	0.774	0.273	0.789	0.184	0.794

D3. Effect of D_G (and D_W, k and d_G)

D_W: 4.6x10^{-14} m^2/s, k: 8.3x10^{-7} 1/s, d_G: 3.4x10^{-7} 1/s, r_G: 2x10^{-5} 1/s.

Changing parameter	**Pores**										**Scaffold**									
D_G in polymer [m^2/s]	**M0**	**G0**	**M7**	**G7**	**M14**	**G14**	**M21**	**G21**	**M28**	**G28**	**M0**	**G0**	**M7**	**G7**	**M14**	**G14**	**M21**	**G21**	**M28**	**G28**
2.90E-16	0.000	0.000	0.000	0.502	0.001	0.603	0.002	0.631	0.002	0.638	1.000	0.000	0.669	0.720	0.463	0.741	0.330	0.747	0.236	0.747
2.90E-15	0.000	0.000	0.000	0.541	0.001	0.634	0.002	0.658	0.002	0.662	1.000	0.000	0.667	0.698	0.466	0.729	0.343	0.736	0.235	0.737
2.90E-14	0.000	0.000	0.000	0.589	0.001	0.669	0.002	0.683	0.002	0.685	1.000	-0.002	0.667	0.698	0.460	0.720	0.329	0.732	0.235	0.722
2.90E-13	0.000	0.004	0.000	0.624	0.001	0.694	0.002	0.703	0.002	0.702	1.000	-0.021	0.668	0.638	0.467	0.701	0.331	0.710	0.237	0.708

D_W: $4.6x10^{-12}$ m^2/s, k: $8.3x10^{-7}$ 1/s, d_G: $3.4x10^{-7}$ 1/s, r_G: $2x10^{-5}$ 1/s.

Changing parameter	**Pores**										**Scaffold**									
D_G in polymer [m^2/s]	**M0**	**G0**	**M7**	**G7**	**M14**	**G14**	**M21**	**G21**	**M28**	**G28**	**M0**	**G0**	**M7**	**G7**	**M14**	**G14**	**M21**	**G21**	**M28**	**G28**
2.90E-16	0.000	0.000	0.000	0.497	0.001	0.602	0.002	0.631	0.002	0.638	1.000	0.000	0.660	0.719	0.470	0.742	0.335	0.748	0.237	0.747
2.90E-15	0.000	0.000	0.000	0.548	0.001	0.637	0.001	0.658	0.002	0.662	1.000	0.000	0.667	0.698	0.467	0.729	0.336	0.737	0.243	0.737
2.90E-14	0.000	0.000	0.000	0.589	0.001	0.669	0.002	0.684	0.002	0.685	1.000	-0.002	0.665	0.675	0.472	0.716	0.338	0.731	0.241	0.721
2.90E-13	0.000	0.004	0.000	0.630	0.001	0.695	0.002	0.703	0.002	0.702	1.000	-0.021	0.668	0.643	0.467	0.703	0.333	0.710	0.239	0.709

D_W: $4.6x10^{-12}$ m^2/s, **k: $4x10^{-7}$ 1/s**, **d_G: $1x10^{-8}$ 1/s**, r_G: $2x10^{-5}$ 1/s.

Changing parameter	**Pores**										**Scaffold**									
D_G in polymer [m^2/s]	**M0**	**G0**	**M7**	**G7**	**M14**	**G14**	**M21**	**G21**	**M28**	**G28**	**M0**	**G0**	**M7**	**G7**	**M14**	**G14**	**M21**	**G21**	**M28**	**G28**
2.90E-16	0.000	0.000	0.000	0.556	0.000	0.708	0.001	0.763	0.001	0.782	1.000	0.000	0.813	0.745	0.672	0.780	0.560	0.791	0.467	0.796

2.90E-15	0.000	0.000	0.000	0.605	0.000	0.734	0.001	0.774	0.001	0.787	1.000	0.000	0.814	0.729	0.672	0.775	0.560	0.791	0.468	0.795
2.90E-14	0.000	0.000	0.000	0.642	0.000	0.756	0.001	0.786	0.001	0.794	1.000	-0.002	0.811	0.710	0.669	0.774	0.562	0.792	0.474	0.798
2.90E-13	0.000	0.004	0.000	0.685	0.000	0.772	0.001	0.792	0.001	0.796	1.000	-0.021	0.814	0.694	0.670	0.774	0.560	0.793	0.476	0.796

D4. Effect of r_G (and D_W, k and d_G)

D_W: $4.6\text{x}10^{-14}$ m^2/s, k: $8.3\text{x}10^{-7}$ 1/s, D_G: $2.9\text{x}10^{-15}$ m^2/s, d_G: $3.4\text{x}10^{-7}$ 1/s.

Changing parameter	**Pores**										**Scaffold**									
r_G [1/s]	**M0**	**G0**	**M7**	**G7**	**M14**	**G14**	**M21**	**G21**	**M28**	**G28**	**M0**	**G0**	**M7**	**G7**	**M14**	**G14**	**M21**	**G21**	**M28**	**G28**
2.00E-04	0.000	0.000	0.000	0.778	0.001	0.778	0.001	0.777	0.001	0.777	1.000	0.000	0.670	0.798	0.468	0.798	0.332	0.798	0.232	0.798
7.00E-05	0.000	0.000	0.000	0.735	0.001	0.750	0.001	0.750	0.002	0.749	1.000	0.000	0.669	0.789	0.466	0.790	0.319	0.789	0.228	0.789
2.00E-05	0.000	0.000	0.000	0.541	0.001	0.634	0.002	0.658	0.002	0.662	1.000	0.000	0.667	0.698	0.466	0.729	0.343	0.736	0.235	0.737
1.00E-05	0.000	0.000	0.000	0.415	0.001	0.508	0.001	0.547	0.001	0.562	1.000	0.000	0.670	0.588	0.464	0.635	0.330	0.655	0.237	0.661
7.00E-06	0.000	0.000	0.000	0.360	0.001	0.439	0.001	0.479	0.002	0.497	1.000	0.000	0.671	0.527	0.465	0.574	0.331	0.596	0.233	0.607
2.00E-06	0.000	0.000	0.000	0.242	0.001	0.260	0.001	0.272	0.002	0.280	1.000	0.000	0.668	0.353	0.456	0.368	0.326	0.374	0.235	0.379

D_W: 4.6x10^{-14} m^2/s, k: 8.3x10^{-7} 1/s, D_G: 2.9x10^{-15} m^2/s, **d_G: 2.4x10^{-7} 1/s**.

Changing parameter	**Pores**										**Scaffold**									
r_G [1/s]	**M0**	**G0**	**M7**	**G7**	**M14**	**G14**	**M21**	**G21**	**M28**	**G28**	**M0**	**G0**	**M7**	**G7**	**M14**	**G14**	**M21**	**G21**	**M28**	**G28**
7.00E-05	0.000	0.000	0.000	0.747	0.001	0.764	0.001	0.764	0.002	0.763	1.000	0.000	0.669	0.791	0.460	0.793	0.331	0.792	0.236	0.792
2.00E-05	0.000	0.000	0.000	0.557	0.001	0.660	0.002	0.689	0.002	0.696	1.000	0.000	0.667	0.707	0.466	0.741	0.343	0.750	0.235	0.753
1.00E-05	0.000	0.000	0.000	0.430	0.001	0.536	0.001	0.585	0.002	0.607	1.000	0.000	0.670	0.600	0.464	0.653	0.332	0.678	0.235	0.689
9.00E-06	0.000	0.000	0.000	0.413	0.001	0.516	0.001	0.565	0.002	0.589	1.000	0.000	0.670	0.582	0.464	0.637	0.331	0.663	0.235	0.675
7.00E-06	0.000	0.000	0.000	0.373	0.001	0.465	0.001	0.516	0.001	0.543	1.000	0.000	0.669	0.546	0.471	0.594	0.326	0.623	0.233	0.637
2.00E-06	0.000	0.000	0.000	0.254	0.001	0.283	0.001	0.304	0.001	0.319	1.000	0.000	0.668	0.367	0.457	0.392	0.323	0.407	0.230	0.417
1.00E-08	0.000	0.000	0.001	0.193	0.001	0.168	0.001	0.145	0.002	0.126	1.000	0.000	0.668	0.201	0.469	0.170	0.336	0.147	0.239	0.127

D_W: 4.6x10^{-12} m^2/s, k: 4x10^{-7} 1/s, D_G: 2.9x10^{-15} m^2/s, **d_G: 1x10^{-8} 1/s**.

Changing parameter	Pores										Scaffold									
r_G [1/s]	**M0**	**G0**	**M7**	**G7**	**M14**	**G14**	**M21**	**G21**	**M28**	**G28**	**M0**	**G0**	**M7**	**G7**	**M14**	**G14**	**M21**	**G21**	**M28**	**G28**
2.00E-05	0.000	0.000	0.000	0.605	0.000	0.734	0.001	0.774	0.001	0.787	1.000	0.000	0.814	0.729	0.672	0.775	0.560	0.791	0.468	0.795
1.50E-05	0.000	0.000	0.000	0.546	0.000	0.690	0.001	0.749	0.001	0.773	1.000	0.000	0.813	0.691	0.671	0.752	0.559	0.778	0.466	0.790
1.00E-05	0.000	0.000	0.000	0.468	0.000	0.611	0.001	0.692	0.001	0.736	1.000	0.000	0.812	0.633	0.668	0.704	0.561	0.740	0.478	0.771

D5. Effect of dG and rG

D_W: 4.6x10^{-14} m^2/s, k: 8.3x10^{-7} 1/s, D_G: 2.9x10^{-15} m^2/s, r_G: 2x10^{-5} 1/s.

Changing parameter	Pores										Scaffold									
d_G [1/s]	**M0**	**G0**	**M7**	**G7**	**M14**	**G14**	**M21**	**G21**	**M28**	**G28**	**M0**	**G0**	**M7**	**G7**	**M14**	**G14**	**M21**	**G21**	**M28**	**G28**
5.00E-09	0.000	0.000	0.000	0.596	0.001	0.730	0.002	0.775	0.002	0.790	1.000	0.000	0.667	0.728	0.466	0.773	0.338	0.790	0.233	0.796
1.00E-08	0.000	0.000	0.000	0.595	0.001	0.728	0.002	0.773	0.002	0.787	1.000	0.000	0.667	0.727	0.466	0.773	0.338	0.790	0.237	0.800
5.00E-08	0.000	0.000	0.000	0.588	0.001	0.716	0.002	0.757	0.002	0.770	1.000	0.000	0.667	0.724	0.466	0.767	0.342	0.782	0.235	0.787

8.00E-08	0.000	0.000	0.000	0.583	0.001	0.707	0.002	0.746	0.002	0.758	1.000	0.000	0.667	0.721	0.466	0.763	0.338	0.777	0.235	0.781
1.00E-07	0.000	0.000	0.000	0.580	0.001	0.701	0.002	0.738	0.002	0.749	1.000	0.000	0.667	0.719	0.466	0.760	0.338	0.773	0.236	0.778
2.40E-07	0.000	0.000	0.000	0.557	0.001	0.660	0.002	0.689	0.002	0.696	1.000	0.000	0.667	0.707	0.466	0.741	0.343	0.750	0.235	0.753
3.40E-07	0.000	0.000	0.000	0.541	0.001	0.634	0.002	0.658	0.002	0.662	1.000	0.000	0.667	0.698	0.466	0.729	0.343	0.736	0.235	0.737

D_W: 4.6x10^{-14} m^2/s, k: 8.3x10^{-7} 1/s, D_G: 2.9x10^{-15} m^2/s, **r_G: 2x10^{-4} 1/s.**

Changing parameter	**Pores**										**Scaffold**									
d_G [1/s]	**M0**	**G0**	**M7**	**G7**	**M14**	**G14**	**M21**	**G21**	**M28**	**G28**	**M0**	**G0**	**M7**	**G7**	**M14**	**G14**	**M21**	**G21**	**M28**	**G28**
5.00E-09	0.000	0.000	0.000	0.800	0.001	0.800	0.002	0.800	0.002	0.800	1.000	0.000	0.671	0.800	0.470	0.800	0.330	0.800	0.237	0.800
1.00E-07	0.000	0.000	0.000	0.793	0.001	0.793	0.001	0.793	0.001	0.793	1.000	0.000	0.672	0.799	0.461	0.799	0.328	0.799	0.236	0.799
2.40E-07	0.000	0.000	0.000	0.784	0.001	0.784	0.001	0.784	0.002	0.784	1.000	0.000	0.670	0.798	0.471	0.798	0.332	0.798	0.231	0.798
3.40E-07	0.000	0.000	0.000	0.778	0.001	0.778	0.001	0.777	0.001	0.777	1.000	0.000	0.670	0.798	0.468	0.798	0.332	0.798	0.232	0.798
1.00E-06	0.000	0.000	0.000	0.739	0.001	0.737	0.001	0.735	0.001	0.735	1.000	0.000	0.674	0.793	0.455	0.793	0.320	0.793	0.230	0.793
1.00E-05	0.000	0.000	0.000	0.426	0.001	0.421	0.001	0.417	0.002	0.413	1.000	0.000	0.669	0.737	0.464	0.735	0.329	0.733	0.235	0.732